Exploring Interactions between Agriculture and Air Quality on Regional to Global Scales

by

Luke D. Schiferl

B.S., University of Wisconsin–Madison, 2010
M.S. in Atmospheric Science, Colorado State University, 2012

Submitted to the Department of Civil and Environmental Engineering
in partial fulfillment of the requirements for the degree of

Doctor of Philosophy in Environmental Chemistry

at the

MASSACHUSETTS INSTITUTE OF TECHNOLOGY

February 2018

Signature of Author ..... Signature redacted
Department of Civil and Environmental Engineering
September 26, 2017

Certified by ..... Signature redacted
Colette L. Heald
Associate Professor of Civil and Environmental Engineering,
and Earth, Atmospheric and Planetary Sciences
Thesis Supervisor

Accepted by ..... Signature redacted
Jesse H. Kroll
Associate Professor of Civil and Environmental Engineering,
and Chemical Engineering
Chair, Graduate Program Committee

Exploring Interactions between Agriculture and Air Quality on Regional to Global Scales

by

Luke D. Schiferl

Submitted to the Department of Civil and Environmental Engineering
on September 26, 2017, in partial fulfillment of the
requirements for the degree of
Doctor of Philosophy in Environmental Chemistry

Abstract

As concern grows over increasing human population and the effects of industrialization on the environment, agriculture and air quality have become important areas of research. Both are vital to human prosperity, determining what we eat and what we breathe. The interactions between agriculture and air quality (defined by ozone and particulate matter (PM) concentrations) are many and often poorly understood. This thesis examines their interactions in two parts. First, we investigate the influence and characterize the importance of the variability in agricultural ammonia emissions on surface inorganic fine PM ($PM_{2.5}$). In a case study, airborne observations indicate that summertime concentrations of ammonia throughout California and $PM_{2.5}$ in Los Angeles are underestimated in a global chemistry model (GEOS-Chem) used to understand air quality issues. We find that increasing ammonia emissions from livestock and fertilizer allows the model to better represent the observations, thereby improving the model's prediction of $PM_{2.5}$ conditions in wintertime, when concentrations and impacts on human health are greater. We also use new observations (surface, aircraft, and satellite) to find that the model underrepresents the summertime ammonia concentration near large source regions throughout the United States. Meteorology dominates the underestimated year-to-year variability in the model over reductions in acid-precursors. Introduction of varying ammonia emissions does not improve the model comparison and has little impact on $PM_{2.5}$. Second, we quantify the impact of air quality on global crop production under current and future emissions scenarios. Using a relativistic approach, we find that the maximum positive impact (highly uncertain) from total PM light scattering can outweigh the negative impact from ozone damage in certain crops and regions. Future scenarios indicate that reductions in air pollution may have a net negative effect on crop production in areas dominated by the PM effect. We then employ a crop model (pDSSAT) to more realistically predict the lessened impact of PM under stress from resource restrictions. We also assess the effect of nitrogen deposition on crops compared to PM. Overall, we highlight the need for better observations of both ammonia concentrations and the impacts of PM on crop growth to reduce uncertainty in these interactions.

Thesis Supervisor: Colette L. Heald
Title: Associate Professor of Civil and Environmental Engineering,
and Earth, Atmospheric and Planetary Sciences

Acknowledgements

Thank you to Prof. Colette Heald, my advisor, for her guidance, support, understanding, knowledge, and wisdom. She has been a top role model for my development as a scientist, and I am proud to have been her student for the past seven years.

Thank you to Profs. Jesse Kroll, Dan Cziczo and Dennis McLaughlin for serving on my thesis committee. They were inspiring teachers in the classroom, and their challenging questions and insightful advice truly improved my research.

Thank you to Bonne, Dave, Maria, Qi, Xuan, Amos, Will, Sam, Jeff, Sarah, Emily, Flora, Ruud, Sid, Katie, and Tess for analysis advice and feedback, allowing me to use all of the disk space, and a continuous supply of coffee and breakfast pastries.

Thank you to the GEOS-Chem support team for model documentation and community infrastructure.

Thank you to the many collaborators who provided data and support:

- Aircraft measurements: John Nowak, John Holloway, Andrew Neuman, Roya Bahreini, Ilana Pollack, Thomas Ryerson, Ann Middlebrook, Scott Herndon, Rob Roscioli, and Scott Eilerman
- Ammonia satellite measurements: Martin Van Damme, Lieven Clarisse, Cathy Clerbaux, and Pierre-François Coheur
- Emissions inventories and implementation: Christine Wiedinmyer, Stu McKeen, Aaron van Donkelaar, Jingqui Mao, and Fabien Paulot
- Gridded crop model: David Kelly
- Valuable discussions: Jennifer Murphy, Jeff Collett, Jay Ham, and Lynn Russell

Thank you to the following funding agencies and sources: NOAA (grant NA12OAR4310064) (Chapters 2 and 3), the EPA-STAR program (GAD R83374) (Chapter 2), the Martin Family Fellowship for Sustainability at MIT (Chapters 4 and 5), and the Abdul Latif Jameel World Water and Food Security Lab (J-WAFS) at MIT (Chapters 4 and 5).

Thank you to my family and friends for their love, their encouragement, and providing distraction to dispel the intensity and stress inherent when working toward a PhD at MIT.

Contents

Chapter 1. Introduction

The need to produce food for a growing human population has increased the intensity of industrial agriculture in the past century. This agricultural system relies heavily on reactive nitrogen as an input for enhanced plant growth, which was historically a limiting nutrient, but is now produced from inert atmospheric nitrogen in the form of ammonia (NH_3) fertilizers [*Erisman et al.*, 2008; *Sutton et al.*, 2008]. Excess fertilizer not used by the intended agricultural crops is volatilized and released to the atmosphere or transported downstream to rivers and lakes. Plants used for the production of livestock pass nitrogen through to waste products, which can also release ammonia to the atmosphere when volatilized. This livestock waste has become the largest source of atmospheric ammonia globally [*Dentener and Crutzen*, 1994], overtaking sources such as natural ecosystems and wildfires. The future of agriculture is of concern globally as changes in air quality (described below), nutrient transport and water balance come to light. Agricultural nutrients transported away from source regions alter delicate balances and can cause acidification and eutrophication [*Erisman et al.*, 2007]. This is of particular concern in sensitive ecosystems such as alpine terrain and wetlands [*Beem et al.*, 2010; *Ellis et al.*, 2013].

Industrialization has had large effects on the air quality of human-settled areas through the modulation of pollutant concentrations. Two significant pollutants which affect air quality are particulate matter (PM) and ground-level ozone (O_3). PM refers to particles suspended in air and can be categorized based on size as either coarse PM (diameter less than 10 μm, PM_{10}) or fine PM (diameter less than 2.5 μm, $PM_{2.5}$). PM_{10} mass is dominated by natural sources, including dust and sea-salt, although their emission can be modified by human activities. $PM_{2.5}$ can be either emitted directly through combustion processes or formed through chemical reactions in the atmosphere. Increases in $PM_{2.5}$ concentration have negative effects on human health, as the small particles can more-readily enter the body, causing respiratory and cardiovascular distress and an overall decrease in life expectancy [*Pope et al.*, 2009]. PM is projected to be the largest environmental cause of death worldwide by 2030 [*OECD*, 2012]. Additionally, PM contributes to reduced visibility and affects the radiation balance of the planet [*IPCC*, 2013]. Ground-level ozone is formed through the reaction between NO_x ($NO + NO_2$) and volatile organic compounds (VOCs) in the presence of sunlight. Sources of NO_x and VOCs are both anthropogenic, such as motor vehicles and industrial processes, and natural. Ozone near the

surface is an oxidant and harmful to biological processes. In humans, ozone increases acute cases of respiratory illness [*Burnett et al.*, 2001]. Background ozone concentrations, meaning ozone present at a location which is not attributable to local anthropogenic sources, have increased dramatically since pre-industrial times [*Vingarzan*, 2004]. While better understanding of ozone chemistry has allowed for effective regulation of precursors in developed countries and is leading to a decrease in peak urban ozone concentrations, background ozone continues to increase due to possible outside influence [*Cooper et al.*, 2012].

Agriculture and air quality interact in numerous ways, and many of these interactions are depicted in Figure 1.1. Agriculture can affect air quality through land use change by changing the emissions of VOCs, which contribute to the formation of ozone and secondary organic aerosol (SOA), a component of PM, and by changing the deposition rate of PM and ozone themselves [*Wu et al.*, 2012]. Dust (largely PM_{10}) lofted from agricultural fields and feedlots [*Qi et al.*, 2015] and incomplete combustion from burning of crop residue also contribute to PM [*Lemieux et al.*, 2004]. Non-road vehicles used in the production and transport of agricultural products can have influences on air quality (NO_x and PM emissions) similar to on-road mobile sources [*US EPA*, 2015]. PM trapped within livestock buildings and high ambient ozone concentrations can have negative impacts on animal health [*Tan and Zhang*, 2004].

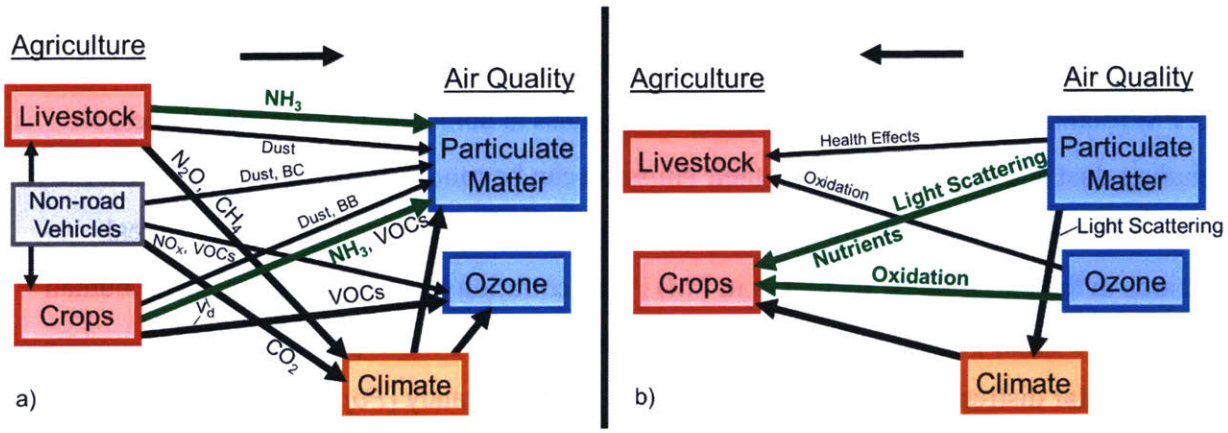

Figure 1.1. (a) Effects of agriculture (red) and agricultural production processes (gray) on air quality (blue). (b) Effects of air quality (blue) on agriculture (red). In both: Large arrows represent regional effects, while small arrows represent more local effects. Indirect effects act through climate (orange). Interactions studied in this thesis are shown in green.

Agriculture also affects air quality through its influence on climate. Nitrous oxide (N_2O) and methane (CH_4), additional byproducts from livestock production, and carbon dioxide (CO_2)

from non-road vehicles are greenhouse gases which are increasing the global mean temperature [*IPCC*, 2013]. Temperature increases affect the chemistry responsible for PM and ozone concentrations [*Seinfeld and Pandis*, 2006]. Climate change also alters meteorological parameters which control the stagnation events responsible for extremely high air pollution levels [*Horton et al.*, 2014] and the trajectory of long range pollution transport [*Fang et al.*, 2011]. Air quality influences agriculture through the scattering and absorbing properties of PM, which influence the climate variables important to productive crops, including precipitation and temperature [*Levy et al.*, 2013].

This thesis focuses on the remaining interactions between agriculture and air quality depicted in Figure 1.1, but not yet discussed. (1) Agriculture impacts air quality through the formation of inorganic $PM_{2.5}$ due to the emission of ammonia in the presence of atmospheric acids (Chapters 2 and 3). (2) Air quality modifies crop production through the scattering of light by PM, the damaging impact of ozone, and the transportation of nutrients (Chapters 4 and 5). We focus on these particular interactions because they are applicable to large-scale, global issues. In addition, we have access to and have developed expertise ourselves in the relevant chemical and radiative processes, and the appropriate tools and observations are available and accessible to further our understanding of these systems. Each interaction, including additional motivation, previous work and more specific objectives, is described in the following chapters.

Chapter 2. An Investigation of Ammonia and Inorganic Particulate Matter in California during the CalNex Campaign

Adapted from: Schiferl, L. D., C. L. Heald, J. B. Nowak, J. S. Holloway, J. A. Neuman, R. Bahreini, I. B. Pollack, T. B. Ryerson, C. Wiedinmyer, and J. G. Murphy (2014), An investigation of ammonia and inorganic particulate matter in California during the CalNex campaign, J. Geophys. Res. Atmos., 119, 1883–1902, doi:10.1002/2013JD020765.

2.1. Introduction

Atmospheric ammonia (NH_3) plays a key role in both the formation of fine particulate matter ($PM_{2.5}$) and in the biogeochemical cycling of nitrogen. Basic ammonia can act to neutralize the acidity of atmospheric acids, leading to the formation of inorganic aerosol (e.g., ammonium sulfate or ammonium nitrate). Understanding the formation of these aerosols is critical to addressing air quality issues, as exposure to particles has negative effects on human health [*Pope et al.*, 2009]. Aerosols can also impact climate, given their ability to adjust the energy budget of the planet through scattering and absorption of solar radiation and their role in cloud formation [*IPCC*, 2007]. Finally, the nitrogen contained in these aerosols can be transported and eventually deposited downwind, a particular concern for sensitive ecosystems [*Beem et al.*, 2010]. If nitrogen becomes oversaturated in the soil or aquatic ecosystems, environmental degradation through acidification and eutrophication may occur [*Erisman et al.*, 2007].

Prior to the development of industrial agriculture practices, the major sources of ammonia to the atmosphere included biomass burning, wild animals, and natural soils [*Holland et al.*, 1999]. Human population growth has increased the need for reliable food sources in the form of crops and livestock. The industrial production of ammonia as a fertilizer has increasingly supplied this need over the last century [*Erisman et al.*, 2008; *Sutton et al.*, 2008]. Thus, large agriculture operations now account for the majority of global ammonia emissions [*Dentener and Crutzen*, 1994]. These emission sources include fertilizers applied to plant crops and the waste by-products of domesticated animals, particularly those raised in large feedlots. Other sources of ammonia include industrial manufacturing processes, the ocean, fossil fuel combustion, and

automobile catalytic conversion [*Bouwman et al.*, 1997]. However, due largely to the challenges associated with in situ measurement of atmospheric ammonia [*von Bobrutzki et al.*, 2010] and local variations in emission control factors such as livestock diet and waste management and storage [*Hristov et al.*, 2011], uncertainties in these emissions and the subsequent transformations into the particle phase remain large.

Sulfur dioxide emitted into the atmosphere is oxidized to form sulfuric acid (H_2SO_4), which readily partitions to the aqueous phase, dissociating to produce sulfate (SO_4^{2-}). In the presence of atmospheric ammonia, a progression of salt formation occurs with increasing total ammonia levels: ammonium bisulfate to letovicite to fully neutralized ammonium sulfate. In higher relative humidity (RH) conditions and at lower total ammonia levels, the aerosol is more likely to stay in aqueous phase as a solution of component ions [*Seinfeld and Pandis*, 2006]. After all available sulfuric acid has been neutralized, the remaining ammonia can react with nitric acid (HNO_3) to form ammonium nitrate aerosol. Thus, ammonium nitrate formation generally occurs in areas of high ammonia and nitric acid and low sulfate concentrations. For ammonium nitrate, the gas and aerosol phases exist in equilibrium, dependent on temperature (T) and RH. Lower temperature and higher RH enhance partitioning to the aerosol phase. The phase of ammonium nitrate aerosol can vary between aqueous and solid as well, depending on the temperature, RH, and the history of RH (i.e., hysteresis of deliquescence). This thermodynamically coupled system, as well as the presence of additional species with displacement potential (e.g., NaCl, organic acids) in the same environment, complicates the formation and equilibrium of inorganic aerosol.

Much of California (CA) experiences high ambient concentrations of surface-level particulate matter. Both the Los Angeles (LA) Basin and the Central Valley are often in exceedance of the Environmental Protection Agency's (EPA) air quality standards for $PM_{2.5}$, which have been established to reduce the negative health effects caused by exposure to atmospheric particles. In particular, the 98th percentile of the 24 h $PM_{2.5}$ concentration inboth regions exceeded the standard of 35 $\mu g\ m^{-3}$ every year from 1999 to 2007 [*Cox et al.*, 2009]. The $PM_{2.5}$ in these areas of high human population and large agricultural production is largely composed of inorganic aerosol formed through acid-base neutralization, where urban centers are

a source of ammonia and NO_x ($NO + NO_2$) from mobile sources, which mix with ammonia from fertilizer and animal waste in agriculturally productive areas. Ammonia emissions in California are some of the highest in the country [*Goebes et al.*, 2003]. Sulfur dioxide is emitted from power generation and shipping near the coast. The topography of California also plays an important role in controlling $PM_{2.5}$ levels as the numerous valleys and mountain ranges allow for trapping and diversion of pollutants. Thus, it is particularly critical in California to understand inorganic $PM_{2.5}$ formation and the role of precursor emissions to achieve air quality compliance.

Observations made in the LA Basin show that inorganic $PM_{2.5}$ is formed from gas precursors in the urban core and that ammonia emissions from agriculture on the eastern side of the basin drive the conversion of nitric acid to nitrate downwind. Both emission of ammonia from volatilization and the transition of aerosol into the gas phase are more likely when temperatures are higher, such as due to daytime heating or during the summer months *[Russell and Cass*, 1986; *Chow et al.*, 1994; *Neuman et al.*, 2003; *Nowak et al.*, 2012]. Inorganic species are 50–60% of the $PM_{2.5}$ mass in the summer in the LA Basin and about 40% in the winter [*Chow et al.*, 1994; *Hand et al.*, 2012].

Although not as well studied, inorganic $PM_{2.5}$ formation in the Central Valley is becoming a larger concern as both human population and agriculture are currently growing at a rate higher than that in the LA Basin [*Hall et al.*, 2008]. The acidity of the region is determined by local sources, with complete neutralization of acids closer to high agricultural ammonia emissions sources [*Jacob et al.*, 1986; *Chow et al.*, 1996, 1998; *Neuman et al.*, 2003]. *Clarisse et al.* [2010] report summertime ammonia concentrations ranging from 10 to 20 ppb detected by the Infrared Atmospheric Sounding Interferometer (IASI) satellite instrument in the Central Valley. These ammonia concentrations are much larger than the 2 ppb observed outside the valley. Inorganic $PM_{2.5}$ makes up 25–35% of the total $PM_{2.5}$ here in the summer but 50% in the winter [*Chow et al.*, 1996; *Hand et al.*, 2012].

In this study, we use aircraft measurements made during the California Research at the Nexus of Air Quality and Climate Change (CalNex) campaign to investigate inorganic $PM_{2.5}$ formation and ammonia emissions in California as represented by the GEOS-Chem model. The

CalNex observations are particularly valuable for investigating inorganic aerosol formation as both gas-phase precursors and speciated aerosol were measured in this campaign. This includes a rare characterization of vertically distributed ammonia concentrations [*Neuman et al.*, 2003; *Nowak et al.*, 2012], which are challenging to measure in situ [*von Bobrutzki et al.*, 2010] and are a critical element to fine PM formation in California.

2.2. CalNex Airborne Observations

The CalNex field study (www.esrl.noaa.gov/csd/projects/calnex/) took place during May and June 2010 in California and the nearby Pacific coastal waters [*Ryerson et al.*, 2013]. For this analysis, we use in situ observations from 16 NOAA WP-3D aircraft flights throughout California (flight tracks shown in Figure 2.1). Aircraft sampling was generally conducted below 6 km altitude, with much of the flight time dedicated to the lower troposphere. The majority of flight time (about 80%) also occurred during the day.

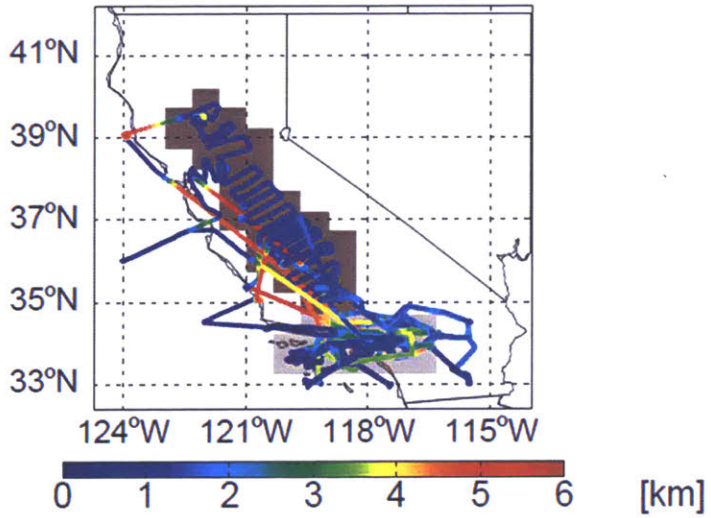

Figure 2.1. Location of 16 NOAA WP-3D flights during the CalNex field campaign (May–June 2010) used in this study, colored by aircraft altitude. Also shown are the two regions used in the analysis: Southern CA (shaded light gray) and the Central Valley (shaded dark gray).

In this study, we use CalNex observations of both gas- and particle-phase inorganic species concentrations. Ammonia was measured by chemical ionization mass spectrometry (CIMS) [*Nowak et al.*, 2007, 2012] with an average uncertainty of ± (30% + 0.2 ppb) (calibration uncertainty + measurement imprecision). This imprecision is determined from the variability in the periodic background measurements, which are interpolated for use in the calculation of the

ambient concentration (total signal–background) at each measurement. Sulfur dioxide was measured by pulsed UV fluorescence [*Ryerson et al.*, 1998] with an uncertainty of ±(15% + 0.5 ppb). Nitric acid was measured by CIMS [*Neuman et al.*, 2002] with an uncertainty of ±(15% + 0.052 ppb). The submicron particle ions were measured by aerosol mass spectrometry (AMS) [*Jayne et al.*, 2000; *Jimenez et al.*, 2003; *Bahreini et al.*, 2009] with an average uncertainty of ±30%. The aerosol concentrations are reported in μg sm^{-3}, where standard conditions are set to 1013.25 hPa and 0°C. The AMS nominally reports submicron aerosol mass concentrations [*Liu et al.*, 2007]; we note that this may represent an underestimate of fine aerosol mass when compared with the model simulation (see Section 2.3). Gas-phase nitrogen oxides, NO and NO_2, were measured by ozone-induced chemiluminescence [*Ryerson et al.*, 2000; *Pollack et al.*, 2010] with an approximate uncertainty of ±4%. The gas-phase species and meteorology parameters (T, RH) were reported at 1 s resolution and the particle ions at 10 s resolution. All observations are averaged to 1 min prior to analysis, and we retain only those minutes with valid measurements for all six of our key species (ammonia, nitric acid, sulfur dioxide, ammonium, nitrate, and sulfate). For comparison with the GEOS-Chem model, airborne CalNex observations are then gridded to the spatial and temporal resolution of the model (see Section 2.3.1).

2.3. GEOS-Chem Model Simulation

2.3.1. General Description

The GEOS-Chem chemical transport model (www.geos-chem.org) is used to interpret the CalNex plane flight observations. GEOS-Chem is driven by assimilated meteorology from the NASA Global Modeling and Assimilation Office; here we use the GEOS-5 product. For this analysis, we perform a series of nested simulations of GEOS-Chem v9-01-01 over North America for 2010 at 0.5° × 0.667° horizontal resolution with 47 vertical layers, typically seven layers within the lowest 1 km [*Wang et al.*, 2004; *Chen et al.*, 2009]. Boundary conditions are produced with the same version of the global model at 2° × 2.5° horizontal resolution.

The sulfate–nitrate–ammonium aerosol system, coupled to gas-phase chemistry, is represented in GEOS-Chem [*Park et al.*, 2004]. Gas-aerosol phase partitioning of these species is described by the thermodynamic equilibrium model ISORROPIA II [*Fountoukis and Nenes*,

2007] and dependent on local temperature and RH conditions. The implementation of ISORROPIA II in GEOS-Chem assumes that the species exist on the upper, metastable branch of the hygroscopic hysteresis curve, a valid assumption in all regions where the RH regularly exceeds the deliquescence relative humidity [*Pye et al.*, 2009], see Section 2.5.3 for further discussion. Gas and particle removal occurs via wet scavenging in convective and stratiform precipitation [*Mari et al.*, 2000; *Liu et al.*, 2001] as well as dry deposition based on surface layer resistances [*Wesely*, 1989]. These removal methods will be discussed in greater detail in Section 2.5.2. We include a fix for unreasonably low nighttime GEOS-5 planetary boundary layer (PBL) heights as described by *Heald et al.* [2012].

2.3.2. Inorganic Emission Inventories

Over the United States (US), anthropogenic emissions in GEOS-Chem follow the Environmental Protection Agency's National Emissions Inventory for 2005 (EPA NEI-2005). The NEI-2005 used in GEOS-Chem is a compilation of several inventories as described by *Kim et al.* [2011]. Emissions rates in NEI-2005 are reported for an August weekday, and these rates are temporally scaled in GEOS-Chem for individual species. For SO_x (sulfur dioxide + sulfate) and NO_x, an annual scale factor based on emissions trends as well as monthly and weekday/weekend scaling based on NEI-1999 is applied (since such scaling factors are not available from NEI-2005). Only monthly scaling is applied to ammonia emissions [*van Donkelaar et al.*, 2008], where this scaling is uniform across the US. Figure 2.2a shows the GEOS-Chem NEI-2005 emissions of ammonia, SO_x, and NO_x for May 2010 over both the continental US and zoomed in to California. Anthropogenic ammonia emissions (which include gasoline vehicles, livestock, agricultural fertilizer, and many smaller sources) are largest in agricultural areas, such as the Midwest, Great Plains, and the Central Valley of California. Additional ammonia emission hot spots occur over cities with high automobile usage, such as Los Angeles. Anthropogenic SO_x emissions are associated with electricity production, industrial processes, and near-coastal shipping activities. Anthropogenic NO_x emissions are largely from mobile sources in urban areas and interstate corridors.

Figure 2.2a also shows the seasonality of ammonia, SO_x, and NO_x emissions from all sectors in California. Anthropogenic sources provide the largest portion for all three species.

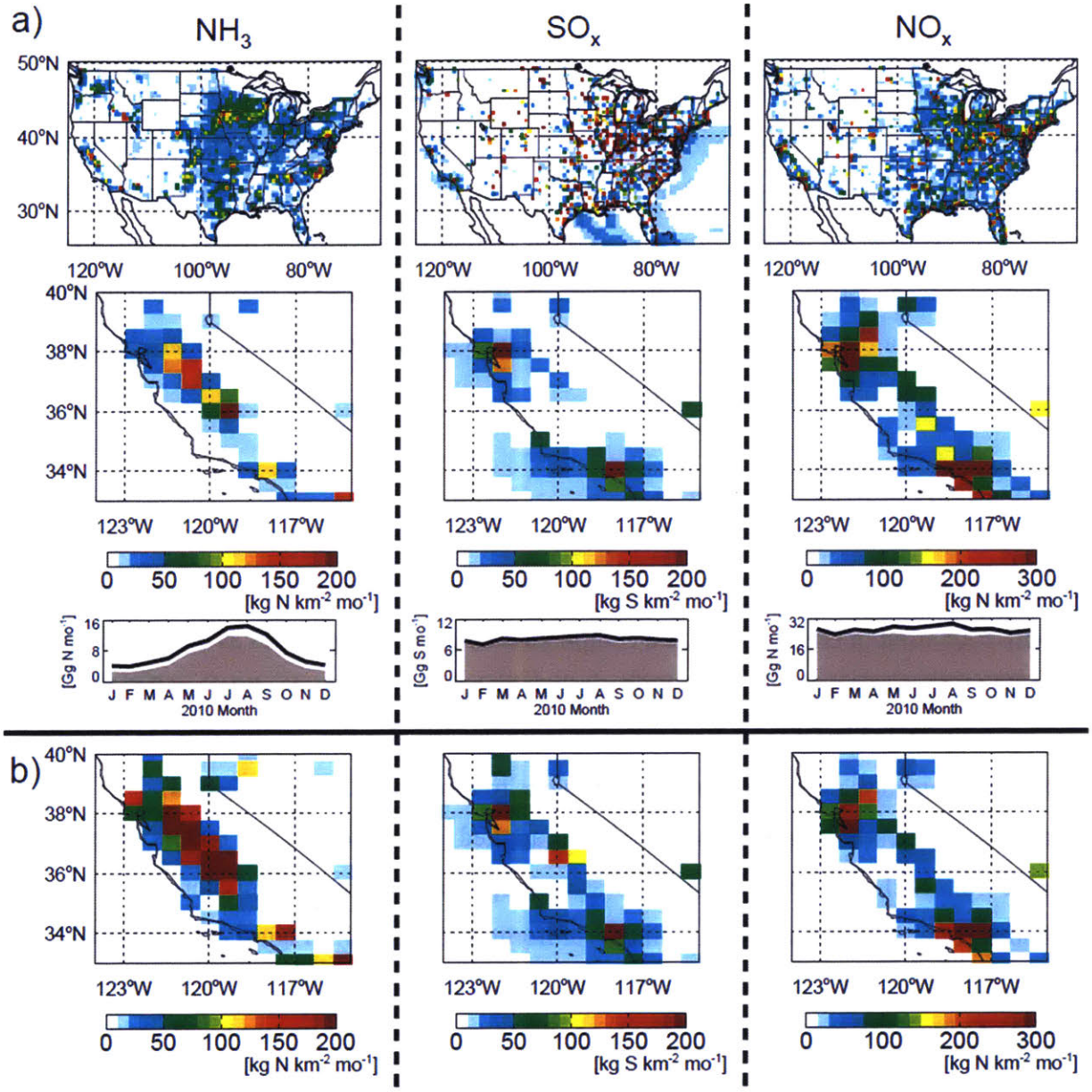

Figure 2.2. (a) May 2010 standard GEOS-Chem anthropogenic emission rate for ammonia, SO_x, and NO_x in the (top) United States and (middle) California. (bottom) Monthly total emission for each species over California in 2010: all sources (black line), anthropogenic sources only (shaded gray). SO_x emissions include ship sources over oceans. (b) May 2010 modified anthropogenic emission rate for ammonia, SO_x, and NO_x in California.

Only ammonia shows a strong seasonal variation, with a summer peak, representing the higher volatility corresponding to higher temperatures and increased agricultural activity. This seasonality is described by *Park et al.* [2004]. Total annual anthropogenic emissions over the domain in California shown for ammonia, SO_x, and NO_x are 75 Gg N yr^{-1}, 91 Gg S yr^{-1}, and 285 Gg N yr^{-1}, respectively.

Biofuel emissions, referring to burning of fuel for domestic use, such as heating and cooking by wood or coal, in GEOS-Chem generally follow the NEI-1999 inventory in the United States, which includes weekday and weekend emissions values. This is true for both SO_x and NO_x. Ammonia biofuel emissions, however, are from the 1990 Global Emissions Inventory Activity (GEIA) as described by *Bouwman et al.* [1997]. Biofuel has little variability throughout the year but does peak in the winter due to increased heating needs.

The Fire INventory from NCAR (FINN) [*Wiedinmyer et al.*, 2011] is used to describe the daily biomass burning emissions of particulate matter and reactive trace gases, including sulfur dioxide, NO_x, and ammonia, for 2010. In the US, emissions from biomass burning are the largest in the summer months, driven primarily from wildfires in the western states [*Wiedinmyer and Neff*, 2007]. For May 2010, biomass burning contributes 0.7% of ammonia emissions and 0.3% of NO_x emissions in California.

Natural ammonia emissions are also from the 1990 GEIA inventory and include emissions from natural ecosystems and the ocean. These natural emissions show a summertime peak similar to that of the anthropogenic sector and are the second largest category after anthropogenic sources, making up 13% of total ammonia emissions in California in May.

Lightning NO_x has been updated in GEOS-Chem v9-01-01 by *Murray et al.* [2012] to provide an improved parameterization through regional scaling. All other relevant emissions, such as soil NO_x, are described by *Pye et al.* [2009].

2.3.3. Previous GEOS-Chem Studies of Inorganic PM in the United States

A number of previous studies have evaluated the GEOS-Chem simulation of surface inorganic $PM_{2.5}$; we highlight here some recent relevant results. *Pye et al.* [2009] find that concentrations of inorganic aerosol are widely underpredicted over the entire United States, but they conclude that ammonia inventory errors are not the primary reason for these discrepancies and instead point to missing processes and low model horizontal resolution (horizontally $4° \times 5°$). *Zhang et al.* [2012], who also use the high-resolution nested version of GEOS-Chem used in this study, report little bias in NH_x (ammonia + ammonium) but significant positive biases for

nitric acid, ammonium, and nitrate, which they suggest may be associated with excess production of nitric acid from N_2O_5 hydrolysis. Based on comparisons with IASI satellite observations, *Heald et al.* [2012] suggest that California ammonia emissions are underestimated in the GEOS-Chem model, which leads to underproduction of nitrate at the surface in this region. Elsewhere in the US, they find a high bias in nitrate in all seasons except spring, consistent with *Zhang et al.* [2012]. *Walker et al.* [2012] also report an underestimate of surface ammonium nitrate concentrations in California. They suggest that a doubling of ammonia emissions is required to simulate annual observed nitrate concentrations in southern California, while even a tenfold increase in the Central Valley does not make up for the low bias in nitrate in that region. They also suggest that a high bias in the GEOS-5 mixed layer depth may account for some of the low nitrate bias, as particles are allowed to disperse into a greater volume near the surface.

2.4. Model Simulation of CalNex Observations

For this analysis, we separate the CalNex observations into two regions: the LA Basin and surrounding area, referred to here as the "Southern CA" region, and both the Sacramento and San Joaquin Valleys, referred to collectively here as the "Central Valley" region (shown in Figure 2.1). The demarcation is 34.75°N latitude, with about 75% of the observations over the Southern CA region and about 25% over the Central Valley. Measurements taken outside of these two primary regions (e.g., over the ocean, in the San Francisco Bay area) constitute about 15% of the number of total measurements from CalNex and are not included in our analysis. As shown by NEI-2005, the Southern CA region is dominated by NO_x and ammonia emissions from vehicles and industrial SO_x, especially within the Los Angeles core area. Ammonia emissions from agriculture dominate the Central Valley region. High NO_x emissions are seen over urban areas in the Central Valley, and SO_x emissions are quite low here compared to Southern CA (Figure 2.2a).

Given that the CalNex aircraft does not uniformly sample a grid box and that it is not possible for a coarse Eulerian model, such as GEOS-Chem, to reproduce plumes as concentrations diffuse through a grid box [*Rastigejev et al.*, 2010], any of the isolated high-concentration plumes observed during CalNex can bias the comparison with model concentrations. Thus, all averaging done in these comparisons will use median value in a grid

box or bin, rather than mean, as a test of model performance. Furthermore, plume-chasing aircraft sampling strategies can further bias the comparison between model and measurements. It is not clear to what degree this may impact our comparisons; we use regional averages throughout this study in an attempt to mitigate this effect.

The median concentrations of the six main species of interest (gases: ammonia, sulfur dioxide, nitric acid; and particle ions: ammonium, sulfate, nitrate) at all altitudes for both observations and the model are compared over the entire region in Figure 2.3. The model reproduces the general spatial distribution of these species, and particularly the transition from the Southern CA to Central Valley regions. However, the model substantially underestimates observed ammonia concentrations, by up to 24 ppb gridded median in the Central Valley, consistent with the underestimates reported by *Heald et al.* [2012] and *Walker et al.* [2012]. Sulfur dioxide in the model is noticeably low in the Central Valley as well, especially in the southern Central Valley. Model values for nitric acid and all three aerosol species are slightly underestimated in the southern Central Valley, and slightly overestimated on the northern end. Nitric acid, ammonium, and nitrate are slightly low in Southern CA. *Heald et al.* [2012] report a consistent low bias in simulated nitrate in southern California compared to surface observations in 2004 but little to no bias in mid-northern California. Except for ammonia, the median model biases for an individual grid box are less than 2 ppb (for the gas-phase species) or 2 $\mu g\ sm^{-3}$ (for the particle-phase species). Uncertainties in the observations are proportional to the measured concentration. Typical uncertainties in this region are 3 ppb for 10 ppb measured ammonia, 0.15 ppb for 1 ppb measured sulfur dioxide, 0.3 ppb for 2 ppb measured nitric acid, and 0.3 $\mu g\ sm^{-3}$ for 1 $\mu g\ sm^{-3}$ measured particle ion species.

Figure 2.4 compares the median vertical profiles of the inorganic gas and particle species in the Southern CA and Central Valley regions. The standard deviation of the observations in each altitude bin is also shown to denote the high degree of observed variability. Some of the high variability and vertical structure reported aloft reflects the limited number of observations at these altitudes, particularly in the Central Valley where the aircraft mainly sampled below 3 km altitude. In general, both the observations and the simulation agree that species concentrations decrease with increasing altitude due to surface sources and the short lifetimes of these species.

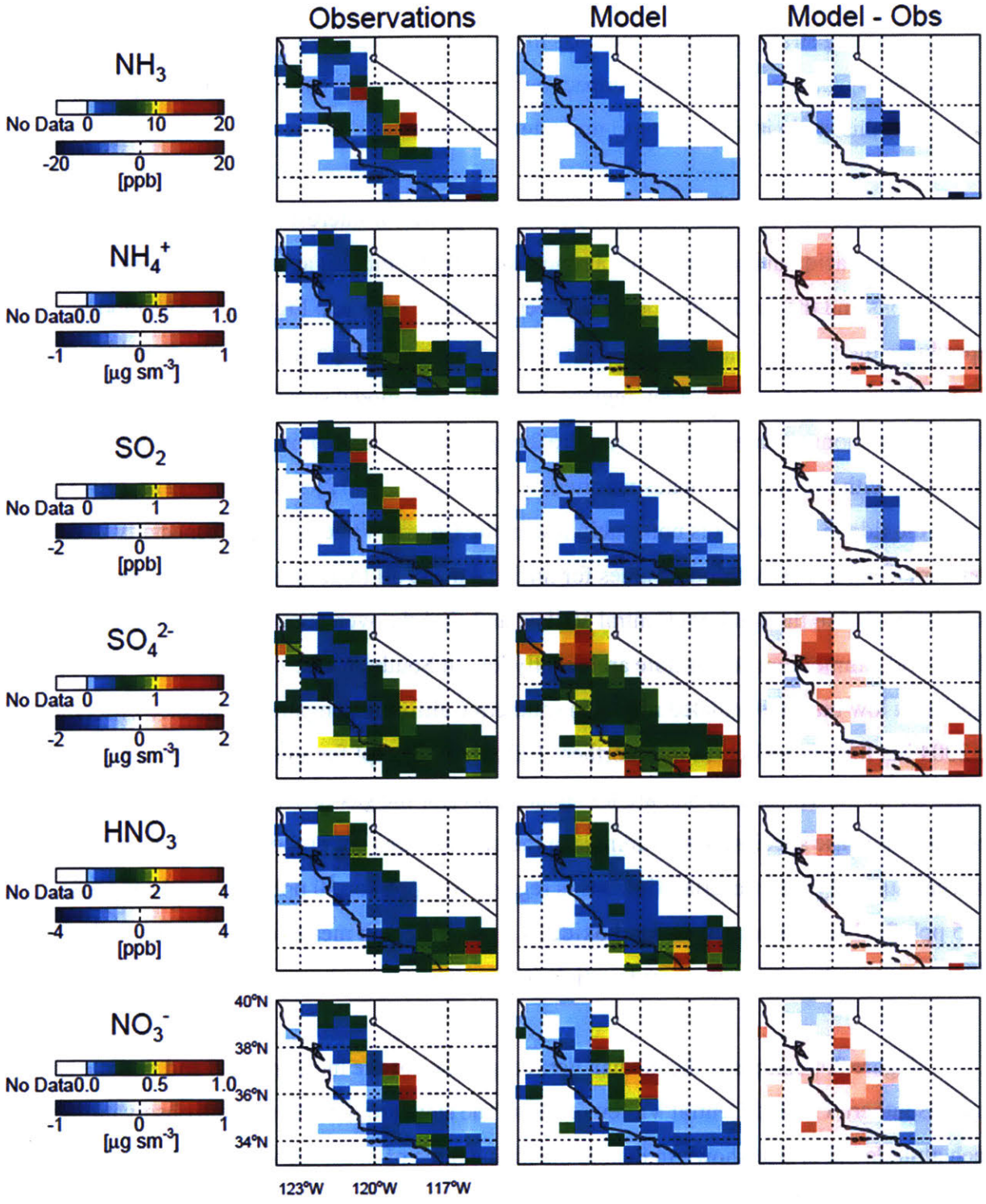

Figure 2.3. (left column) Median CalNex airborne observations and (middle column) median GEOS-Chem simulated concentrations along the flight paths averaged vertically over each grid box. (right column) Difference between observations and model. Color bars are saturated at respective values.

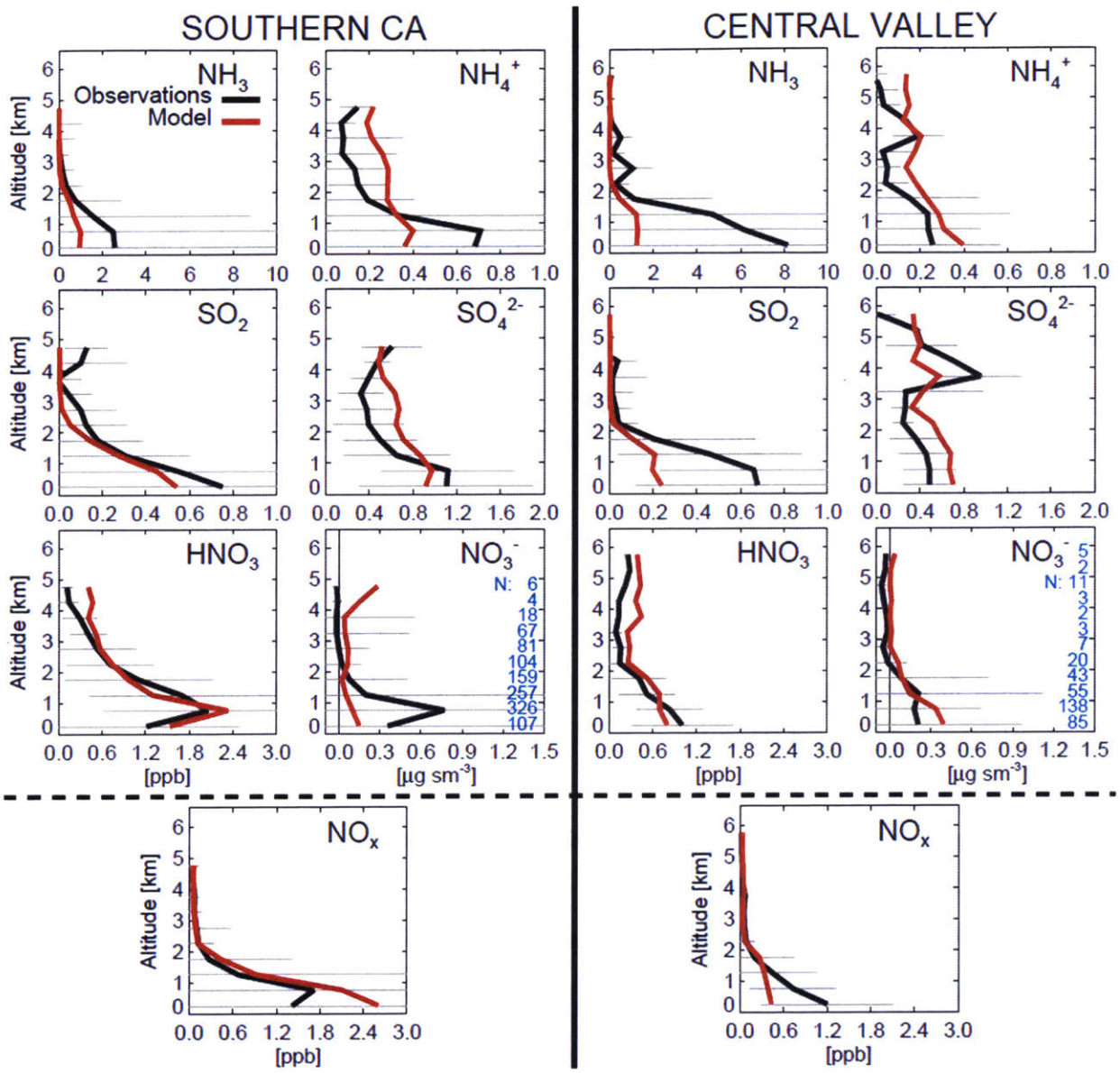

Figure 2.4. Vertical profiles of median CalNex plane flight observations (black) and median GEOS-Chem simulated concentration along those flight paths (red) averaged in 500 m altitude bins for the (top) six main gas precursors and particle ions and (bottom) NO_x as a precursor to nitric acid. The Southern CA region and Central Valley region are shown separately. The standard deviation of the observations in each altitude bin is shown in gray. The number of points in each bin is shown in blue.

Exception to this occurs in the near-surface layer, where deposition can reduce concentrations. Median model near-surface ammonia is biased low by a factor of 5 in the Central Valley and a factor of 2.5 in Southern CA. The model simulation of ammonium and nitrate is correspondingly low in Southern CA, consistent with an underestimate in ammonia precursor emissions. However, the model overproduces ammonium nitrate concentrations in the Central Valley despite the very low simulated ammonia concentrations, suggesting both that ammonium nitrate

formation is not ammonia limited in this region and that ammonium nitrate production is overestimated in the model. This is inconsistent with *Walker et al.* [2012] who find that 2009 surface nitrate concentrations are underestimated by the GEOS-Chem model throughout California; however, they apply different scaling factors to their emissions, and a direct comparison is not possible, as they do not provide emission totals for California. The model simulation in the Central Valley also suffers from an underestimate of sulfur dioxide levels by about a factor of 3 (below 2 km), with a simultaneous overestimate in near-surface sulfate. Although the nitric acid comparison is good in both regions, the simulated near-surface NO_x concentration, also shown in Figure 2.4, is biased high in Southern CA by 27% and low in the Central Valley by 52%.

The discrepancies between the CalNex observations and GEOS-Chem model simulation identified above could be due to several factors within the model. In the following section, we explore these factors, diagnose simulated sensitivities due to model uncertainties, and propose solutions to reconcile these differences.

2.5. Exploring the Sensitivities of the GEOS-Chem Simulation

2.5.1. Gas-to-Particle Partitioning

The ISORROPIA II thermodynamic equilibrium model in GEOS-Chem determines both the partitioning of ammonia into ammonium in order to neutralize sulfate and the partitioning of ammonium nitrate between the particle and gas phases. In GEOS-Chem, these calculations are based on the model ambient temperature and RH and the model concentrations of total ammonia, sulfate, total nitrate, sodium, and chloride. The concentration of ions present in submicron dust can also be treated in ISORROPIA II, but this is not included in the GEOS-Chem implementation due to the challenges of characterizing the variability in dust composition. Given the assumption of metastable equilibrium enforced by the GEOS-Chem model, ammonium nitrate particles remain deliquesced in ISORROPIA II through the lowest ambient RH levels (see Section 2.5.3 for further discussion).

Due to the sensitivity of ammonium nitrate equilibrium to temperature and RH, any bias in these parameters from the assimilated meteorology could affect the ammonium and nitrate

equilibrium concentrations. Figure 2.5 compares the observed and model (assimilated) meteorology for both the Southern CA and Central Valley regions. The median model temperature profile is generally biased low by about 1°C in both regions, with a modest overestimate near the surface in the Southern CA region. However, the model and observations are highly correlated, with linear regression slopes close to 1. The RH comparison is somewhat more scattered, as expected given the challenges of both measuring and predicting RH. The median model bias in RH for individual observations ranges from about 5 to 10%, in both directions, but no mean bias is evident.

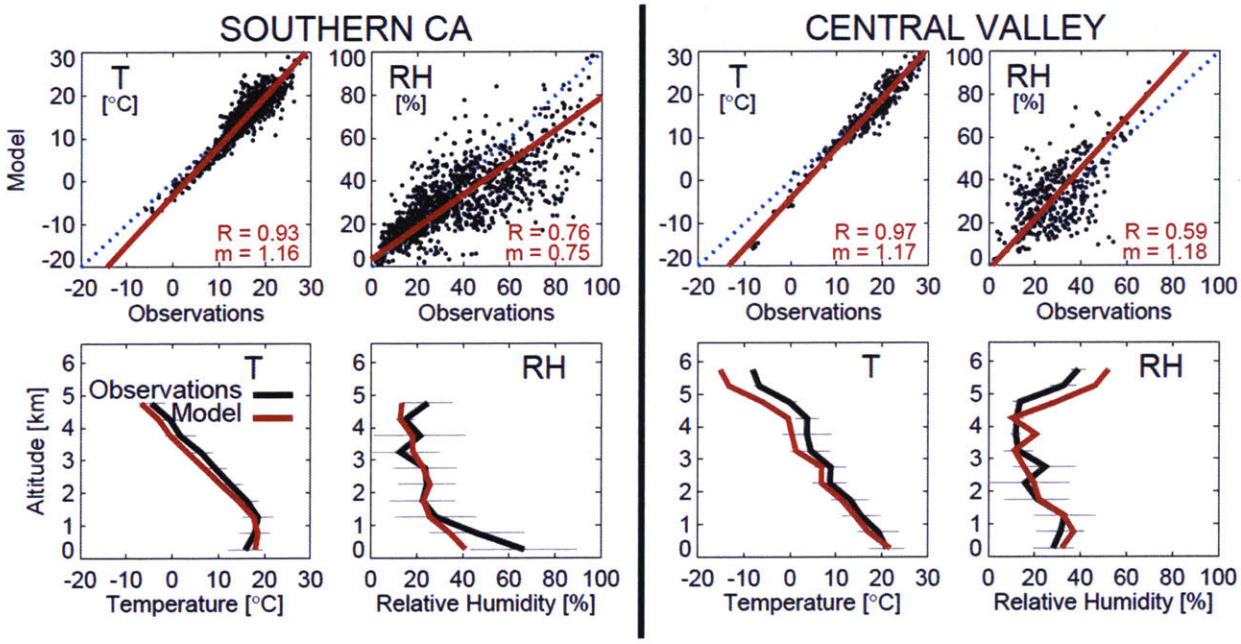

Figure 2.5. Comparison of CalNex plane flight observations and GEOS-Chem model meteorology along those flight paths for temperature (T) and relative humidity (RH). Southern CA region and Central Valley region are shown separately. (top) Scatterplots (orthogonal regression line in red, 1:1 line in broken blue, R is correlation coefficient, m is slope). (bottom) Median vertical profiles (as in Figure 2.4).

In order to determine the effects that these errors in meteorology (T, RH) could have on the simulated profiles, we perform a series of sensitivity simulations where the meteorological inputs into ISORROPIA II are varied. Given T and RH conditions experienced at the surface in California during this time of year, little sensitivity is expected; however, at the colder and drier condition aloft, errors in meteorology may more adversely affect the simulation. Thus, simulations are performed for ±1°C and ±10% RH from the original GEOS-5 values at all vertical levels. The impact of varying the temperature within the observed uncertainty on species concentration is very small with virtually no change in the median concentration profiles

(maximum variation in a vertical bin for any species is 0.2 μg sm^{-3}, not shown). The impact of varying RH is similarly small for all regions, except for nitrate concentrations aloft (maximum variation in a vertical bin of 0.5 μg sm^{-3} at 5 km), where limited observations are available to evaluate the simulation. Thus, we conclude that the simulation of nitrate concentrations below 3 km is not sensitive (less than 0.2 μg sm^{-3} variation) to the estimated uncertainty in model RH for the region. Overall, we conclude that model bias in temperature and RH during CalNex does not significantly impact the gas-to-particle partitioning in the model and cannot account for model bias in the simulation.

Chloride ion (Cl^-) can impact the fine inorganic PM system discussed here in two ways. First is from the reaction of sea salt (NaCl) with nitric acid, which leads to the formation of sodium nitrate ($NaNO_3$) while releasing hydrochloric acid (HCl). In GEOS-Chem, only accumulation mode sea salt is included in the calculation of the gas-aerosol equilibrium state with ISORROPIA II. Second is through the neutralization reaction of hydrochloric acid with ammonia to form ammonium chloride (NH_4Cl). Hydrochloric acid for this reaction is typically emitted directly from urban sources [*Kaneyasu et al.*, 1999], which are not included in GEOS-Chem. We find that AMS-observed airborne chloride concentrations during CalNex were low (less than 1.2 μg sm^{-3} at all points) throughout the region studied. This chloride measured is typically in the form of ammonium chloride, rather than sea-salt chloride [*Canagaratna et al.*, 2007]. The model overpredicts the median chloride concentrations by a factor of 2, suggesting that, while the comparison is not exact, the missing hydrochloric acid sources in the model are not critical for predicting chloride levels. Sensitivity tests verify that reducing simulated chloride concentrations to observed levels (or less) does not significantly impact the equilibrium of ammonium nitrate formation in the model (less than 0.1 μg sm^{-3} mean concentration change near the surface). Therefore, there is little evidence that we are missing a substantial source of ammonium or nitrate in the form of sodium nitrate or ammonium chloride in our simulation of California.

ISORROPIA II represents only the equilibrium partitioning of fine particles; therefore, any possible sink of nitric acid onto coarse sea salt or dust is not represented here. However, the comparison of Figure 2.4 does not suggest that we are missing a large nitric acid sink in

California, as simulated nitric acid values are within 20% of observations at all altitudes. While we have neglected the impact of organic acids and dust on nitrate formation in the GEOS-Chem simulation, we do not expect either to play a dominant role in the inorganic gas-particle system or the simulation biases described here as concentrations of these species are low during California summer [*Fairlie et al.*, 2010; *Myriokefalitakis et al.*, 2011].

2.5.2. Wet and Dry Deposition

Wet deposition processes allow for the removal of chemical species from the atmosphere as they are incorporated into precipitation. GEOS-Chem uses wet deposition schemes by *Liu et al. [2001]* for aerosols and *Mari et al. [2000]* for gases to determine how much of a given species is removed. These schemes are driven primarily by the presence of convection and precipitation within the meteorological input parameters.

Over the California domain shown in Figure 2.1, the NH_x wet deposition flux makes up a much smaller fraction of total NH_x deposition than dry deposition (0.8 Gg N $month^{-1}$ mean wet deposition compared to 2.2 Gg N $month^{-1}$ mean dry deposition for May and June 2010). The CalNex time period represents the driest season in California. Most of the precipitation occurs over the mountains to the east of the Central Valley. As this is largely driven by the regional meteorology, wet deposition of SO_x and total nitrate follows similar seasonal patterns.

We use monthly mean wet deposition measurements from the National Atmospheric Deposition Program National Trends Network (NADP/NTN) (nadp.sws.uiuc.edu/ntn) at nine sites in California in 2010 to test the simulated wet deposition in GEOS-Chem. The observations and model agree that wet deposition levels of all three ion species in May and June are low, both in absolute terms (Figure 2.6) and compared to other times of the year (not shown). The comparison of observed and simulated mean wet deposition fluxes in Figure 2.6 shows a slight model underestimate of wet deposition at sites east of the Central Valley, but these sites are outside of the domain of the aircraft measurements. Thus, wet removal does not control the budget of trace gases and particles over California in this season, and biases in the GEOS-Chem simulation cannot be attributed to this process.

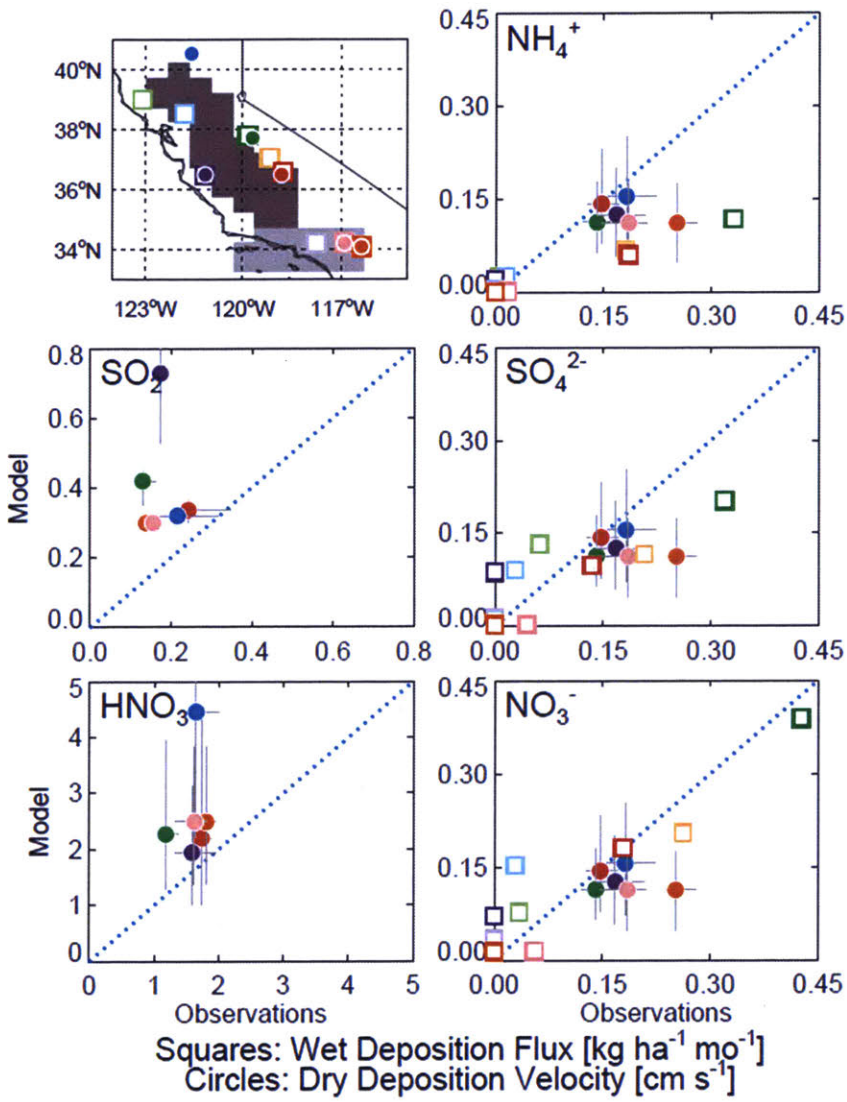

Figure 2.6. Scatterplots of mean May–June 2010 NADP/NTN and GEOS-Chem wet deposition flux at nine sites (squares) and CASTNET and GEOS-Chem dry deposition velocity at six sites (circles) in California. Site locations are shown in upper left; 1:1 line is shown in broken blue. Gray lines represent extent of minimum and maximum weekly observed and daily model velocity values. Ammonia dry deposition is not measured by CASTNET. Only wet deposition of ions is measured by NADP/NTN.

GEOS-Chem uses the *Wesely* [1989] resistance parameterization for dry deposition. This scheme combines aerodynamic resistance, boundary layer resistance, and canopy surface resistance terms to calculate a deposition velocity. This deposition velocity is combined with the ambient species concentration to determine the dry deposition flux.

Dry deposition of gaseous ammonia dominates the simulated NH_x mass loss to deposition during May and June in California (63% of total NH_x deposition, 85% of NH_x dry deposition).

Similarly for SO_x and total nitrate, the dry deposition of the gas species dominates that of the aerosol. Dry deposition of nitric acid clearly dominates the total nitrogen deposition throughout California in May and June, accounting for 6.9 Gg N $month^{-1}$ of the 11 Gg N $month^{-1}$ mean total nitrogen deposition (63%). This is consistent with US nitrogen deposition budget reported by *Zhang et al.* [2012], where nitric acid dry deposition makes up the largest portion of total nitrogen deposition annually throughout the US. Simulated May 2010 dry deposition velocities over land in California range from 0.3 to 0.5 cm s^{-1} for ammonia and from 0.2 to 4.0 cm s^{-1} for nitric acid. These velocities are highly affected by land type and density of vegetation.

Average dry deposition velocity values from seven California sites in the EPA Clean Air Status and Trends Network (CASTNET) (www.epa.gov/castnet) are compared with GEOS-Chem for May and June 2010 in Figure 2.6. CASTNET does not report ammonia dry deposition velocities. It is critical to note that the dry deposition velocities from CASTNET are derived quantities from the Multilayer Model. Thus, the comparison with GEOS-Chem is in fact a comparison of two models. However, we use these comparisons to provide an estimate of potential bias in the GEOS-Chem simulation. Based on these few point sites for comparison, the model deposition velocity is biased high for sulfur dioxide and nitric acid and somewhat low for the aerosols.

We conduct a sensitivity simulation to test whether these potential biases in dry deposition velocity may contribute to the discrepancies between the simulation and the CalNex observations. In this simulation, sulfur dioxide and nitric acid dry deposition velocities are reduced by 50%, lowering the minimum sulfur dioxide velocity from 0.3 cm s^{-1} to 0.2 cm s^{-1}, and the aerosol dry deposition velocity is increased by 70%, all changed to match the CASTNET values. The impacts of this change on sulfur dioxide are small. The near surface median sulfur dioxide concentration in Southern CA is increased by 0.04 ppb, nearly halving the bias in this region. A relatively insignificant increase of about 0.03 ppb is seen in the Central Valley. Nitric acid experiences a larger change in the near-surface concentration in both regions, with median increases of 0.37 ppb in Southern CA and 0.12 ppb in the Central Valley. This creates an overestimation in nitric acid in Southern CA and matches the CalNex observations in the Central Valley. The increase in nitric acid also enhances ammonium nitrate formation. The overall

change is larger in the Central Valley however, where the ammonium nitrate increase in Southern CA is completely offset by increased aerosol deposition. Only a small decrease in concentration, less than 0.03 $\mu g\ sm^{-3}$ for all aerosol species, can be attributed to the change of the aerosol dry deposition velocity alone. While the improvement in surface sulfur dioxide concentration in Southern CA and nitric acid concentration in the Central Valley made by altering the dry deposition velocities corrects much of the original discrepancy for those species seen in Figure 2.4, confidence in the derived CASTNET values is low, and thus, it is not clear that the bias in sulfur dioxide and nitric acid can be correctly attributed to errors in dry deposition velocity. We note that the dry deposition velocities of ammonia have not been evaluated against observations; although, a similar 50% decrease in simulated ammonia dry deposition velocity does not produce any significant changes to the species concentrations simulated for CalNex (nor do we see any significant change in concentrations under the extreme test of reducing ammonia dry deposition velocities by 90%). The modest sensitivity of the simulation to the assumed sulfur dioxide and nitric acid dry deposition velocities suggests that this could be a small source of bias in the model simulation.

2.5.3. Emissions

Given the changes in human and livestock populations in parts of California as well as changes in mitigation technology, the NEI-2005 used in GEOS-Chem may not adequately describe our study period in 2010. *Russell et al.* [2012] indicate that NO_2 concentrations have decreased by about 30% in cities across the US, including near LA, between 2005 and 2011 due to increased emission controls. This likely accounts for the model overestimate of NO_x in the Southern CA region shown in Figure 2.4. As for ammonia, the total number of cattle, a key source of ammonia, in the San Joaquin Valley increased by 24% from 2002 to 2010 (United States Department of Agriculture California livestock inventory (www.nass.usda.gov/ca)), creating a large emissions underestimate. Applying ammonia emissions inventories correctly is also difficult given the variety of waste management and dietary factors which can affect the local emission levels at a given time.

We investigate the magnitude of adjustment to the NEI-2005 anthropogenic emissions which can reconcile our model simulation with the CalNex observations. Our initial comparisons

showed that the model ammonia concentrations were low throughout California, but this difference is much greater in the Central Valley. Figure 2.7 disaggregates the NEI-2005 California ammonia emissions into two key source sectors: livestock and on-road mobile sources. This clearly delineates the livestock ammonia emission in the Central Valley region and the on-road mobile ammonia source in the Southern CA region, as well as in the vicinity of San Francisco. We investigate the impact of increasing the livestock ammonia emission by a factor of 5 over the entire inventory area in our modified simulation. In addition, using the same CalNex airborne measurements as in this study, *Nowak et al.* [2012] show that the NEI-2005 ammonia emissions are quite low for the eastern side of the LA Basin, where many dairy operations exist. They report a measured ammonia emission rate of 12–64 Gg yr^{-1} from livestock in this eastern LA region, compared to the NEI-2005 rate of about 0.37 Gg yr^{-1}. We set the livestock ammonia emission rate in the single east LA model grid box consistent with the region discussed by *Nowak et al.* [2012] to 12 Gg yr^{-1} in our modified simulation. This is more than 30 times the original value rather than the 5 times increase imposed elsewhere. Although not yet available in gridded format, the NEI-2008 version 3 (www.epa.gov/ttnchie1/net/2008inventory.html) supports a large growth in livestock ammonia emissions in California, compared to NEI-2005: a doubling in the Central Valley and 17 times increase in Southern CA.

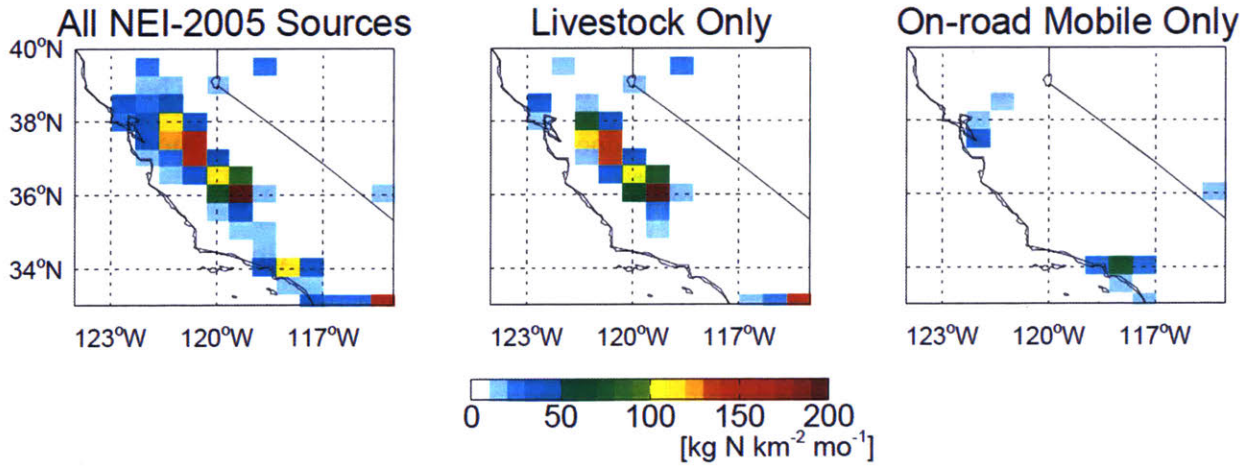

Figure 2.7. NEI-2005 ammonia emissions in GEOS-Chem for May 2010 over California: all sources, livestock only, and on-road mobile only.

The model sulfur dioxide concentrations are underestimated in the Central Valley as well. This low bias is larger in the southern Central Valley region than in the north. In an effort to better represent observed concentrations, we increase the northern and southern Central Valley

sulfur dioxide emission by 3 times and 10 times, respectively, in our modified simulation. This increases the Central Valley mean May 2010 SO_x emission rate from 3 kg S km^{-2} $month^{-1}$ to 31 kg S km^{-2} $month^{-1}$. This model underestimate of sulfur dioxide concentrations in the Central Valley may be related to upwind urban sources (e.g., from Fresno, Sacramento, Bay Area) or local sources of sulfur dioxide. However, we are unable to attribute this discrepancy based on the observations used here. This requires further exploration. The scaling factors selected are based solely on the observed bias in the baseline simulation (Figure 2.4). We also implement a 30% reduction in anthropogenic NO_x emission from the NEI-2005 values based on *Russell et al.* [2012]. The new May emission rates for anthropogenic ammonia, SO_x, and NO_x in the modified GEOS-Chem simulation are shown in Figure 2.2b. The annual anthropogenic emissions rates over the California domain shown are now 280 Gg N yr^{-1}, 118 Gg S yr^{-1}, and 209 Gg N yr^{-1} for ammonia, SO_x, and NO_x, respectively.

Vertical profiles comparing the results from the modified emissions simulation with the standard run are shown in Figure 2.8. In the Southern CA region, the low ammonia concentration bias is overcorrected by the increased emissions. The increase in emissions compensates for much of the bias in ammonia in the Central Valley; however, a pronounced near-surface underestimate remains. The low bias in sulfur dioxide concentrations is halved in the Central Valley and completely eliminated in Southern CA. Increased ammonia emissions in both regions act to neutralize more nitric acid, decreasing its concentration while promoting ammonium nitrate aerosol formation. The NO_x concentration comparison in Southern CA is much improved with lower NO_x emissions, while a low bias remains in the Central Valley. However, this drop in NO_x creates a modest low bias in nitric acid near the surface in both the Central Valley and Southern CA which is much larger than the nitric acid decrease caused by the ammonia increase alone. Excess dry deposition of nitric acid in the model (discussed in Section 2.5.2) may also contribute to this underestimation. Inorganic aerosol concentrations increase in both regions due to increased availability of ammonia and sulfur dioxide. This substantially improves the simulation of inorganic $PM_{2.5}$ in Southern CA but worsens the already high-biased simulation of ammonium and sulfate in the Central Valley and produces an overestimate in nitrate (consistent with the US-wide overestimate in nitrate concentrations reported by *Heald et al.* [2012]). We

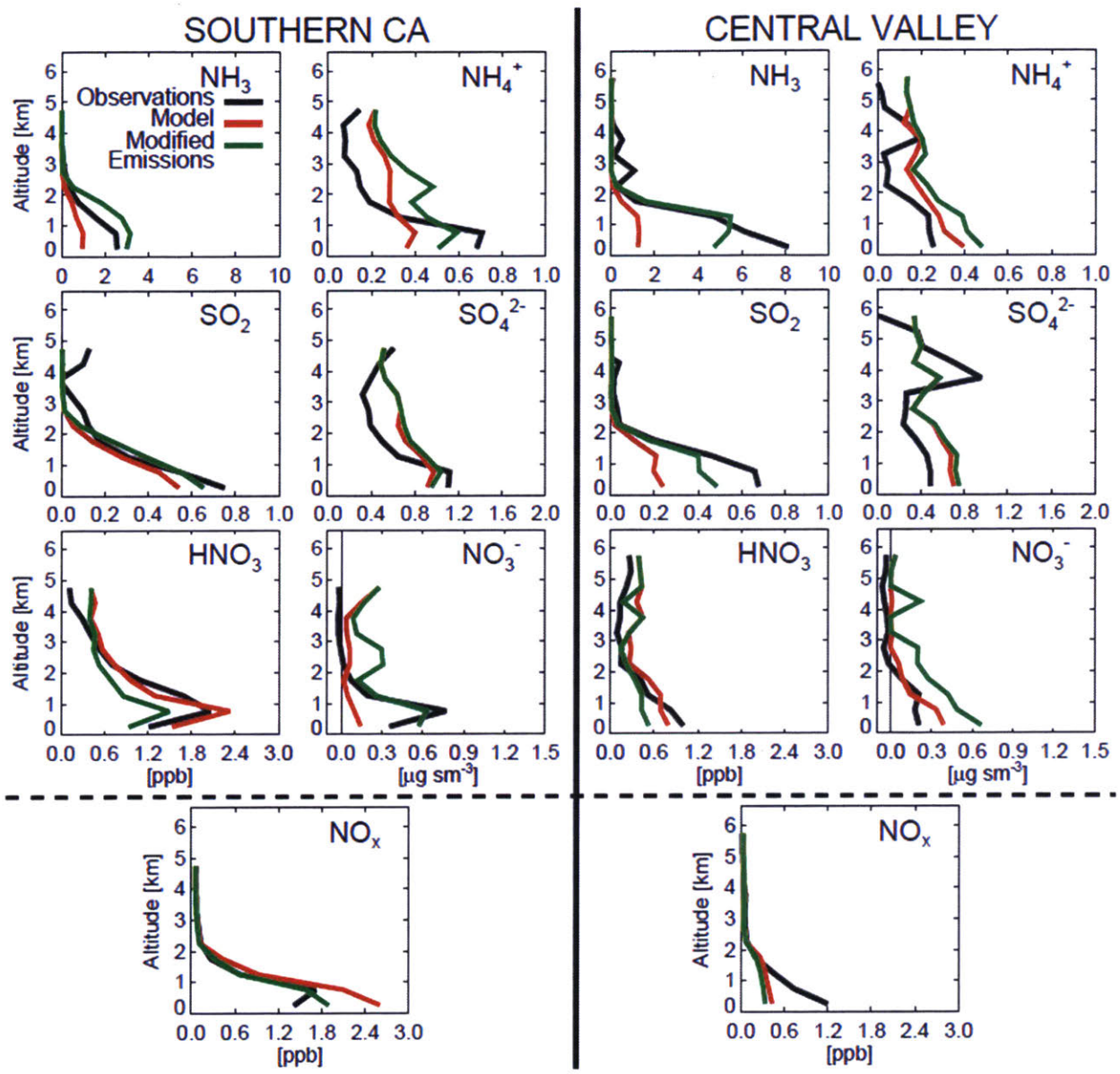

Figure 2.8. Same as Figure 2.4 but with vertical profiles resulting from the GEOS-Chem simulation with modified emissions added in green. The number of points per bin remains the same.

note here that these comparisons may also be influenced by the AMS size cutoffs which may underestimate the fine PM mass concentrations when compared to the model.

The results of these emissions modifications, in concert with the sensitivities explored in Sections 2.5.1 and 2.5.2, suggest that uncertainties in the GEOS-Chem simulation of the inorganic gas-particle system are dominated by emissions. Accurate emission inventories are critical to the ability to effectively model reactive nitrogen and $PM_{2.5}$ formation in California. The emissions modifications we have made are the largest source of concentration variation and

the closest we have come to reducing initial errors among the factors examined in Section 2.5. However, we note that we have applied uniform scaling factors to the NEI-2005, where emission trends likely differ considerably at the county level.

Figure 2.9 summarizes the near-surface air quality and inorganic $PM_{2.5}$ composition for our two regions in California by comparing the CalNex airborne observations with the standard and modified emissions GEOS-Chem simulations. The CalNex observations show that, below 1 km, inorganic $PM_{2.5}$ concentrations are about three times as high in Southern CA as in the Central Valley, with median concentrations of 2.47 and 0.91 $\mu g\ sm^{-3}$, respectively. However, the relative speciation of inorganic fine PM is similar across California (sulfate contributes 50% and nitrate makes up about 25%, both by mass).

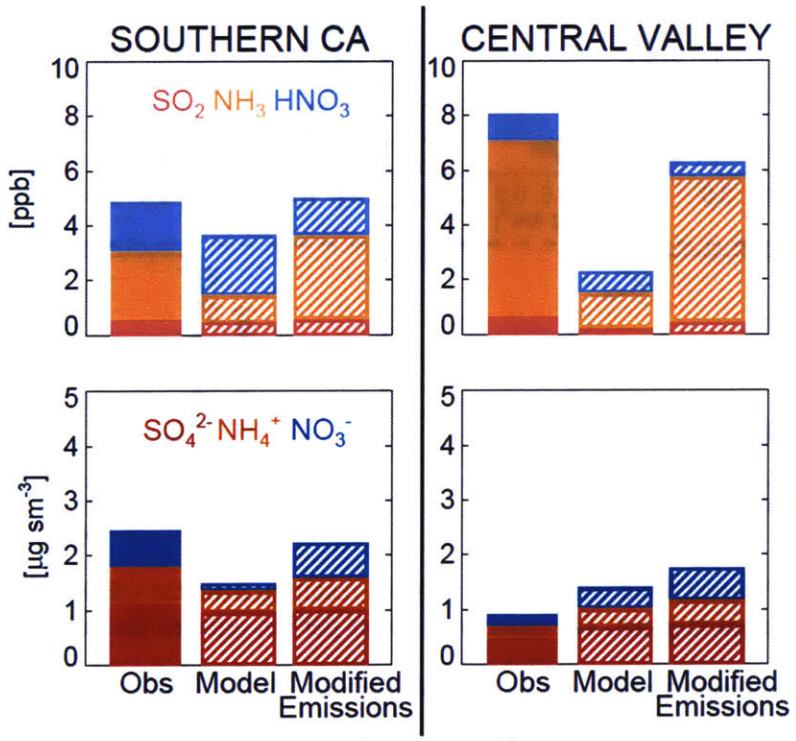

Figure 2.9. Median species concentrations below 1 km. Comparing (top) gases species with (bottom) aerosol species, Southern CA region with Central Valley region for three cases: CalNex airborne observations, standard GEOS-Chem simulation, and simulation with modified emissions.

On a more local scale, both CalNex airborne observations and GEOS-Chem simulation (with updated emissions based on *Nowak et al.* [2012]) capture the formation of ammonium nitrate downwind of LA as the oxidized NO_x emitted from the city core reacts with large amounts of ammonia from farms to the east of LA. Observed near-surface inorganic $PM_{2.5}$ in

East LA is 24% higher than in LA (4.32 μg sm^{-3} compared to 3.48 μg sm^{-3}) and is made up of 44% nitrate compared to 34% in LA. The modified simulation better captures the higher ammonium nitrate concentration in East LA, producing 3.57 μg sm^{-3} inorganic $PM_{2.5}$ compared to 1.65 μg sm^{-3} in the standard simulation.

Increasing ammonia, sulfur dioxide, and decreasing NO_x emissions as described in the modified simulation decreases the overall regional biases seen in the initial comparison of the observations and standard GEOS-Chem (Figure 2.9). Comparison of gas species is improved or consistent with the initial comparisons in both regions. Aerosol concentrations in Southern CA are also greatly improved, especially for ammonium and nitrate. The largest remaining discrepancy is the simulated Central Valley inorganic particle concentrations, which are initially too high (by 51%) compared to the observations and are increased further with the modified emissions (now 89% overestimate). This occurs despite the continued underestimate of the gas-phase precursors in the same region of 23%. One possible cause of this particle mass overestimate could be the deliquescence assumptions applied in the model. Ammonium nitrate deliquescence exhibits a hysteresis, where the RH exposure history of the particle dictates whether the particle is deliquesced when exposed to RH between the crystallization and deliquescence RH. Given that a three-dimensional model cannot track this particle history, an assumption that the particle remains on the upper deliquesced branch (metastable) or lower crystallized branch (stable) must be applied. In the GEOS-Chem model, the default is the use of the metastable assumption, which is appropriate under higher RH conditions [*Pye et al.*, 2009]. However, under the dry summertime conditions in California, this assumption may be erroneous. In Figure 2.10, we examine this behavior by comparing the difference in the simulated nitrate concentrations predicted under the modified emissions scenario with the stable and metastable assumption along the CalNex flight tracks. Using a stable assumption, which allows for both solid and liquid aerosol, rather than only liquid as in the metastable assumption, generally reduces ammonium nitrate formation. This occurs throughout California, except in conditions when both nitric acid and ammonia concentrations are sufficiently high to exceed the equilibrium constant for the solid formation of ammonium nitrate, seen, for example, at the surface in LA. In terms of the median comparisons presented in Figures 2.8 and 2.9, the stable assumption eliminates about half of the ammonium nitrate overestimate in the Central Valley, but at the

same time, it degrades the comparison with ammonium nitrate observations in Southern CA. This may represent a key uncertainty in the simulation of ammonium nitrate in relatively dry locations. However, we see from Figure 2.10 that in Southern CA, the median and the mean difference in concentrations due to this shift in ammonium nitrate formation regime are of opposite sign. Thus, the relative importance of this effect likely varies with location and evaluation metric. The true particle history is also likely a mixture of hydration and dehydration, suggesting that our metastable and stable simulations bracket the "true" ammonium nitrate formation conditions. Other possible causes of the overprediction of ammonium nitrate in the Central Valley include a missing loss mechanism, insufficient ventilation or poor representation of transport and export from the Central Valley due to insufficiently resolved terrain, or underestimation of the fine PM mass observed with AMS. Further investigation is required to improve the PM simulation in this challenging region.

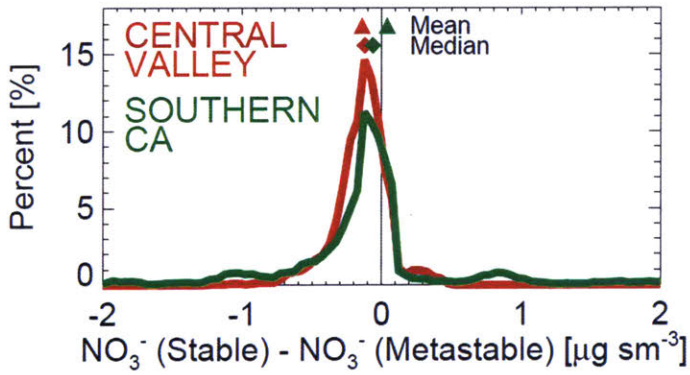

Figure 2.10. Histograms show the difference in simulated nitrate concentrations along the CalNex flight tracks over the Central Valley (red) and Southern CA (green) when applying the stable versus metastable assumption in the GEOS-Chemmodel. All simulations are shown with modified emissions scenario (described in Section 2.5.3). Also displayed are the mean (triangle) and median (diamond) values for each distribution. All differences for the Central Valley are within the given range, while 4% of Southern CA differences are above 2 µg sm^{-3} and 1% are below –2 µg sm^{-3}.

Finally, ammonia emissions likely peak in the afternoon due to the influence of temperature on the volatility of ammonia and increased anthropogenic activity (farming practices, vehicle operation) during the day [*Pinder et al.*, 2006a]. However, ammonia emissions in GEOS-Chem remain constant throughout the day, and this could be another limitation on the model's ability to represent surface-level air quality. In Figure 2.11, we explore the sensitivity of the diurnal pattern of regional surface ammonia, ammonium, and nitrate concentrations to both the diurnal profile of ammonia emissions and the mixing depth for May–June 2010. By emitting

ammonia in a daytime pulse and raising the overnight PBL height by 50 hPa (an arbitrary value chosen to test sensitivity), we see that the simulated diurnal pattern of surface concentrations of ammonia and ammonium nitrate are highly sensitive to these factors. The sensitivity to ammonium nitrate formation is higher in Southern CA, which is ammonia limited. Except for the increase in surface ammonia concentration in the Central Valley, midday concentrations appear unaffected, while the nighttime differences are on average a factor of 2. There is little impact on sulfate concentrations under both of these scenarios (not shown). This suggests that characterizing the diurnal trend in both emissions and mixing depth is critical to accurately simulating hourly fine PM exposure. We note that the model simulation of predominantly daytime airborne measurements during CalNex is virtually insensitive to these factors. Further investigation, with a large data set of hourly measurements in multiple seasons, is required to further investigate the processes controlling the diurnal variability of fine inorganic PM in California.

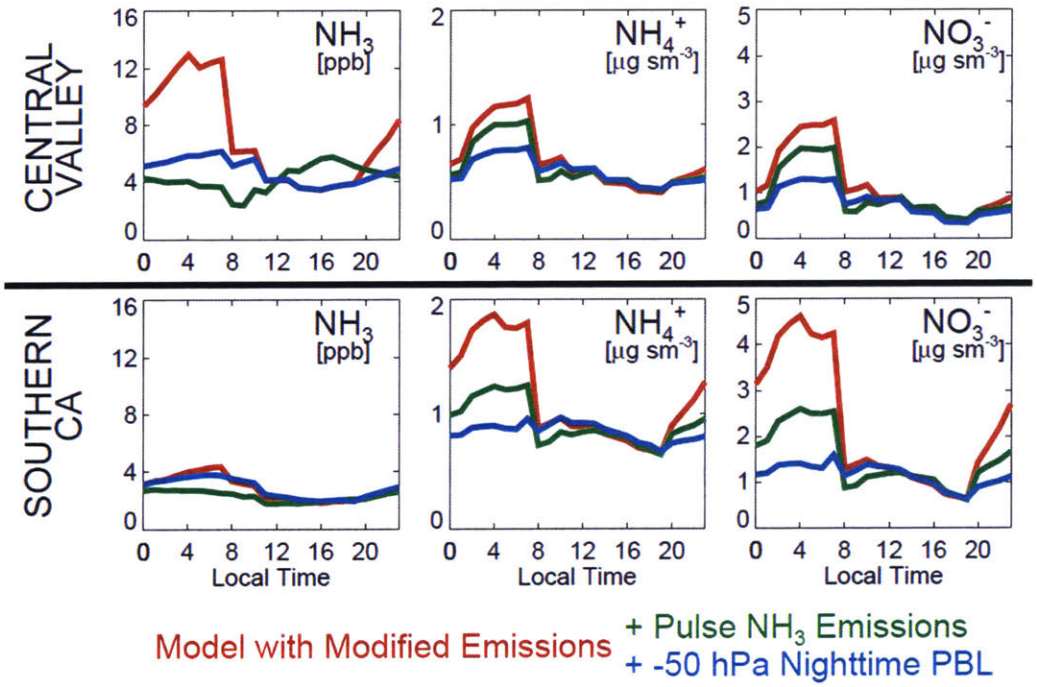

Figure 2.11. Hourly mean regional surface concentrations of (left column) ammonia, (middle column) ammonium, and (right column) nitrate for May–June 2010 simulated with GEOS-Chem: standard simulation with modified total emissions (red), afternoon pulse of ammonia emissions (green), and lifting of the overnight PBL by 50 hPa (blue). All simulations include the modified total emissions described in Section 2.5.3.

2.6. Application of Modified Emissions to Year-Round Surface Air Quality in California

We use this same modified emissions simulation, based on the summertime CalNex period evaluation, to investigate the year-round inorganic $PM_{2.5}$ formation and surface-level concentrations in California. In Figure 2.12, observed and simulated surface inorganic $PM_{2.5}$ concentration and percent mass composition are compared at nine EPA Air Quality System (AQS) sites in California (six in Central Valley, three in Southern CA) (www.epa.gov/ttn/airs/airsaqs) for 2010. Ion species discussed here are collected on a nylon filter after $PM_{2.5}$ inlet, extracted and analyzed using ion chromatography. The model is sampled for valid observation days for the grid box containing each of the sites. The seasonality of the simulated concentrations generally compares well with the observations in both regions, supporting the validity of the emissions modifications year round and the model's usefulness to address air quality issues throughout the year. The notable exception is the high bias in simulated nitrate in the Southern CA region through the summer and fall. However, the AQS sites in the Southern CA region are close to LA and represent near-source air masses rather than the regional averages shown elsewhere in this study, and therefore, reported concentrations are higher. Ammonium nitrate formation is highly sensitive to changes in NH_x and total nitrate under these conditions, so a slight high bias in either of these, perhaps due to overly rapid oxidation of NO_x to nitric acid, could cause an overprediction of the particle mass. The mean ammonium nitrate concentrations at the surface shown here are not sensitive to the stable/metastable assumption in the model, consistent with *Heald et al.* [2012]. This is the result of both somewhat higher RH conditions at the surface, and an averaging out of localized increases and decreases (refer to Figure 2.10). The only exception to this is in LA where concentrations of nitric acid and ammonia are consistently high enough to promote greater ammonium nitrate formation under stable conditions. However, this leads to a maximum regional mean increase in nitrate of about 0.5 $\mu g\ sm^{-3}$ at the Southern CA sites and makes up at most about 25% of the difference between model and observations in Figure 2.12.

Figure 2.13 contrasts the mean regional simulated surface concentrations for both gas and aerosol species in the Southern CA and Central Valley regions in June and December. These results are insensitive to the stable/metastable assumption in the model. In the Central Valley, the

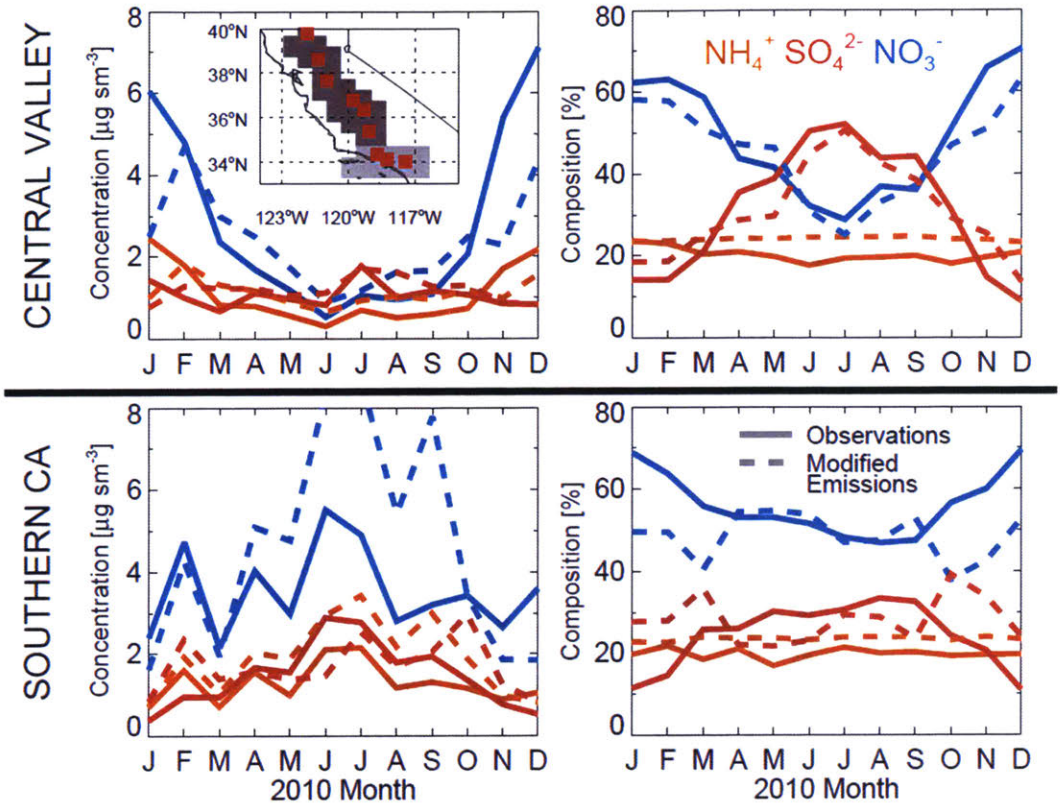

Figure 2.12. Mean monthly surface concentrations and percent of total particle species for 2010 in California. Comparing EPA Air Quality System (AQS) sites (solid line) and GEOS-Chem simulation with modified emissions (dashed line) in each of two regions. Simulated values are sampled for grid box corresponding to surface site and days with valid observed concentrations.

mean regional simulated surface inorganic aerosol concentrations are three times higher in December (7.07 µg sm^{-3}) compared to June (2.32 µg sm^{-3}). This relative change is supported by the seasonal variation shown by the AQS observations. Despite wintertime ammonia emissions reductions, there remains abundant available ammonia in the atmosphere in the Central Valley. The nitrate fraction of inorganic PM in the Central Valley increases from 30% in June to 64% in December. A higher wintertime frequency of inversion events and a lower mean PBL height trap pollutants in the Central Valley region and contribute to these higher PM levels. The mean simulated PBL height in this region decreases from 1.7 km in June to 0.7 km in December. About 75% of the simulated increase in ammonium nitrate is due to effects of the lower wintertime PBL height, while the remainder is due to colder temperatures enhancing ammonium formation balanced with lower ammonia emissions. Given this high sensitivity, PBL height measurements could be useful to investigate whether the modest ammonium nitrate underestimate in the winter, shown in Figure 2.12, is a result of errors in meteorology and/or

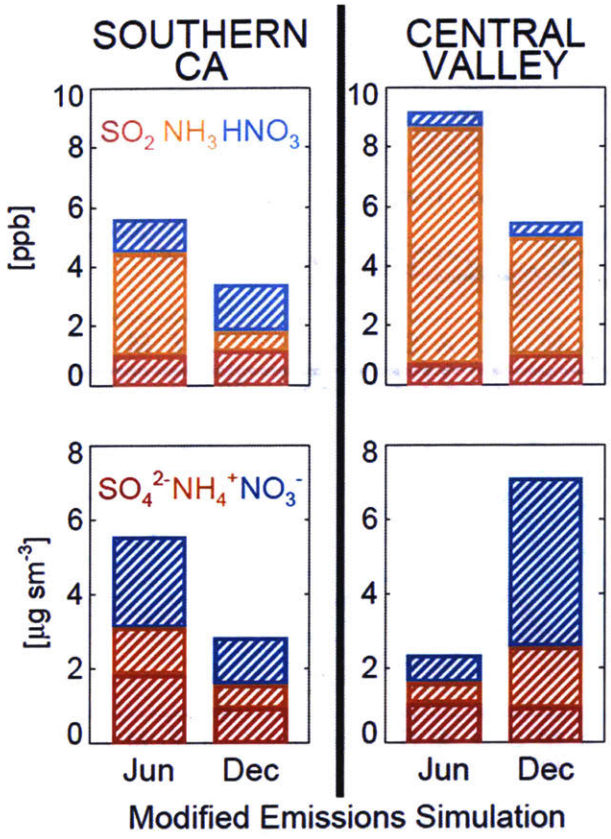

Figure 2.13. Regional mean simulated species concentrations at the surface for June and December 2010 for model with modified emissions. Comparing (top) gas species with (bottom) aerosol species. Southern CA region on left with Central Valley region on right.

mixing. Frequent winter rain, cloud, and fog activity in the Central Valley can also accelerate the deposition of PM species during this time [*Jacob et al.*, 1986]. This removal counters the increase in sulfate production which occurs when more liquid water is available, leaving sulfate concentrations relatively constant throughout the year.

Conversely, in Southern CA, the simulated regional mean inorganic $PM_{2.5}$ concentration is two times lower in December (2.80 µg sm^{-3}) than in June (5.52 µg sm^{-3}), while the relative composition of the inorganic $PM_{2.5}$ remains the same. The thermodynamic potential for ammonium nitrate formation and total nitrate levels is comparable in Southern CA and the Central Valley in the wintertime. However, unlike in the Central Valley, the Southern CA region is ammonia limited in the winter. While the relative wintertime decrease in ammonia emissions is similar in both regions, the absolute ammonia supply is considerably lower in Southern CA, restricting ammonium nitrate formation. This effect is larger than seasonal changes in

temperature and PBL height, which are more moderate than in the Central Valley, and would otherwise increase the ammonium nitrate concentrations. Like in the Central Valley, the wintertime change in sulfate concentration is a balance between increased production and wet deposition. A series of widespread, gas- and particle-phase concentration measurements (with colocated profilers to help characterize mixing depth) are required to further investigate the relative role of emissions, meteorology, and mixing on surface PM air quality in California in different seasons.

By removing all anthropogenic ammonia emissions from our simulation with modified emissions, we estimate that about 40–60% of surface inorganic $PM_{2.5}$ in California during the summer and up to 78% in the Central Valley region in the winter (56% in the Southern CA) are attributable to anthropogenic sources of ammonia. Ammonia that is not partitioned into aerosol or deposited near its emission region can be transported, given the proper meteorological conditions, and react or be deposited elsewhere. This excess ammonia often occurs due to the very large emission rates in certain areas, such as in the Central Valley. Future flight campaigns in these remote areas or the use of space-based remote sensing instruments could help evaluate the effects of increasing ammonia emissions on air quality and ecosystems downwind of the CalNex region.

2.7. Conclusions

We have evaluated the representation of the ammonia and inorganic aerosol system in the GEOS-Chem chemical transport model using aircraft observations from the CalNex campaign in May and June 2010. Initial comparisons of observations with the simulation show underprediction of ammonia and sulfur dioxide in two regions in California, near LA and the Central Valley. Median concentrations of ammonium, sulfate, and nitrate are underpredicted near LA as well but overpredicted in the Central Valley. NO_x is overpredicted in the region near LA.

Sensitivity analysis of several processes within the model indicates that underestimated/ overestimated emissions are most likely to account for model biases. Increasing anthropogenic emissions of ammonia and sulfur dioxide enhance inorganic PM formation in both regions. A decrease in anthropogenic NO_x, as suggested by *Russell et al.* [2012], counters some of this

formation. These modifications reduce the initial model bias in all species, except aerosols in the Central Valley. This suggests that the NEI-2005 does not adequately describe livestock ammonia and anthropogenic NO_x throughout California and anthropogenic sulfur dioxide sources in the Central Valley. This trend is consistent with the trends in emissions suggested by the NEI-2008. Furthermore, we find that ammonium nitrate concentrations simulated along the CalNex flight tracks may be sensitive to thermodynamic assumptions made in the model, but this sensitivity is negligible for mean surface concentrations (with the exception of LA).

We use this model with improved emissions to investigate surface inorganic fine PM, which contributes to poor air quality in California. The simulated concentrations confirm observations, where inorganic $PM_{2.5}$ is highest in the Central Valley during the winter and highest in Southern CA during the summer. June $PM_{2.5}$ concentrations are more than a factor of 2 higher near LA than in the Central Valley. This is reversed in December when ammonium nitrate formation is favored in the Central Valley. Central Valley inorganic $PM_{2.5}$ concentrations are three times as high during this time than in June. Nitrate accounts for the largest portion of mass and seasonal variation in fine inorganic PM in both regions. Unlike in most of the US, inorganic $PM_{2.5}$ in California is not dominated by sulfate, so ammonia emissions control could be an effective method to lower the inorganic $PM_{2.5}$ concentration in the region. Our simulations suggest that more than half of the inorganic $PM_{2.5}$ throughout California is produced as a result of anthropogenic ammonia emissions.

The remaining reservoir of ammonia in the Central Valley indicates that the formation of inorganic $PM_{2.5}$ and its associated air quality degradation could dramatically increase should the concentration of atmospheric acids increase. This seems possible given current projections of southern Central Valley human population: about 20% increase over 2010 population by 2020 and 60% increase by 2040 [*State of California*, 2012]. However, advances in emissions technology and implementation may counteract some or all of the effects of population growth [*Steiner et al.*, 2006]. The balance of these trends will likely dictate future $PM_{2.5}$ air quality in California.

Chapter 3. Interannual Variability of Ammonia Concentrations over the United States: Sources and Implications

Adapted from: Schiferl, L. D., C. L. Heald, M. Van Damme, L. Clarisse, C. Clerbaux, P.-F. Coheur, J. B. Nowak, J. A. Neuman, S. C. Herndon, J. R. Roscioli, and S. J. Eilerman (2016), Interannual variability of ammonia concentrations over the United States: sources and implications, Atmos. Chem. Phys., 16, 12305–12328, doi:10.5194/acp-16-12305-2016.

3.1. Introduction

The modern agricultural system developed to feed an increasing human population relies heavily on artificially produced reactive nitrogen in the form of ammonia (NH_3). The intensification of agricultural practices has significantly perturbed the global nitrogen cycle over the past century, including increases in ammonia emissions into the atmosphere [*Galloway and Cowling*, 2002; *Erisman et al.*, 2008; *Sutton et al.*, 2008]. Agricultural ammonia emissions contribute to inorganic fine particulate matter ($PM_{2.5}$ formation (e.g., ammonium sulfate and ammonium nitrate) in the atmosphere [*Seinfeld and Pandis*, 2006]. $PM_{2.5}$ has numerous negative effects on human health, including respiratory and cardiovascular distress and an overall decrease in life expectancy [*Pope et al.*, 2009]. Agriculture has a large impact on $PM_{2.5}$ throughout the world, contributing up to 40% of premature mortality due to outdoor air pollution in parts of Europe [*Lelieveld et al.*, 2015]. In the United States (US), ammonia emissions from agriculture exports alone react to increase population-weighted $PM_{2.5}$ concentration domestically by 0.36 $\mu g\ m^{-3}$, with contributions greater than 1 $\mu g\ m^{-3}$ in parts of the Midwest [*Paulot and Jacob*, 2014]. Thus, the regulation of ammonia emissions may have the potential to reduce $PM_{2.5}$ in ammonia-limited areas [*Pinder et al.*, 2006b], and in a sulfate-limited environment (sulfate = SO_4^{2-}), ammonia can play a more important role, leading to ammonium nitrate formation. However, this potential for ammonia emissions reductions to reduce $PM_{2.5}$ may be decreasing as sulfur dioxide (SO_2) and NO_x (nitric oxide (NO) + nitrogen dioxide (NO_2) regulation is implemented in the US [*Holt et al.*, 2015]. $PM_{2.5}$ also contributes to reduced environmental visibility and affects the radiative budget of the earth [*IPCC*, 2013]. Finally, the release of excess nitrogen from agricultural sources into the atmosphere will also increase nitrogen deposition fluxes, which can cause negative ecosystem effects such as acidification and eutrophication

[*Erisman et al.*, 2007]. This is of particular concern in sensitive ecosystems such as alpine terrain and wetlands [*Beem et al.*, 2010; *Ellis et al.*, 2013].

The magnitude and timing of the ammonia emissions from agriculture are generally less well understood than for other anthropogenic emissions (e.g., mobile sources of NO_x, power plant emissions of SO_x (SO_2 + sulfate)). A sticky gas, ammonia is difficult to measure in situ, and this can lead to a low bias in measured concentrations [*von Bobrutzki et al.*, 2010]. The paucity of observational constraints has also limited the evaluation of emission inventories and the resulting $PM_{2.5}$ formation simulated by models. Agricultural emission inventories are often based on emission factors from animals or fertilizers under certain field conditions, which are generalized to known populations or mass applied, respectively. These conditions are highly variable due to meteorology, local livestock diet, and waste management and storage [*Hristov et al.*, 2011]. Recent studies have established that these bottom-up inventories often underestimate ammonia emissions due to difficulties in effectively scaling the low-biased measurements [*Walker et al.*, 2012]. Studies in California, in particular, show evidence of this ammonia underestimate in areas with rapidly increasing livestock populations, and they encourage improvements in ammonia emissions estimates to better predict $PM_{2.5}$ [*Nowak et al.*, 2012; *Schiferl et al.*, 2014]. This is a key finding in Chapter 2. Models that underestimate the ammonia emissions will underestimate the surface $PM_{2.5}$ if sufficient acid is available, negatively affecting air quality management. However, *Paulot et al.* [2016] suggest that ammonium nitrate formation globally is more limited by nitric acid (HNO_3) than ammonia, and that the uncertainty associated with the formation of nitric acid via N_2O_5 uptake has a greater impact on ammonium nitrate formation than the uncertainty associated with ammonia emissions. Regardless, as regulations in the US restrict SO_2 and NO_x, the proportion of reactive nitrogen deposition is shifting from oxidized to reduced forms [*Pinder et al.*, 2011; *Lloret and Valiela*, 2016], and thus the need to understand ammonia emissions and their role in the environment is growing. This importance has been recognized as new observations of ammonia have become available over longer time periods and with more spatial coverage.

Given these new observations and their relevance to understanding inorganic $PM_{2.5}$ formation, our goal is to understand the factors that control ammonia concentrations and their

variability in the atmosphere. This study uses newly available observations to investigate the variability of ammonia in the US during a 5-year time period (2008–2012). We first identify observed ammonia variability and investigate the ability of a chemical transport model to reproduce these observations. Then, we attribute sources of the model ammonia concentration variability and use known relationships in an attempt to more accurately represent the variability of agricultural ammonia emissions.

3.2. GEOS-Chem Model Simulation

3.2.1. General Description

We use the GEOS-Chem chemical transport model (www.geos-chem.org) to simulate ammonia concentrations over the US. The scenarios described throughout this paper are driven by GEOS-5 assimilated meteorology for 2008 to 2012from the NASA Global Modeling and Assimilation Office. We use v9-02 of the GEOS-Chem model in a nested configuration over North America at a horizontal resolution of 0.5° × 0.667° [*Wang et al.*, 2004; *Chen et al.*, 2009]. The chemistry and transport time steps for these nested simulations are 20 and 10 min, respectively. A global simulation at 2° × 2.5° horizontal resolution is used to generate the boundary conditions necessary for the nested simulations. There are 47 vertical layers in all cases. The representation of the sulfate–nitrate–ammonium aerosol system and its relevant precursor gases in the standard version, including emissions, chemistry, and deposition schemes, generally remains as that described previously in Chapter 2. Briefly, the coupling of gas-phase chemistry to aerosol chemistry in GEOS-Chem is described by *Park et al.* [2004]. The gas-particle partitioning of ammonium nitrate is calculated by ISORROPIA II [*Fountoukis and Nenes*, 2007] as implemented by *Pye et al.* [2009], where the aerosols are assumed to exist on the metastable branch of the hygroscopic hysteresis curve. Relevant modifications from v9-01-01 used in Chapter 2 to v9-02 used here include updates to the seasonal cycle of the US Environmental Protection Agency's (EPA) National Emissions Inventory for 2005 (NEI-2005) ammonia emissions [*Zhang et al.*, 2012] and to the algorithm controlling soil NO_x emissions *[Hudman et al.*, 2012] (described in Section 3.2.2).

3.2.2. Emissions and Emission Trends in Base Scenario

The "base scenario" referred to in this analysis incorporates modifications to the standard GEOS-Chem v9-02 simulation that have been made to the emissions in order to more accurately represent the study time period. In the base scenario, annual scale factors applied to anthropogenic SO_x and NO_x emissions to capture the emissions trends over time (which end in 2010 in the standard model version) are extended uniformly spatially to 2011 and 2012 from EPA Trends data (www.epa.gov/ttn/chief/trends/). Mean anthropogenic SO_x, largely from power generation, and NO_x, largely from automobiles, emission rates over the US in summer (JJA) 2008 are 18 mg S km^{-2} s^{-1} and 16 mg N km^{-2} s^{-1}, respectively. As shown in Figure 3.1, anthropogenic SO_x and NO_x emissions are highest in the eastern US and are often associated with rural point or dense urban sources. These emission rates decrease by 30 and 33%, respectively, by 2012. The majority of the magnitude of these decreases occurs in the eastern regions of the US. For 2008, anthropogenic SO_x makes up 98% of total SO_x emissions, and anthropogenic NO_x makes up 65% of total NO_x emissions. Other major sources of NO_x with large interannual variability are soils and fertilizer use. In the entire US, these summertime emission rates vary from –23 to +20% of the mean from 2008 to 2012, with most of the variability occurring in the Plains and the Midwest regions. The soil and fertilizer NO_x emission rates are simulated online and are controlled by a combination of nitrogen storage and meteorology [*Hudman et al.*, 2012]. In 2012, high temperatures increase soil and fertilizer NO_x emissions, offsetting the decrease in anthropogenic NO_x emissions (Figure 3.1).

As in the standard version, our base scenario uses anthropogenic ammonia emissions from the EPA NEI-2005 inventory, which includes livestock, fertilizer, and non-agricultural sources. These emissions are for August and scaled uniformly spatially each month as determined by *Zhang et al.* [2012]. The summer mean anthropogenic ammonia emission rate for the US is 12 mg N km^{-2} s^{-1}. Livestock and fertilizer use comprise 71 and 15% of this emission rate, respectively. This proportion is unrealistically constant throughout the year as the scaling above does not, for example, account for springtime crop fertilization. The Plains and the Midwest exhibit higher total anthropogenic emission rates of 20 and 19 mg N km^{-2} s^{-1}, respectively, with larger contributions from agriculture. The spatial distribution of these high

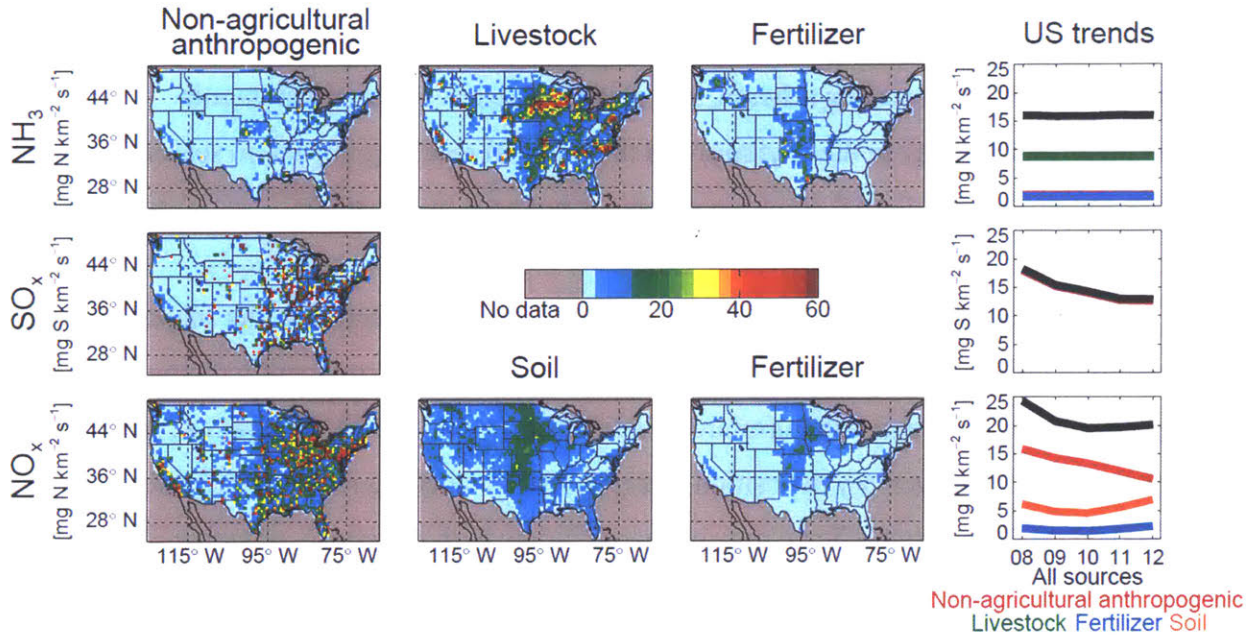

Figure 3.1. Summer (JJA) (top row) ammonia, (middle row) SO_x, and (bottom row) NO_x emissions as implemented in the GEOS-Chem base scenario. Maps show values for 2008; US emission rate shown for 2008 through 2012 on the right. Color bar is saturated at 60; local values may exceed this emission rate. Data outside the continental US are not shown here, nor in all subsequent figures.

ammonia emission regions are shown in Figure 3.1. For the entire US, anthropogenic ammonia emissions make up 78% of the total ammonia emissions in the summer. Other sources include natural emissions (16%), biofuel (3.7%) and biomass burning (1.8%). Biomass burning emissions are highly variable over the study period (by a factor of 2), which causes slight differences in the proportions mentioned above. In our base scenario, we use daily biomass burning emissions from the Fire INventory from NCAR (FINN) through 2012 [*Wiedinmyer et al.*, 2011]. Given a nearly constant rate of ammonia emission and the large changes in NO_x emissions mentioned above, changes in the ammonia concentrations may be driven by changes in the acid supply, which would affect gas-particle partitioning of ammonium nitrate and the overall $PM_{2.5}$ concentration.

There is no diurnal or interannual variability in the ammonia emissions in our base scenario. When we implement a diurnal emission scaling determined by the local daily diurnal surface temperature profile, the mean surface summer ammonia concentration in the US is reduced by 12% (1.62 ppb without vs. 1.43 ppb with diurnal emission scaling). This mean value is heavily influenced by a large daily overnight decrease in concentration of 24%, while the

daytime concentration decrease is minimal, only 1%. There is substantial uncertainty associated with any diurnal emission scaling scheme, and given its modest impact on ammonia concentrations (particularly in the daytime) and the minimal resulting impact on seasonal mean $PM_{2.5}$ concentrations, the diurnal emission scheme is not used in this study.

We have not included any scheme that accounts for the bidirectional flux (deposition and re-emission) of ammonia in our base scenario. Rather, ammonia is permanently removed via wet scavenging in convective and stratiform precipitation [*Mari et al.*, 2000; *Amos et al.*, 2012] and via surface resistance-driven dry deposition [*Wesely*, 1989]. Ongoing research suggests that a unidirectional dry deposition scheme may be inappropriate with regards to ammonia [*Massad et al.*, 2010; *Zhang et al.*, 2010]. Under a bidirectional scheme, ammonia can be either taken up or re-emitted by a plant based on the comparison of the ambient ammonia concentration with a varying compensation point (an ambient concentration greater than the compensation point leads to deposition). Re-emitted ammonia has the potential to affect ecosystems farther downwind. Failing to account for this re-emission may locally cause an overestimation in dry deposition, resulting in low ammonia concentrations. *Zhu et al.* [2015] incorporate the bidirectional flux scheme of *Pleim et al.* [2013] into GEOS-Chem, which increases the July ammonia emissions and concentration in the US. This slightly reduces the July model bias compared to measurements at Ammonia Monitoring Network (AMoN) sites. However, the bidirectional scheme causes a decrease in ammonia emissions and concentration in April and October, which worsens the comparison with observations and does not account for missing primary emissions. Such bidirectional flux schemes, developed largely to simulate field conditions, require higher resolution observations for evaluation at finer scales than those offered by current observations and global models.

3.2.3. GEOS-Chem Simulation of Ammonia in Previous Studies

A number of previous studies have evaluated the GEOS-Chem simulation of ammonia. These studies are often limited in their comparison with ammonia observations and instead use measurements of $PM_{2.5}$ concentration and wet deposition flux, which are more commonly measured, to indirectly evaluate the model. The initial evaluation of the implementation of the gas-particle partitioning mechanism by *Pye et al.* [2009] reveals an underprediction of inorganic

aerosol in the US, but they do not attribute this bias to problems with the ammonia emissions inventory. *Zhang et al.* [2012] apply an updated monthly scaling to the NEI-2005 ammonia emissions to improve the model bias in NH_x (NH_3 + ammonium (NH_4^+) based on network measurements of wet deposition fluxes over a limited timeframe. Even with these improvements, the model remains biased high for nitric acid, ammonium, and nitrate (NO_3^-), which they suggest is due to excess production of nitric acid from N_2O_5 hydrolysis, though *Heald et al.* [2012] show that altering this uptake process does not improve the simulation of nitrate in the model. An underestimate of ammonia emissions in California is suggested by *Heald et al.* [2012] and in Chapter 2 using Infrared Atmospheric Sounding Interferometer (IASI) satellite measurements and aircraft measurements of ammonia, respectively. *Walker et al.* [2012] also suggest that an increase in ammonia emissions in California is required to reduce the model bias compared to ammonium nitrate observations. The GEOS-Chem adjoint is used along with Tropospheric Emission Spectrometer (TES) measurements by *Zhu et al.* [2013] to constrain ammonia emissions over the US. They find an optimized solution that increases ammonia emissions in California and other parts of the western US and improves comparison of simulated surface concentration with observations from AMoN. *Paulot et al.* [2014] also use the GEOS-Chem adjoint along with ammonium wet deposition measurements to similarly optimize ammonia emissions. These results increase ammonia emissions in California and the Midwest, consistent with underestimates described in previous studies, and decrease emissions in some regions of the northeast and southeast. Their optimization also suggests errors in the seasonality of emissions, particularly relating to fertilizer emissions in the Midwest.

3.3. Ammonia Observations

3.3.1. IASI Satellite Column Measurements

Recent work has shown that atmospheric ammonia concentration can be retrieved from satellite observations at thermal infrared wavelengths [*Clarisse et al.*, 2009, 2010; *Shephard et al.*, 2011; *Shephard and Cady-Pereira*, 2015; *Warner et al.*, 2016]. These retrievals provide greater spatial coverage of ammonia concentrations than current surface networks. Here we use a product from the IASI mission, which is designed to take full advantage of the hyperspectral character of the instrument [*Van Damme et al.*, 2014a]. An infrared radiance index, calculated from a wider spectral range than previous ammonia satellite products to increase sensitivity, is

converted to a total ammonia column value using look-up tables that depend on this index and the thermal contrast (temperature difference between the surface (skin) and the air above). These look-up tables are computed using the Atmosphit forward radiative transfer model. The observations provide high spatial resolution (circular 12 km footprint at nadir) and up to twice daily temporal resolution. Although there is vertical variation in the concentration sensitivity in the infrared retrieval, this information (e.g., an averaging kernel) is not available with this IASI product. However, an uncertainty estimate (retrieval error) is associated with each individual measurement. In general, relative uncertainties are smaller for larger column concentration and larger thermal contrasts. These errors range from more than 100% to less than 25% under good conditions. This IASI product was initially used to examine both regional and global ammonia concentration variation, highlighting the influence of biomass burning events on the global scale as well as the ability to capture smaller ammonia emission features [*Van Damme et al.*, 2014a]. In *Van Damme et al.* [2015b], seasonal patterns and interannual variability at subcontinental scale are identified and an IASI derived climatology of the month of maximum columns is used to attribute major source processes. Ammonia column measurements from the retrieval scheme were also evaluated in Europe against a regional air quality model by *Van Damme et al.* [2014b]. This comparison shows good agreement between observed and simulated ammonia column concentrations in both agricultural and remote regions, although average measured columns are higher than those simulated. When accounting for the lack of retrieval sensitivity during colder months, the observations capture the seasonality simulated in the agricultural regions. *Van Damme et al.* [2015a] attempt to validate the IASI product against in situ ammonia measurements, although this is challenging given the lack of highly spatially distributed measurements and the difference in measured quantities. The measured IASI columns tend to show less variability compared to surface measurements.

Our study uses data from the morning overpass (09:30 local solar time when crossing the Equator) of IASI onboard the MetOp-A satellite from 2008 to 2012. Each day is gridded by computing the mean column concentration (and other properties) weighted by relative error of the native retrievals within each GEOS-Chem horizontal grid box at the nested resolution (0.5° × 0.667°). The results of this gridding and averaging scheme are shown in Figure 3.2 as the mean

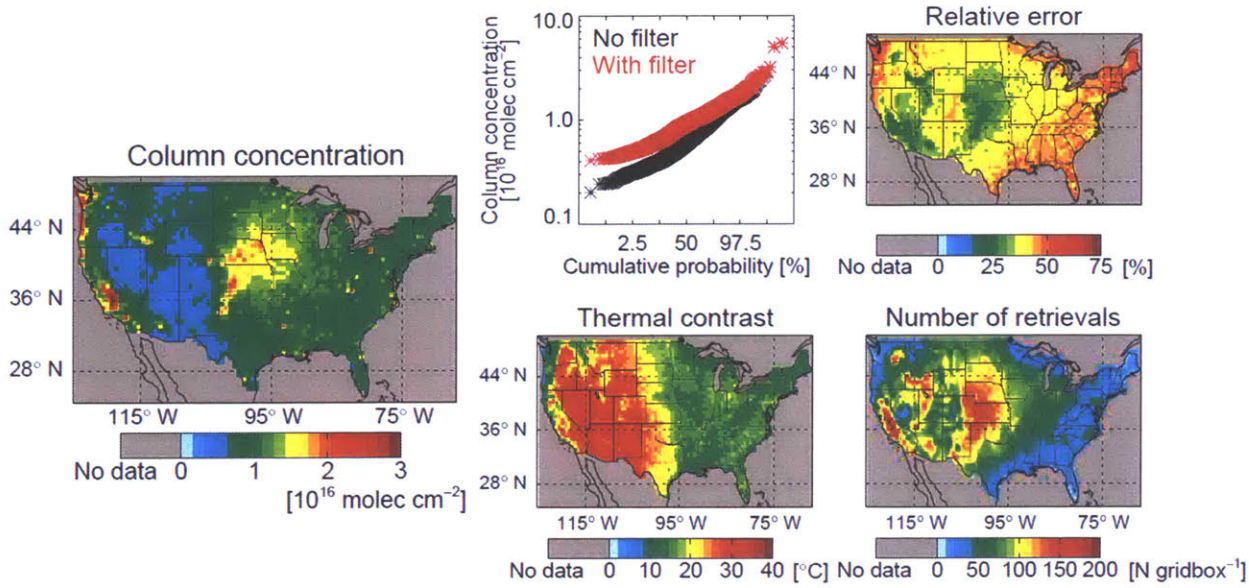

Figure 3.2. (left) Mean gridded daily summer (JJA) 2008–2012 IASI ammonia column concentrations, filtered for cloud cover (< 25% cloud cover), skin temperature (> –10°C), and relative error (≤ 75%). (top center) Distribution of column concentrations with (red) and without (black) described filtering. Accompanying retrieval parameters and properties: (top right) relative error, (bottom center) thermal contrast, and (bottom right) number of retrievals.

of all summers during the study period. We filter out retrievals with cloud cover greater than or equal to 25% and skin temperature less than or equal to –10°C as recommended by *Van Damme et al.* [2014a]. Post-gridded values are filtered by removing grid boxes with greater than 75% relative error. This filtering alters the distribution of the column concentration by removing the smallest values, as shown in Figure 3.2. We also isolate the continental US by removing grid boxes over Canada, Mexico and the ocean, but due to their size, some grid boxes along the border may exhibit outside influence (such as ocean retrievals along the Pacific Northwest coast). We calculate seasonal means as the simple arithmetic mean of all valid gridded daily values within that time period. This method weights each day with at least one valid retrieval evenly, rather than biasing the seasonal mean toward days with multiple valid retrievals in a grid box on a single day.

The gridded IASI values used in our analysis are more likely to be valid (meeting the retrieval and filtering restrictions) on warm, cloud-free days with high ammonia concentrations. The mean reported IASI concentrations are therefore biased, as low ammonia concentrations are harder to detect with confidence, and are thus often filtered out. Most valid retrievals occur during the summer, the time of highest concentration (and emissions in most areas) and better

infrared retrieval conditions. As shown in Figure 3.2, the range of mean (2008–2012) summer gridded and filtered concentrations is from 0.4 to 7×10^{16} molec cm^{-2}. The IASI column concentrations are highest in known agricultural regions such as the Central Valley of California, the Plains, and the Midwest. Individual spatial features are well defined and benefit from the high horizontal resolution satellite product.

Although filtered to exclude a maximum relative error, the remaining errors remain higher along the eastern coast and throughout the southeastern US, which has lower ammonia concentrations and lower thermal contrast. The relative error is also inversely related to the number of valid retrievals present in each grid box for a certain timeframe. These parameters are shown for comparison in Figure 3.2. The hot, dry, and cloud-free conditions experienced in the western US in the summer are ideal conditions for infrared retrievals. The higher emissions and concentrations of ammonia during the summer months also yield more information and higher confidence during this time. Thus, we restrict much of our analysis and discussion to the summers of 2008–2012. The lack of an averaging kernel provided with the IASI product makes a traditional model–measurement comparison challenging. We therefore focus on the qualitative spatial and temporal constraints from IASI.

We do not use other satellite measurements of ammonia, available from TES aboard the Aura satellite, the Cross-track Infrared Sounder (CrIS) aboard the Suomi National Polar-orbiting Partnership (NPP) satellite, and the Atmospheric InfraRed Sounder (AIRS) aboard the Aqua satellite [*Shephard et al.*, 2011; *Shephard and Cady-Pereira*, 2015;*Warner et al.*, 2016]. While the footprint of TES (~8 km) is smaller than that of IASI (~12 km), IASI has substantially better spatial coverage given TES's limited cross-track scanning. Thus, the measurement frequency over the same area is much higher for IASI and more useful for studying ammonia variability. The CrIS and AIRS products have only recently been developed. Further, CrIS has been active since only 2011, providing a limited timeframe for studying the variability of ammonia, and AIRS focuses on ammonia concentrations at a vertical height of 918 hPa, the location of highest instrument sensitivity, which excludes much of the western US, which is located above this height, from analysis.

3.3.2. AMoN Surface Measurements

AMoN (http://nadp.sws.uiuc.edu/amon/) reports integrated 2-week measurements of ammonia surface concentration at fixed ground sites across the US. While 14 days is the goal measurement frequency, this can vary by up to a week in either direction. AMoN was established in 2007, and we use measurements from 2008 through 2012 in our study. The number of sites and spatial coverage of the network has increased greatly throughout this timeframe (Figure 3.3). Fourteen sites provide measurements for the entire study period, with 57 sites operating by 2012. Measurements are made using triplicate passive diffusion samplers, where ammonia sorbs to a phosphoric acid-coated surface. The resulting ammonium is removed via sonication and measured with flow injection analysis [*Puchalski et al.*, 2011]. The passive sampler measurements used by AMoN have a 2σ uncertainty of 6.5% (www.radiello.com). Evaluation of these samplers against annular denuder measurements shows a consistent low bias, especially when measuring concentrations below 0.75 $\mu g\ m^{-3}$ (at 20°C and 1 atm, which is 0.99 ppb at standard temperature and pressure – STP) [*Puchalski et al.*, 2011]. However, we note that AMoN does not report blank corrections that could bias these measurements high [*Day et al.*, 2012]. AMoN measurements, reported in $\mu g\ m^{-3}$, are converted to ppb using local temperature and pressure from the GEOS-5 meteorology in this study. The summer seasonal mean surface ammonia concentrations measured by AMoN range from 0.43 ppb in Coweeta, North Carolina, to 31 ppb in Logan, Utah, during our study period. When calculating seasonal mean AMoN surface ammonia concentrations, we define the date of an individual AMoN measurement as the center date of its measurement time period. AMoN measurements from 27 sites from November 2007 to June 2010 have previously been used by *Zhu et al.* [2013] to evaluate the optimization of ammonia emissions used in GEOS-Chem. Their initial comparison prior to optimization showed that GEOS-Chem was generally biased low for surface ammonia concentrations throughout the year, with particularly poor performance in the spring.

3.3.3. Airborne Measurements

High resolution measurements of ammonia have recently been made in three dimensions aboard aircraft during field campaigns throughout the US. We use data from seven campaigns, which we separate into seven regions, for a total of nine snapshots of the vertical distribution of ammonia concentration. Specific information regarding these cases, including locations, dates,

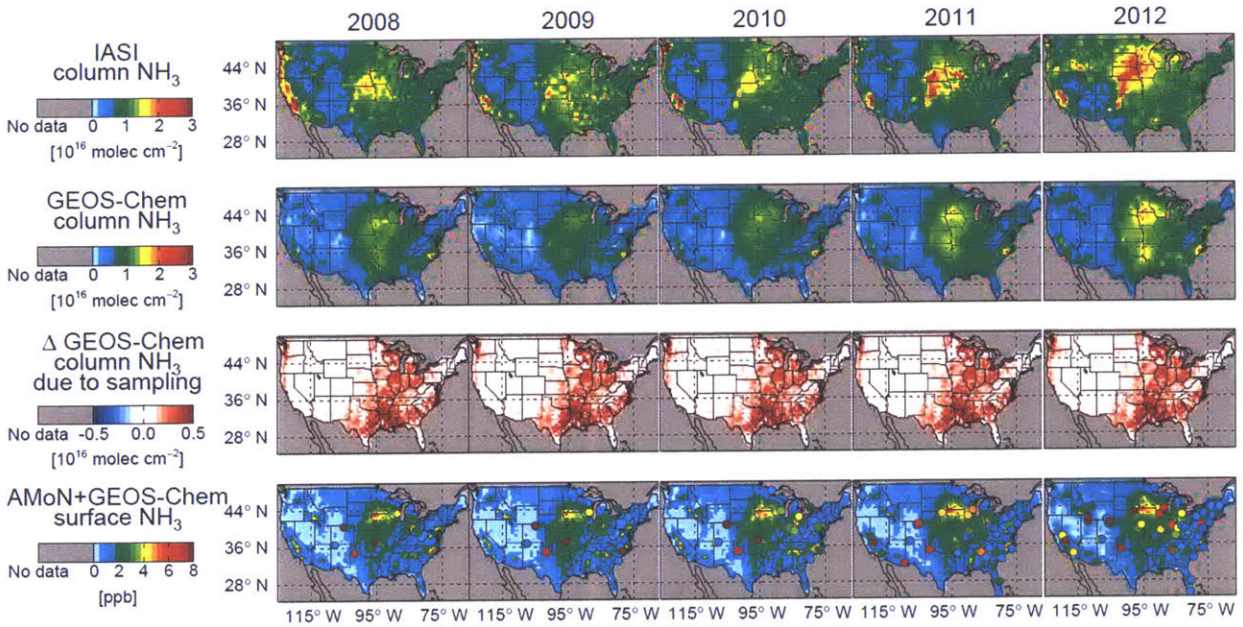

Figure 3.3. Mean summer (JJA) ammonia concentrations for (columns) 2008 to 2012: (rows, top to bottom) gridded and filtered IASI observed column concentration, GEOS-Chem simulated column concentration sampled to valid IASI days, changes in GEOS-Chem simulated column concentration due to sampling to coincident IASI measurements, and AMoN observed surface concentration (circles) overlaid on GEOS-Chem surface concentration.

instrumentation, and uncertainty, is listed in Table 3.1. All measurements were made with a 1 s interval, except those made during DISCOVER-AQ in California, which used a 3 s interval, and those made during ICARTT in the northeastern US, which used a 5 s interval. In all cases, the ammonia concentration measurements are averaged to 1 min time resolution. The horizontal spatial distributions of these measurements are shown in Figure 3.4a.

3.3.4. Observed Year-to-Year Ammonia Variability

The observed ammonia concentration can be modulated by numerous anthropogenic and environmental factors, including ammonia emissions, meteorology, and the emission of acid precursors (i.e., SO_x and NO_x). Emissions of anthropogenic ammonia are affected by changes in agricultural activities such as livestock population and fertilizer application, as well as the implementation of catalytic converters in urban areas. These emissions are sensitive to meteorology that modulates volatilization from the agricultural ammonia sources, increasing with higher temperature and wind speed. Biomass burning events are highly variable and temporarily increase ammonia emissions. Our baseline simulation captures only the year-to-year variation in biomass burning emissions of ammonia; emissions from all other sectors are fixed.

Table 3.1. Relevant details for the observed ammonia concentrations shown in Figure 3.4, including the aircraft campaign, geographic location, dates, ammonia instrument, instrument sample rate, and typical instrument uncertainty range (calibration uncertainty + measurement imprecision), which show flight-to-flight variability detailed in the respective archived data files.

Campaign	Region (lat.; lon. range)	Dates	Instrument	Uncertainty
ICARTT [*Nowak et al.*, 2007]	Northeastern US (38–47°N; 67–83°W)	Jul–Aug 2004	NH_3 CIMS[a]	±(30% + 0.115 ppb) + 0.045 ppb
TexAQS [*Nowak et al.*, 2010]	Eastern Texas (27–35°N; 90–100°W)	Sep–Oct 2006	NH_3 CIMS	±(25% + 0.070 ppb) + 0.035 ppb
CalNex [*Nowak et al.*, 2012]	Southern California (CA) (see Chapter 2)	May–Jun 2010	NH_3 CIMS	±(30% + 0.200 ppb) + 0.080 ppb
CalNex	Central Valley, CA (see Chapter 2)	May–Jun 2010	NH_3 CIMS	±(30% + 0.200 ppb) + 0.080 ppb
DISCOVER-AQ	Central Valley, CA (see Chapter 2)	Jan–Feb 2013	CRDS[b] (Picarro G2103)	±(35% + 1.7 ppb) + 0.2 ppb
SENEX	Southeastern US (31–43°N; 75–96°W)	Jun–Jul 2013	NH_3 CIMS	±(25% + 0.070 ppb) + 0.020 ppb
FRAPPE	Colorado (38–42°N; 101–110°W)	Jul–Aug 2014	Aerodyne Dual NH_3/HNO_3 QCL[c]	±(22% + 0.305 ppb) + 0.058 ppb
SONGNEX	Colorado (38–42°N; 101–110°W)	Mar–Apr 2015	NH_3 CIMS	±(35% + 0.500 ppb) + 0.035 ppb
SONGNEX	Southern Plains (26–36°N; 93–105°W)	Mar–Apr 2015	NH_3 CIMS	±(35% + 0.500 ppb) + 0.035 ppb

a CIMS: chemical ionization mass spectrometer. b CRDS: cavity ring down spectrometer. c QCL: quantum cascade laser.

Meteorology affects the partitioning of ammonia into ammonium nitrate, where higher temperature and lower relative humidity favor the gas phase, as well as the removal of ammonia from the atmosphere by changing the rates of both wet and dry deposition [*Russell et al.*, 1983; *Mozurkewich*, 1993]. Even in a well-mixed boundary layer, ammonia concentrations may have strong gradients caused by temperature variations with altitude that alter gas-to-particle partitioning of ammonium [*Neuman et al.*, 2003]. Figure 3.5 shows the year-to-year variation in key meteorological parameters across the US from 2008 to 2012 from the GEOS-5 assimilated meteorological product. Emissions of SO_x and NO_x also affect the ammonia concentration by regulating the amount of acid available to convert ammonia into ammonium sulfate and ammonium nitrate particles. Figure 3.1 shows that the anthropogenic component of these emissions decreases substantially in the US during our study period. Meteorology can also affect the rate of soil and fertilizer NO_x emissions by changing the storage and volatilization processes (simulated changes also shown in Figure 3.5).

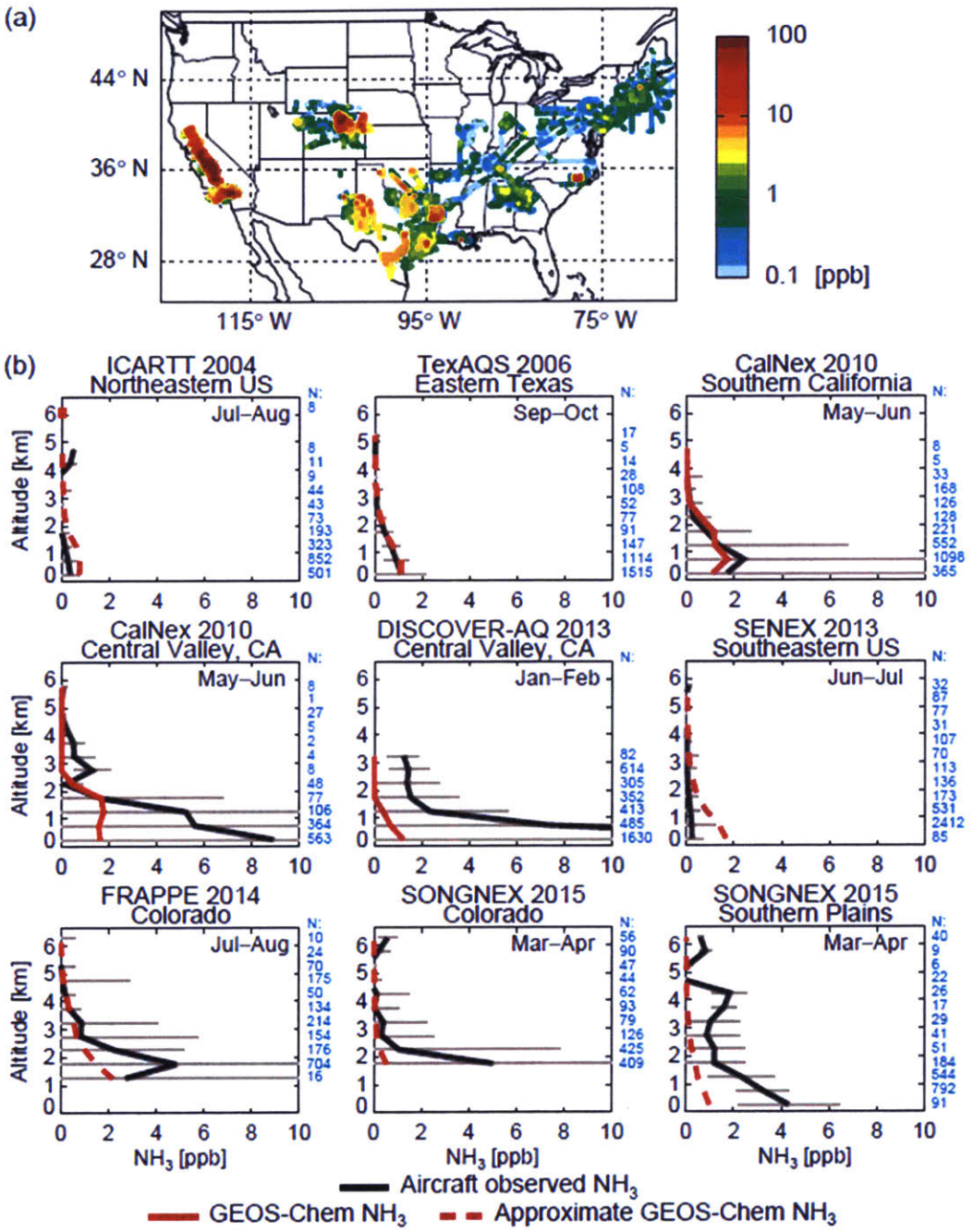

Figure 3.4. (a) Spatial distribution of 1 min mean observed ammonia concentrations for several aircraft campaigns throughout the US listed in Table 3.1. (b) Vertical profiles of median observed ammonia concentration (black) and median GEOS-Chem simulated ammonia concentration (red) averaged in 500 m vertical bins from these campaigns. Simulated concentrations matched to the year and flight tracks of the campaign are shown in solid red, while approximately sampled concentrations (mean 2008–2012 simulated concentrations) are shown in dashed red. Gray bars show the standard deviation of observations in each bin. The number of observations in each bin are shown in blue. The 2 months during which the campaign took place are indicated in the top right of each profile.

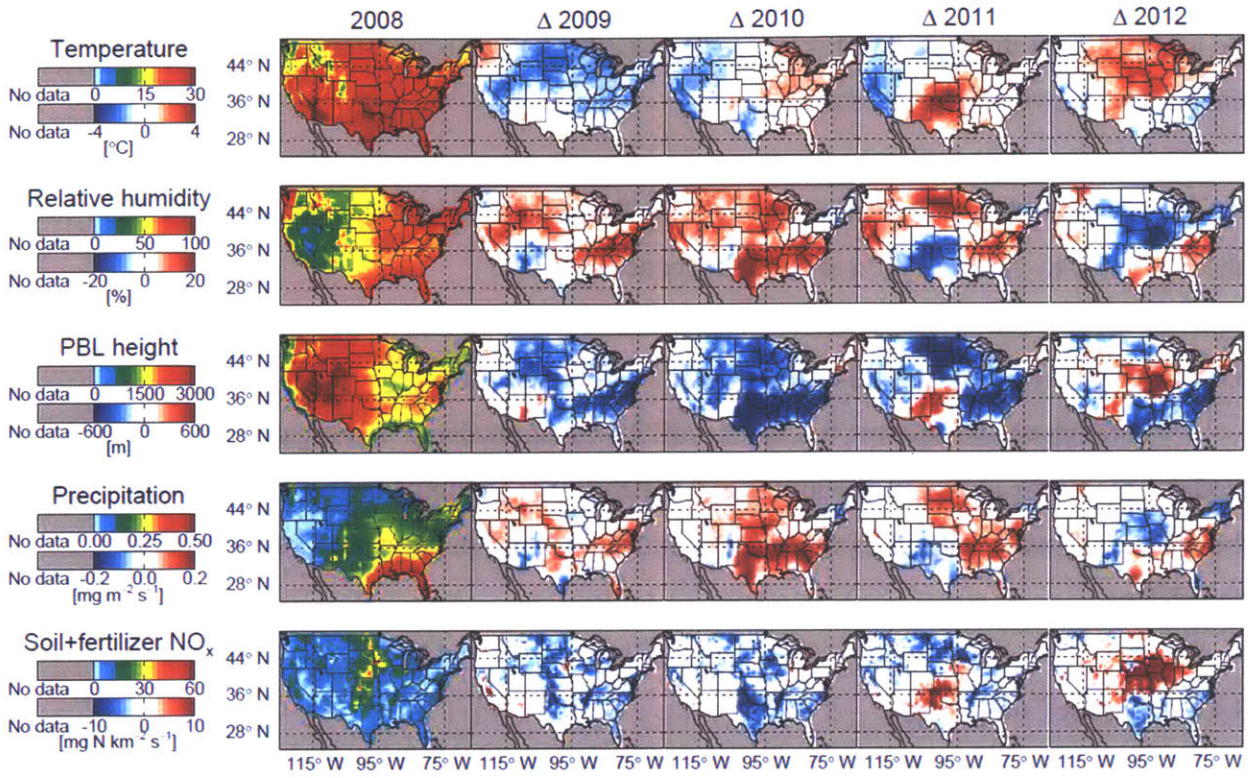

Figure 3.5. Mean summer (JJA) assimilated GEOS-5 meteorology parameters and meteorologically driven NO_x emissions used in GEOS-Chem simulation for (columns) 2008 to 2012: (rows, top to bottom) temperature, relative humidity, planetary boundary layer (PBL) height, precipitation, and soil+fertilizer NO_x emissions. Absolute values for 2008 shown along with changes from 2008 for 2009 to 2012.

Using IASI column concentration and AMoN surface concentration measurements, we show in Figure 3.3 that observed ammonia concentrations vary significantly from year to year over the US. The mean IASI column concentration observed over the US in the summers of 2008 through 2012 is 0.95×10^{16} molec cm^{-2}, which ranges from a low of 0.90×10^{16} molec cm^{-2} in 2010 to a high of 1.1×10^{16} molec cm^{-2} in 2012 (indicating that the mean ammonia column concentrations over the US range from –5.3 to +16% of the mean during these 5 years). At the surface, the mean AMoN observed ammonia concentration in the summer from all sites with records from 2008 to 2012 is 3.4 ppb, ranging from 3.0 ppb in 2009 to 4.3 ppb in 2012 (or between –11 and +25% of the mean). The IASI and AMoN observations differ on the year with the lowest mean summer concentration (2010 for IASI and 2009 for AMoN); this difference is likely due to a lack of AMoN sites distributed throughout areas that have low IASI column concentrations in 2010. The regions of high agricultural production, including California and the Plains, exhibit higher year-to-year variability in the magnitude of IASI column concentrations. For example, in the Plains region, maximum summer IASI values are 23% higher in 2012 than

the mean of the 5 study years. This is also the case for surface concentrations at several AMoN sites in the Midwest and the west.

In what follows, we will use the GEOS-Chem model to examine the source of the observed year-to-year variation in ammonia concentrations.

3.4. Base Scenario Simulation of Ammonia Measurements

Throughout this section, we use the GEOS-Chem model to investigate how well the model captures the observed magnitude and variability in ammonia concentrations. We sample the model to simulate the ammonia concentrations observed in both temporal and spatial dimensions.

3.4.1. Column Comparison

To evaluate the ammonia concentration throughout the column, the simulated column concentrations are recorded at the local 09:00–10:00 overpass time, and this 1 h mean is compared to the IASI retrievals at 09:30 local time. It is not straightforward to compare this value in an unbiased way with the IASI measurements since the vertical sensitivity of the instrument may not be consistent with the model. For this reason, this value cannot be quantitatively compared to the IASI retrieved column with confidence; however, we qualitatively compare trends and spatial features here. When sampling is applied, only simulated days with valid IASI retrievals (at least one per grid box) are included. Seasonal means are calculated as the mean of all days (no sampling) or of only days with valid IASI retrievals (with sampling). The simulated ammonia column concentrations are generally well correlated with the IASI observations (Figure 3.6) over the summer, particularly in the Plains and the Midwest (correlation (R) = 0.6–0.8). Sampled simulated column concentrations shown in Figure 3.3 have a summer mean of 0.64×10^{16} molec cm^{-2}, ranging from 0.52×10^{16} molec cm^{-2} in 2009 to 0.80×10^{16} molec cm^{-2} in 2012 (or between –19 and +25% of the mean). We find considerable year-to-year variation in the simulated ammonia concentration, even with fixed ammonia emissions.

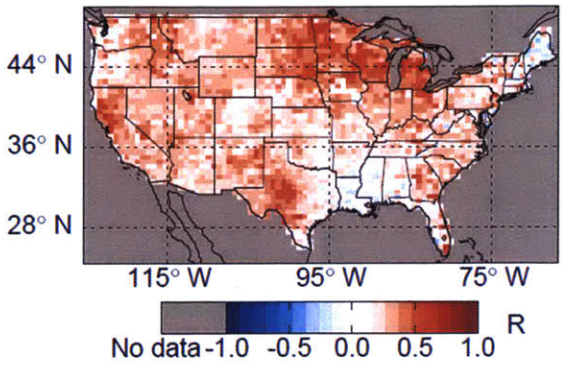

Figure 3.6. Summer (JJA) correlation (R) for all years (2008–2012) between daily gridded and filtered IASI ammonia column concentration and daily GEOS-Chem base scenario ammonia column concentration.

Sampling the model to match IASI observations, as shown in Figure 3.3, increases the concentrations in regions with more invalid IASI days according to the filtering process described in Section 3.3.1. Valid days tend to have higher concentrations as they meet the filter requirements due to more favorable retrieval conditions, which include a higher retrieved ammonia signal. Cloudy days, being cooler and having greater probability of rain, also tend to have lower ammonia concentrations, and these cannot be retrieved. In the southeastern US, sampling increases the regional summer mean simulated ammonia column concentration significantly, by 26% (2011) to 58% (2012). Even after accounting for this sampling bias, the simulated column concentrations are consistently lower than those observed by IASI, which is consistent with the findings of *Van Damme et al.* [2014b] over Europe. This underestimate is because the filter requirement restricting high relative error inherently favors larger observed columns. Consequently, there is lower year-to-year variability in the mean summer IASI column concentrations (21% of the mean between the highest and lowest years) than those simulated by the model (44%). This discrepancy in variability may also be due to our use of total column values, rather than isolating the layers where the satellite has greater sensitivity. For example, removing the more variable near-surface layers, where the satellite is presumed to be less sensitive, could reduce the model variability in the comparison mentioned above.

The distribution of ammonia throughout the column is also relevant to assessing the ability of the model to represent the ammonia column concentration observed by IASI, as the retrieval has varying sensitivity at different vertical levels. In Figure 3.4b we use measurements of ammonia from several aircraft campaigns throughout the US to evaluate the simulated

ammonia vertical profile. We show the median, rather than the mean, to account for the inherent inability of the model to reproduce highly concentrated plumes occasionally observed by the aircraft. To compare the observations with the simulation during campaigns that take place in our study period (extended to February 2013), we sample the model directly in time and space for each flight of the campaign. For campaigns outside of this time period, we sample directly in space for each flight but approximate the time component by using the 5-year mean (2008–2012) of each 2-month campaign window. As shown in Figure 3.4b, the observed median ammonia vertical profile is highly variable in magnitude and shape between different regions. In high ammonia emission regions, the observed ammonia concentration increases greatly toward the surface, and the median ammonia vertical profile is less variable between different campaigns in the same region (e.g., Central Valley in 2010 and 2013, Colorado in 2014 and 2015) than between different regions. As with the observations, the model performance varies greatly between regions. Over areas such as Central Valley, previously examined in Chapter 2, the model underestimates ammonia throughout the vertical profile, especially near the surface. The model also performs more poorly in the spring according to measurements in Colorado and the southern Plains in 2015, but limited sampling across seasons makes it difficult to be conclusive. Other regions, like southern California, eastern Texas, Colorado in summer 2014, and the southeastern US have a much smaller bias. The slight high bias in the model at the surface in the northeastern and southeastern US regions is consistent with previous evaluation of NEI-2005 in GEOS-Chem against AMoN measurements [*Paulot et al.*, 2014]. Local conditions clearly influence the model simulation of the observed concentrations. Overall, the model shows less variability than the observations, but the model profile shape is generally consistent with the observed shape outside of large source regions. This suggests that, outside of these source regions, model biases in the shape of the vertical profile are unlikely to bias comparisons with satellite column observations.

3.4.2. Surface Comparison

Summer seasonal mean simulated surface concentrations are compared with the seasonal mean AMoN surface concentration observations in Figure 3.3. For a more direct comparison of individual observations, we match the hours of the AMoN sampling period with the corresponding hourly values from the simulation, and the mean of these hours is used for

comparison. We also apply a spatial interpolation scheme to this comparison, where the four nearest grid box values are averaged based on the distance between their center and the observation site location. This adjusts the simulated concentration to account for the influence of nearby grid boxes at sites near grid box edges and in regions that exhibit strong horizontal gradients. The mean summer simulated surface concentration at AMoN sites with measurements from 2008 to 2012 (11 sites) is 2.5 ppb, which varies from a low of 2.1 ppb in 2008 (–16% of the mean) to a high of 2.8 ppb in 2012 (+13% of the mean) over the study time period. This mean simulated concentration is lower than that observed (2.5 ppb vs. 3.4 ppb). The range of simulated surface concentrations between high and low years is also half of the range observed (0.73 ppb vs. 1.3 ppb). These ranges are shown for comparison in Figure 3.7 along with the range in surface ammonia concentrations over the entire US. The range in summertime mean ammonia concentrations across the US is smaller, and the mean is lower (by more than 25%) than when sampled to the AMoN sites. This suggests that the AMoN network does not adequately represent the range of ammonia concentrations across the US; as many AMoN sites are located near high ammonia source regions, there is a sampling bias for this network. The near-source location of many of these AMoN sites provides an additional challenge for the regional-scale resolution model simulation used here and is likely responsible for some of the model underestimate.

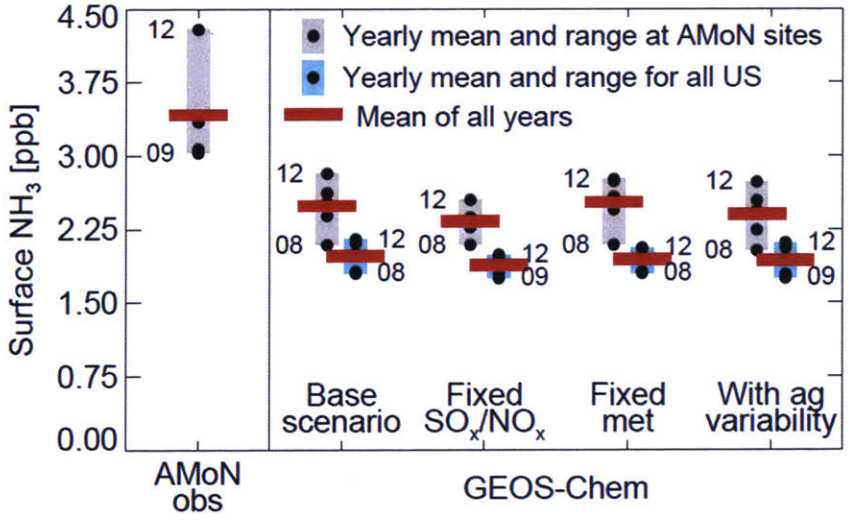

Figure 3.7. Yearly summer (JJA) mean surface ammonia concentration (black circles) and mean of all years (red bar) for observed AMoN sites valid from 2008 to 2012 and four GEOS-Chem scenarios: (left to right) base scenario, fixed anthropogenic SO_x and NO_x emissions, fixed meteorology, and including agricultural ammonia emission variability. Vertical bars indicate the range of all years: simulation sampled to AMoN sites (gray) and simulation for the entire US (blue).

By limiting the above analysis to only summers 2011 and 2012, the number of sites with measurements in both years increases to 48. The mean bias in this case is more modest (–0.02 ppb), with 2011 biased slightly high and 2012 biased slightly low. There is a consistent high bias at many of the eastern US sites, which is offset by a low bias in the west in 2012, likely due to local biomass burning that is not adequately captured in the model. However, even for this limited time period, the model fails to reproduce the observed year-to-year variation (observed 0.80 ppb increase in the summertime mean from 2011 to 2012, with a simulated increase of only 0.11 ppb). This difference is dominated by high measurements in 2012 in the west, but the observed increase from 2011 to 2012 in the Midwest is also underestimated.

Figure 3.8 shows a detailed comparison of observed and base scenario simulated surface ammonia concentrations at three AMoN sites with records from 2008 to 2012; these are selected as representative regional sites and demonstrate the varying degree of model skill. Simulated concentrations at all three sites reproduce the observed seasonal cycle, with highest concentrations in the summer and lowest in the winter. The Indianapolis, Indiana, site represents typical Midwestern sites, with nearby urban SO_x and NO_x emission sources surrounded by rural ammonia sources. This site is located in central Indianapolis, and the corresponding model grid box is made up of about 30% city and 60% rural land. The overall comparison at Indianapolis is good throughout the study period, with an R of 0.56 and a normalized mean bias (NMB) of –0.14 (mean bias of –0.41 ppb). There is a noticeable increasing trend in the observed ammonia concentrations from 2008 to 2012; the model captures much of this upward trend.

The Horicon Marsh, Wisconsin, site represents rural regions where ammonia emissions are primarily from agricultural sources. This site is located in a grid box that is nearly 90% farm land (the remaining 10% is made up of small towns and wetlands). This uniformity should be easier for the model to represent. The comparison between observed and simulated ammonia concentration is generally very good when considering the entire time period (R = 0.65, NMB = 0.06, mean bias = +0.19 ppb). However, this comparison is somewhat worse in the summer (R = 0.44), as the model does not properly simulate the timing or magnitude of the peak concentrations.

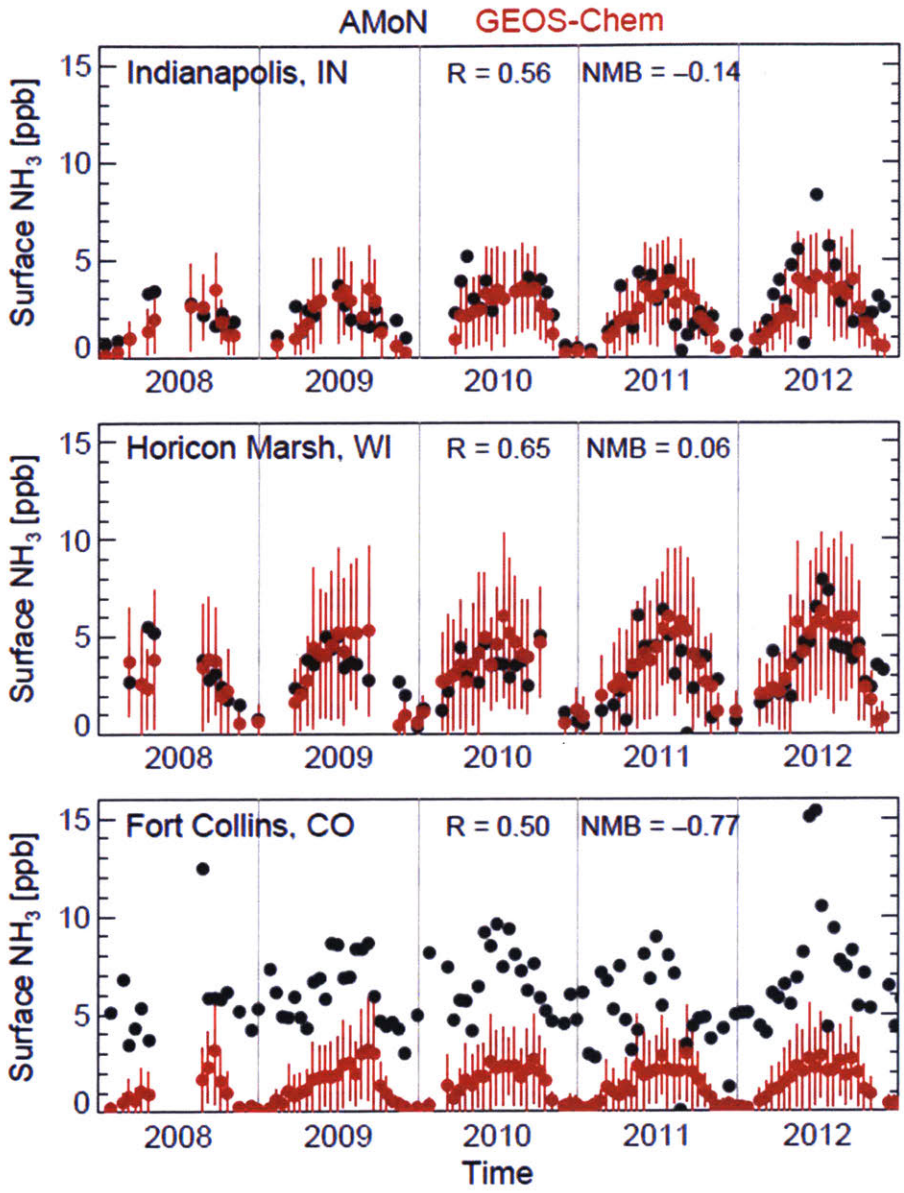

Figure 3.8. Observed (black circles) and base scenario simulated (red circles) surface ammonia concentration time series at three AMoN sites from 2008 to 2012: (top, urban) Indianapolis, Indiana (IN), (middle, agricultural) Horicon Marsh, Wisconsin (WI), and (bottom, varying topography/high horizontal gradient) Fort Collins, Colorado (CO). Standard deviation of simulated hours shown as vertical red lines. Gray vertical lines indicate the transition between calendar years.

Finally, the Fort Collins, Colorado, site represents one of several sites in the western US that present a challenge to simulate due to large horizontal concentration gradients over areas with highly varying topography. This is an area of high livestock ammonia emissions to the east bounded on the west by the Front Range of the Rocky Mountains. Ammonia is advected from feedlots to the east and observed high concentrations result. The site is located on the eastern side of a grid box that is made up of 75% mountains and forest toward the west. There is

considerable elevation increase as well from east to west. As a result, simulated concentrations in this grid box take on the characteristics of the mountain region rather than the agricultural plain. There is a large low bias at the Fort Collins site of –4.7 ppb (R = 0.50, NMB = –0.77) for the entire time period. If we compare the observations with simulated values of the next grid box east in the agricultural region (without weighting neighboring grid boxes), the bias drops significantly (about 35%), so that only –3.0 ppb bias in all months remains. However, even with this adjustment to account for site location, the model performance here is among the poorest. Similar comparisons for the eight remaining sites with records during this time period are shown in Figures S1–S3 in Supplement.

3.4.3. Integrated Comparison: Colorado, Summer 2012

The variation of both the observed column and surface ammonia concentrations in the western US is influenced by biomass burning events in the summer of 2012. The wildfire activity in the Colorado Front Range during this time (May–September 2012) provides an opportunity to synthesize the different ammonia concentration information discussed above as this is an area that is also known for high agricultural ammonia emissions.

IASI measurements during days without fire emission influence (determined by visual inspection of Moderate Resolution Imaging Spectroradiometer (MODIS) imagery, with at least 75% domain retrieval coverage) show a peak mean column concentration of 2.1×10^{16} molec cm^{-2} just to the east of Fort Collins (FC) (Figure 3.9), corresponding to the location of feedlots. The mountains to the west of FC, along with ridges to the north and south, cause the agriculturally emitted ammonia to circulate throughout the Front Range, with only limited transport westward [*Wilczak and Glendening*, 1988]. Column concentrations remain elevated to the south and east throughout the plain of eastern Colorado, while concentrations in western areas of the domain at high elevations are quite low. Aircraft measurements in Colorado during the FRAPPE (summer 2014) and SONGNEX (spring 2015) campaigns confirm this distribution of ammonia in the region (Figure 3.4a). Figure 3.9 shows that IASI column concentrations are considerably higher on days with wildfire activity. The largest increase takes place over the Front Range near FC and to the east due to fires located in the Colorado mountains during late June–early July, when the mean IASI column over the region more than doubles. In August,

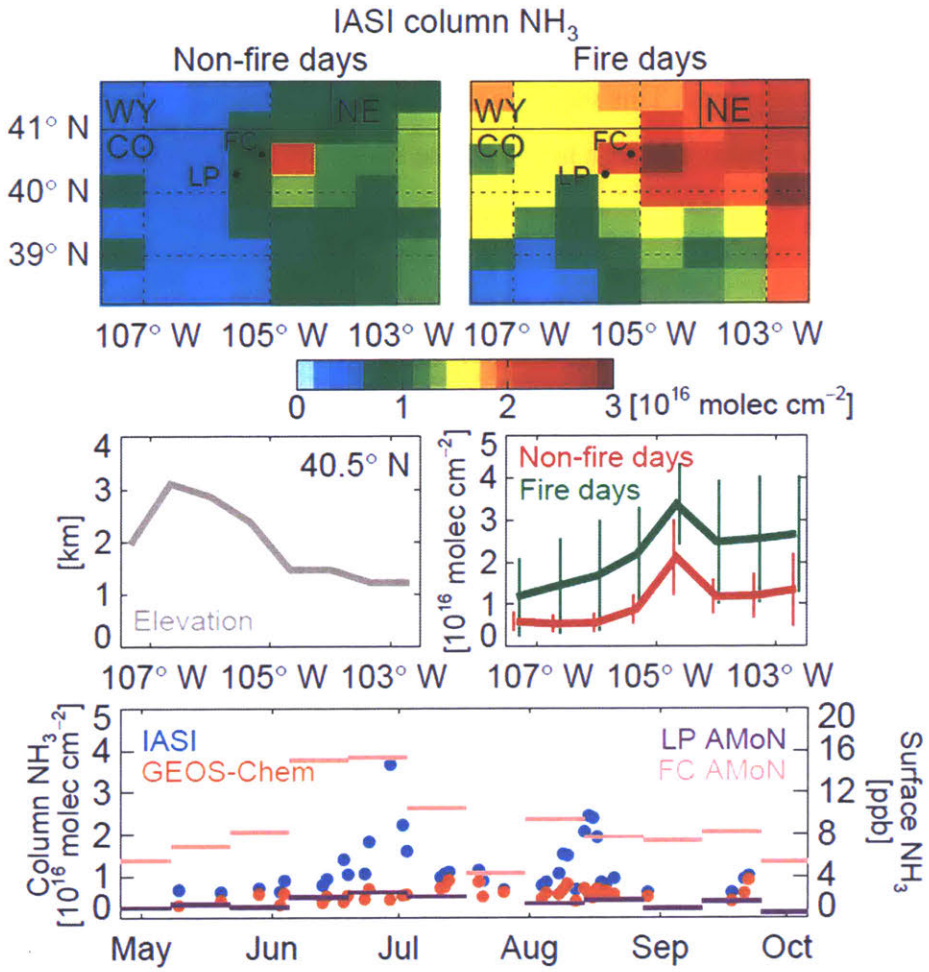

Figure 3.9. Mean gridded IASI column ammonia concentration over the Colorado Front Range from May to September 2012 during (top left) non-fire days and (top right) fire days. (middle left) Elevation of each grid box center at 40.5°N over the longitude range above. (middle right) Mean IASI column ammonia concentration at each gridbox at 40°5 N over the longitude and time range above for non-fire days (red) and fire days (green). (bottom) Mean daily IASI (blue) and GEOS-Chem (orange) column ammonia concentrations over the domain above and observed surface ammonia concentrations at the Longs Peak (LP) (purple) and Fort Collins (FC) (pink) AMoN sites.

column concentrations are enhanced in the north and west of the domain due to the transport of wildfire plumes into the region from fires in other areas of the northwestern US. Thus, we see in Figure 3.9 that the average ammonia concentrations observed by IASI during the season are elevated throughout the region due to fire emissions. These wildfire emissions are present in addition to the persistent agricultural ammonia sources throughout the time period, as the feedlot grid box east of FC has the highest column concentration even on wildfire-influenced days (3.4×10^{16} molec cm^{-2}, increase of 62 %). However, the IASI retrieval is more sensitive to ammonia lofted vertically, as is the case in biomass burning outflow. The GEOS-Chem

simulated ammonia column concentrations in this domain do not capture the peaks observed by IASI throughout the time period. This suggests that the model inventory underestimates the fire emissions of ammonia or their injection height; these biases are likely exacerbated by the IASI vertical sensitivity.

AMoN surface concentrations at the FC site, also in Figure 3.9, follow the peaks in concentration observed by IASI in both June and August and show a similar relative increase (factor of ~2 in late June), while surface concentrations at the Longs Peak (LP) AMoN site show no evidence of an enhancement due to fire, likely because the site is isolated from the Front Range source region. It is difficult to quantify the contribution of the wildfire ammonia source from these observations because the fire events also correspond to the highest surface temperatures of the year, thereby affecting ammonia volatilization and partitioning chemistry. Additional observations of ammonia concentrations in fire plumes could help improve emissions estimates and clarify the importance of this source (e.g., *Whitburn et al.* [2015]).

3.4.4. Updated Inventory Comparison

A more recent anthropogenic emission inventory, NEI-2011, is available over the US for 2011 (available from www.epa.gov/air-emissions-inventories/2011-national-emissions-inventory-nei-data, adapted for GEOS-Chem by *Travis et al.* [2016]). This inventory includes changes in both the magnitude and timing of anthropogenic ammonia, SO_x , and NO_x when compared to NEI-2005. Averaged over the summers during the study period of 2008 to 2012, anthropogenic ammonia emissions are 26% higher, anthropogenic SOx emissions are 13% higher, and anthropogenic NOx emissions are 11% lower in NEI-2011 compared to in NEI-2005 as applied to GEOS-Chem over the US. Variable spatial seasonality for ammonia emissions has been included in NEI-2011 such that known emissions events like springtime fertilizer application in the Midwest are now accounted for.

We repeat our GEOS-Chem simulations with NEI-2011 for 2008 and 2012 and compare the simulated surface concentrations with the observed AMoN surface concentration in these 2 years. Generally, the summer high concentration bias at the eastern US sites is reduced using the updated inventory. The simulation improves at a few of the western sites as well, but many

biases remain or worsen. Strong gradients in local sources and geography still likely play a large role at many of these sites. At Midwestern sites, the new seasonality often better represents the springtime and summer peak concentration, but the comparison during the transition to late summer and fall is degraded. For Horicon Marsh, Wisconsin, the summer R in 2008 and 2012 between observed and simulated surface concentrations decreases from 0.63 to 0.48 when using NEI-2011 rather than NEI-2005. While NEI-2011 may better represent the magnitude and timing of emissions in some locations, it is also a year-specific inventory and does not provide a better constraint than NEI-2005 on the year-to-year variations in ammonia emissions that are the main focus of this study.

3.4.5 Summary of Base Scenario to Observation Comparisons

From the comparisons described here, we conclude that the model generally captures the vertical, temporal, and regional variability of ammonia but underestimates the summertime ammonia concentration observed in both the column and at the surface, particularly near source regions (including both agricultural and fire emissions). The year-to-year variability in the model at the surface is lower than the variability observed, but the trends and variability captured by the simulation are significant considering that ammonia emissions in the model are fixed. We next explore the processes in the model that contribute to this variability.

3.5. Attributing Sources of Ammonia Variability

3.5.1 SO_x and NO_x emissions reductions

In order to identify the drivers of year-to-year variation in simulated ammonia concentrations, we run sensitivity studies that isolate individual factors affecting the ammonia concentrations. The first sensitivity simulation holds anthropogenic SO_x and NO_x emissions constant at 2008 levels for 2009 to 2012 in order to gauge the effects of these emissions reductions on the ammonia concentration in the base scenario. This analysis relies on an accurate simulation of the trends in sulfate and nitrate in areas of significant ammonia concentration. Briefly, we evaluate our base scenario against observations from all available sites (148) in the Interagency Monitoring of Protected Visual Environment (IMPROVE) network (vista.cira.colostate.edu/improve) over our study period. Comparison of the trend in summer mean indicates that GEOS-Chem reproduces well the decreasing trend in sulfate over the eastern

US and the Pacific coast (not shown). In the Intermountain West, which generally lacks high ammonia concentrations, the simulation predicts a decreasing trend in sulfate, while the observations show an increase. The model generally reproduces the trend in nitrate, although the decline in nitrate in the eastern US is somewhat stronger than observed. This indicates a possible oversensitivity to changing NO_x emissions in the model.

Figure 3.10 shows that SO_x and NO_x reductions over the US act to significantly increase the ammonia column concentration over time. Much of this increase takes place over the eastern US, where anthropogenic SO_x and NO_x emissions are highest (Figure 3.1), and therefore where absolute reductions in SO_x and NO_x are largest. Decreases in the sulfate and total nitrate ($TNO_3 = HNO_3 + NO_3^-$) availability caused by the SOx and NOx emission reductions, respectively, require less ammonium to neutralize particle-phase acids, leaving more ammonia in the gas phase. For the US summer mean, the simulated ammonia surface concentrations increase by 8.8% from 2008 to 2012 due to the anthropogenic emissions changes, compared to the 29% decrease in total SO_x emissions and the 17% decrease in total NO_x emissions. We attribute 32% (0.17 ppb) of the range of summer surface ammonia concentration simulated by the base scenario to anthropogenic SO_x and NO_x emissions reductions. In the column, 26% (0.07×10^{16} molec cm^{-2}) of the range is due to these reductions.

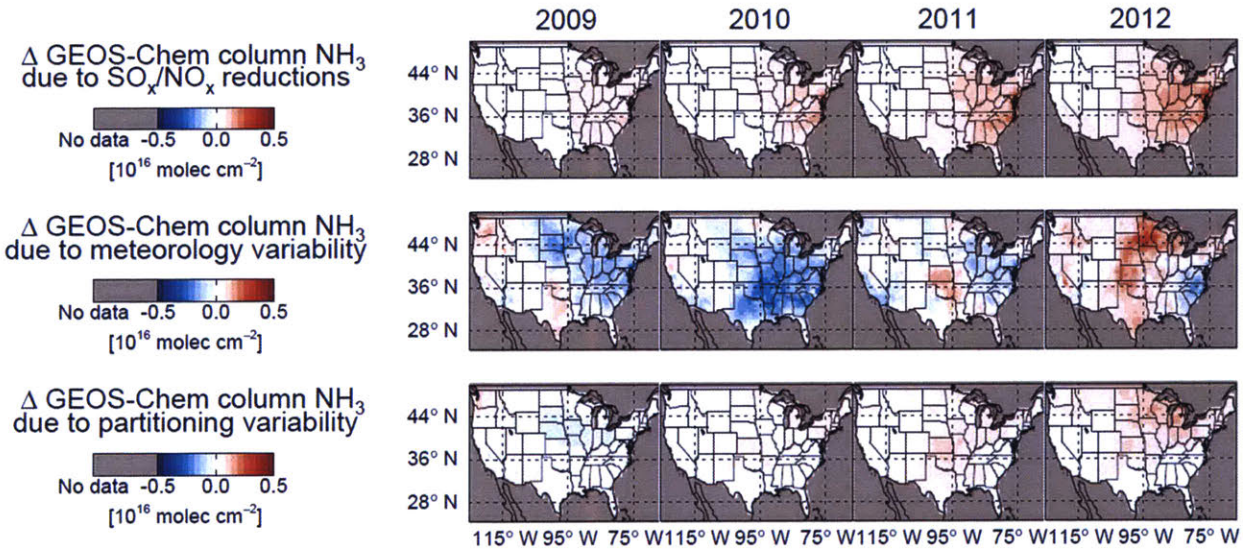

Figure 3.10. Simulated mean summer (JJA) ammonia column concentration changes for (columns) 2009 to 2012 caused by (rows, top to bottom) anthropogenic SO_x and NO_x emissions reductions, assimilated meteorology variability, and meteorology variability affecting only ammonium nitrate partitioning. Compare to the baseline ammonia column shown in Figure 3.3.

3.5.2. Meteorology Variability

The second sensitivity simulation tests the effects that meteorological variability has on the simulated ammonia concentration. In this simulation, we hold the GEOS-5 assimilated meteorology constant at year 2008 conditions for all years of our simulation (2008–2012). Meteorology can alter the distribution and phase of ammonia via changes in transport, deposition, oxidation, and gas-particle partitioning. Soil and fertilizer NO_x emissions are also effectively held constant in this simulation given that their variability is largely controlled by meteorology. While meteorology may indirectly affect biomass burning emissions, such as by leading to more fires during a dry and hot year, we do not account for this here, as these emissions are allowed to vary in all cases. Comparison with both 10- and 35-year mean Modern-era Retrospective Analysis for Research and Applications (MERRA) meteorology from the NASA GMAO [*Rienecker et al.*, 2011] shows that 2008 is a typical meteorological year in the US. Thus, anomalies from 2008 in 2009–2012 can be seen as realistic deviations from an average condition.

Figure 3.10 shows that the effects of meteorology on the ammonia concentration are highly variable both spatially and temporally. The spatial variability is generally greater at the surface (not shown) than in the column. Variations in simulated ammonia concentration can be connected with the meteorological features shown in Figure 3.5. For example, the summer of 2010 in the southeastern US is a high precipitation year that contributed to lower ammonia concentration throughout the column due to increased wet removal. Higher relative humidity also likely contributes to this decrease by favoring the particle phase of the ammonium nitrate equilibrium. Another example is the high-temperature, low-humidity and low-precipitation summer of 2012 in the Plains and the Midwest, which favors the gas phase of the ammonium nitrate equilibrium and generally higher concentrations (due to reduced removal). However, these same high temperatures in 2012 lead to higher emissions of soil and fertilizer NO_x, which modestly counteract this effect at the surface by encouraging more ammonia to partition to the particle phase to neutralize this supply of acid (Figure 3.5). Lower planetary boundary layer (PBL) heights, such as in the upper Midwest in summer 2011, can trap ammonia near the surface. More ammonia nearer the surface could increase the dry deposition flux as this is the primary direct removal method for gaseous ammonia, slightly offsetting the increased

concentration due to trapping and decreasing the concentration throughout the column. We attribute 64% (0.34 ppb) of the range of summer surface ammonia concentration simulated by the base scenario to meteorology. In the column, 67% (0.18×10^{16} molec cm^{-2}) of the range is due to these variations. Meteorology clearly dominates the year-to-year variability in simulated ammonia concentration.

A third sensitivity simulation isolates the effects of two-way partitioning of ammonia on the simulated ammonia concentration. This partitioning is driven by the ambient temperature and relative humidity as inputs into ISOROPPIA II. In this simulation, we hold these inputs constant at year 2008 conditions for all years of our simulation (2008–2012). Higher temperature and lower relative humidity generally favor partitioning into the gas phase and an increase in ammonia concentration. The results of this simulation, shown in Figure 3.10, indicate that the effects of partitioning are less spatially and temporally variable than those of all meteorology discussed above. The variability due to partitioning can make up a significant portion of the change due to all meteorology, such as in the warm summer of 2012 when partitioning accounts for 73% of the net change due to all meteorology. This is also true to a smaller degree during the cool summer of 2009 (13%). In relatively wet summers, such as 2010 and 2011, enhanced partitioning acts to offset the losses due to all meteorology (likely caused by increased wet deposition) by 10 and 73%, respectively. Overall, partitioning accounts for 23% (0.06×10^{16} molec cm^{-2}) of the range in the summer base scenario column concentrations, which is 33% of the range due to all meteorology. Thus, the phase partitioning due to meteorology plays a significant, but not always dominant, role in controlling the variability of ammonia.

3.5.3. Missing Simulated Ammonia Variability

The simulated ammonia concentrations do show significant year-to-year variability despite constant ammonia emissions, but this variability is generally lower than that observed by IASI and AMoN at individual locations (Figures 3.3 and 3.7). However, maximum observed column concentrations in the western US in 2012 are likely from smoke enhancements at the vertical levels at which IASI is more sensitive; the model cannot reproduce this column variability without properly weighting the different vertical levels sensitive to these concentrations. There are also not enough AMoN sites over the entire time period to robustly

indicate either regional variations in surface ammonia concentration or whether a particular site is impacted by local emission changes. The range of simulated mean ammonia concentrations is 0.53 ppb less than the range observed at the available sites over the summers of 2008 to 2012 (Figure 3.7). Most of this missing range is from sites in the west and the Midwest, where agricultural ammonia emissions are higher. The observed range is likely influenced by high biomass burning emissions in the west and high temperature effects on partitioning in the Plains and the Midwest, which are greater than in the model. In addition, the base scenario does not account for variations in year-to-year changes in agricultural ammonia emissions, so we next assess how much influence these variations may have on the ammonia concentration.

3.6. Implementing Agricultural Ammonia Emissions Variability

3.6.1. Activity Scaling

The base scenario anthropogenic ammonia emissions are constant for all years of study. This is not realistic due to year-to-year changes in agricultural activity and the meteorological dependence of emissions (Section 3.6.2). We define agricultural activity as livestock population and fertilizer application. Using data from the US Department of Agriculture National Agricultural Statistics Service (USDA NASS) (www.nass.usda.gov), we compute annual scale factors for agricultural activity based on the changes in these sources (for a description of the methods, see Section A1 in Appendix A).

As shown in Figure 3.11, this scaling results in large increases in livestock ammonia emissions compared to the base scenario in Iowa (13% by 2012), although this is relatively constant during the study period (only a 2.3% increase between 2008 and 2012). The more dramatic change occurs over Texas and Oklahoma where livestock populations, largely beef cattle, decrease by 18% between 2008 and 2012 with a net loss of 20% compared to the base year by 2012. This large decrease in beef cattle population is due to extended extreme drought that reduces cattle food supply and forces higher cull rates [*Peel*, 2012].

The changes in ammonia emissions due to fertilizer application variations are smaller than those for livestock population (Figure 3.11). There is a noticeable decreasing trend in fertilizer application in the Texas and Oklahoma region due to a decrease in crop planting during

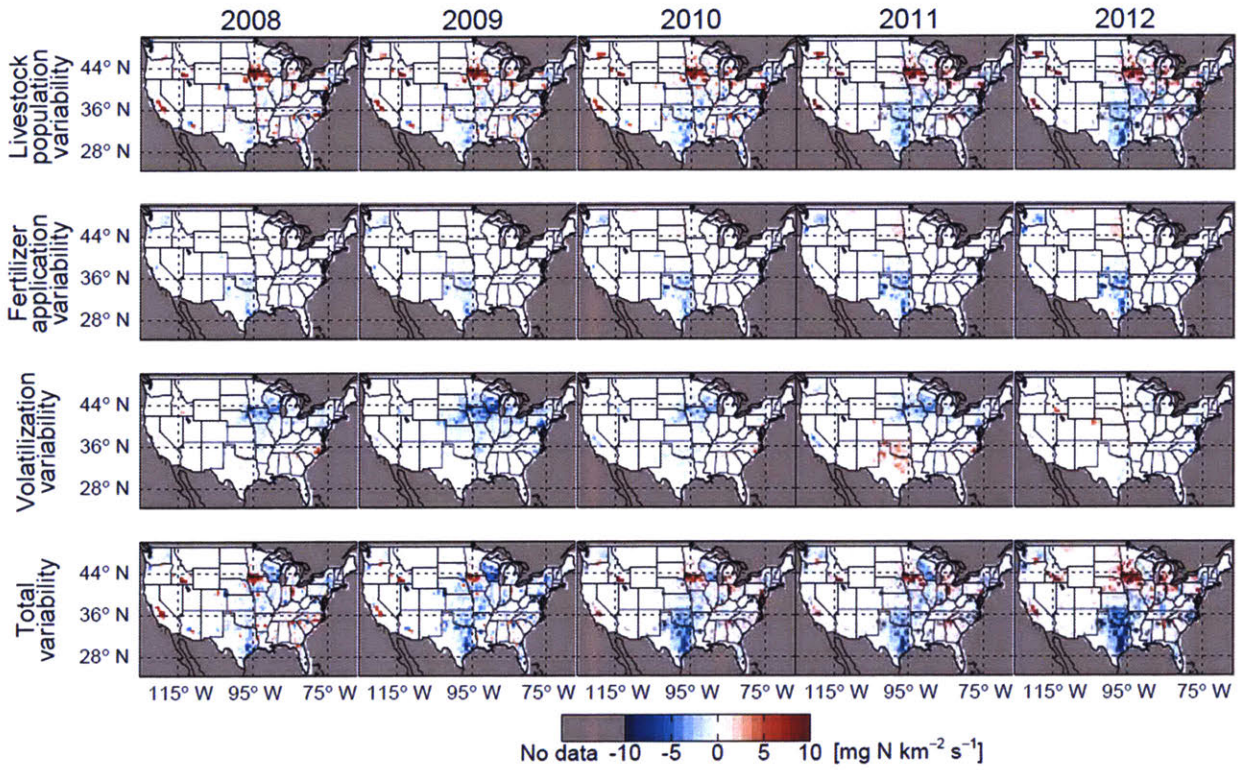

Figure 3.11. Differences in summer (JJA) agricultural ammonia emissions compared to base scenario emissions for (columns) 2008 to 2012 by including various emissions variability scenarios: (rows, top to bottom) livestock population variability, fertilizer application variability, volatilization variability, and all three combined.

the drought mentioned above (18% loss between 2008 and 2012), and an increase in the northern Plains of 20% compared to the base year by 2012. Our approach likely underestimates the year-to-year variation in fertilizer ammonia emissions in the Midwest (see Section A1 for details).

Although some locations experience large changes in total anthropogenic ammonia emissions due to activity variations (e.g., –13% in Texas and Oklahoma), the US mean change is only about –2.5 %. This is consistent with the EPA Trends data, which suggest a 3.0% decline in ammonia emissions between 2008 and 2012. Our changes present a spatial distribution of these shifts, however, rather than one national trend value.

3.6.2. Volatilization Scaling

The anthropogenic ammonia emissions in the base scenario also do not account for changes in the transfer of ammonia from the surface to the atmosphere due to temperature and wind speed variability (referred to together here as changes in volatilization). Higher

temperatures (increased volatility) and greater wind speeds (increased transport) lead to higher ammonia emissions. We compute monthly scale factors that account for the effects of temperature and wind speed on both livestock and fertilizer emissions. This generally follows the methods used by *Paulot et al.* (2014) for the Magnitude and Seasonality of Agricultural Emissions model for NH_3 (MASAGE_NH3) and is described in Section A2.

The changes in ammonia emissions computed from volatilization scaling are overall smaller, but they are more spatially variable compared to those due to agricultural activity (Figure 3.11). The scenario with volatilization scaling increases US mean summertime ammonia emissions by 0.1% in 2012 and decreases emissions by 3.2% in 2009 compared to the base scenario. Together, activity and volatilization scaling add 2.8% variability compared to the mean of the base scenario over the US. This variability is largest over the Midwest (6.4%) and the Texas and Oklahoma (14%) regions.

3.6.3. Resulting Changes to Ammonia Concentration

We simulate the ammonia concentrations for two cases as described above: (1) with added activity (livestock + fertilizer) variability of ammonia emissions and (2) with both activity and volatilization variability of ammonia emissions. The results from these simulations are shown for column concentrations in Figure 3.12. Changes for volatilization alone are calculated as the difference between the two scenarios (not shown). Since summer meteorology generally favors the gas phase of the ammonium nitrate equilibrium, most ammonia resides in the gas phase, and nearly all changes to the ammonia concentrations in our scenarios correspond directly to changes in the ammonia emissions. Thus, changes for both simulations are of similar magnitude, with more spatial and temporal variability caused by incorporating volatilization variability into the emissions. Activity emission variability decreases the mean US summer column by only 0.01×10^{16} molec cm^{-2} (2%) throughout 2008 to 2012 compared to the base scenario, and adding volatilization variability has no further effect on this mean. Activity and volatilization variability oppose one another, leading to a net decrease of only 0.01×10^{16} molec cm^{-2} (4% of the base scenario range). Summertime R between daily IASI observations and the simulated column concentrations in 2011 and 2012 increases by up to 0.1 in the Midwest, but decreases by a similar magnitude in Texas and Oklahoma (compared with base

scenario magnitude R in Figure 3.6). At the surface, activity and volatilization emission variability decreases the mean US summer concentration by similarly small proportions (1–2%) and has a limited effect on the range of values between minimum and maximum year surface concentrations for this domain (Figure 3.7). The largest changes in surface ammonia concentration take place where the largest emission changes occur. In Texas and Oklahoma, ammonia concentration decreases by 0.5 ppb or 17% of the base scenario for summer 2012, the year with the largest changes.

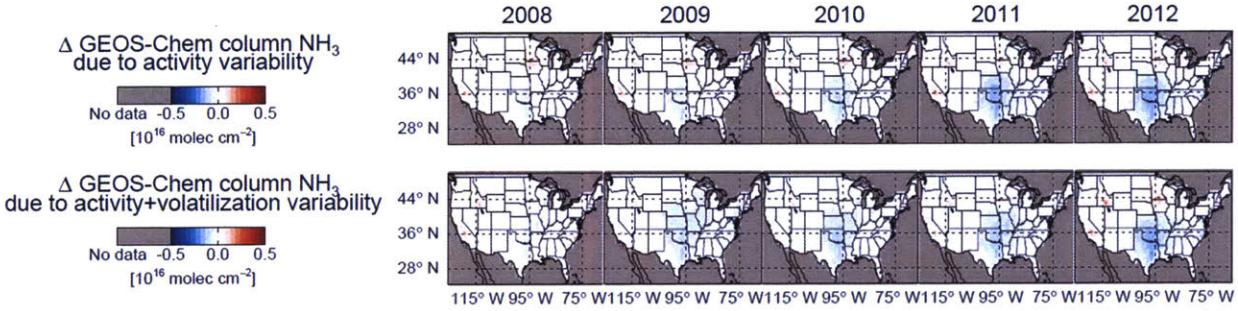

Figure 3.12. Changes in simulated summer (JJA) surface ammonia concentration from the base scenario caused by including variable ammonia emissions for (columns) 2008 to 2012: (rows, top to bottom) activity (livestock population and fertilizer application) variability and activity with volatilization variability. Compare to the baseline ammonia column shown in Figure 3.3.

The "best" scenario (including both activity and volatilization emission variability) also does not greatly improve the simulation bias or range compared to AMoN observations. For the sites with observations from 2008 to 2012, the scenario with activity and volatilization agricultural ammonia variability further degrades the simulation in summertime, increasing the bias from –0.93 to –1.02 ppb (Figure 3.7). For the 2011–2012 timeframe when more sites are available, the magnitude of the mean summer bias increases from –0.02 to –0.07 ppb. This is likely skewed toward the numerous low-concentration sites in the eastern US that start observing in 2011. However, variations in the ammonia emissions do moderately improve the ability of the model to capture year-to-year variations in surface ammonia concentrations measured at some AMoN sites, with increases in R during the entire study period of up to about 0.07 (mean increase of 0.01). At Horicon Marsh, Wisconsin, the R between observation and model improves from 0.65 to 0.67 in all seasons, but from 0.44 to 0.54 in summer only.

We find that year-to-year variations in regional ammonia emissions play a modest role in controlling observed variations in summertime ammonia concentrations. Our simulation

including this variation remains biased compared to observations throughout many regions of the US. There are several factors that may contribute to the remaining simulation bias of ammonia concentration magnitude and variability compared to the observations. Much higher spatial resolution may be required to adequately capture ammonia concentrations in areas with high horizontal concentration gradients (see Figure 3.4a); however, given the sparse coverage of the AMoN network, it is challenging to assess the role that site placement plays in biasing our comparisons. Additionally, better observational constraints, such as satellite products with vertical sensitivity information, could help identify the source of bias in the model.

3.7. Impacts of Ammonia Variability on Surface $PM_{2.5}$ and Nitrogen Deposition

Ammonia neutralizes acids in the atmosphere to produce $PM_{2.5}$ under appropriately cool and humid meteorological conditions. Changes in ammonia emissions, acid-precursor emissions, climate, and meteorology may all influence the surface $PM_{2.5}$ concentration. The potential for further formation of $PM_{2.5}$ (defined here as the sum of ammonium, sulfate, and nitrate) can be described by the gas ratio (GR) [*Ansari and Pandis*, 1998], as defined by Equation (3.1):

$$GR = \frac{[NH_x] - 2[SO_4^{2-}]}{TNO_3}. \quad (3.1)$$

The concentrations in Equation (3.1) are in molar units. The seasonal mean GR over all 5 years (2008–2012) as simulated by our GEOS-Chem base scenario is shown over the US in Figure 3.13. A GR >> 1 indicates little potential for further ammonium nitrate formation given additional ammonia emissions, while 0 < GR < 1 generally indicates that this potential does exist, under the appropriate meteorological conditions. None of the simulated seasonal mean GR values are below 0, which would indicate incomplete neutralization of sulfate. We recognize that the transition around GR = 1 occurs gradually as ammonia increases, but note that a large portion of the US exhibits a GR well above or below 1 in all seasons.

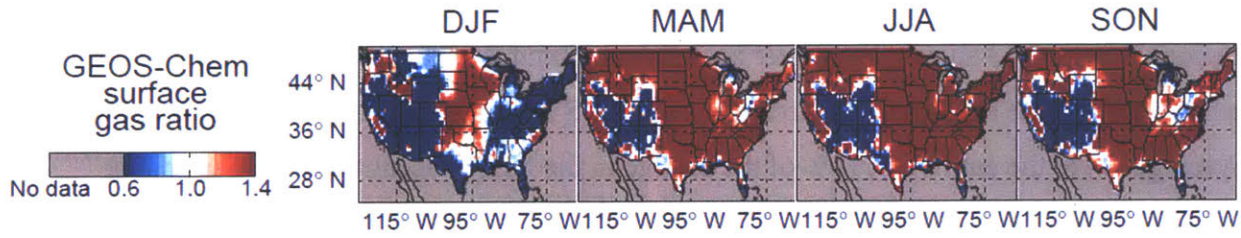

Figure 3.13. Base scenario simulated mean seasonal gas ratio (GR) for all years (2008–2012): (left to right) winter (DJF), spring (MAM), summer (JJA), and fall (SON). All values are greater than zero.

In the summer, we find that the surface $PM_{2.5}$ concentration is weakly sensitive to ammonia emission changes described in Section 3.6 (–0.6% in summer 2012 compared to the base simulation) (Figure 3.14). The gas phase of the ammonium nitrate equilibrium is favored under summer meteorological conditions, and the GR values in Figure 3.13 show that ammonium nitrate formation potential exists only in the Intermountain West. Thus, nearly all change (89%) in the NH_x concentration from changing ammonia emissions remains in the gas phase. There is essentially no change in ammonium sulfate as all sulfate in ammonia emissions regions has already been neutralized (GR > 0). Rather, Figure 3.14 shows that changes in the surface $PM_{2.5}$ are driven by anthropogenic SO_x and NO_x emission reductions (34% $PM_{2.5}$ reduction from 2008 to 2012) and meteorology. Although not evaluated here, summertime $PM_{2.5}$ may be affected during overnight periods when temperature decreases and relative humidity increases and via formation of minor salts such as ammonium oxalate, which are more likely to form during periods of high photochemistry.

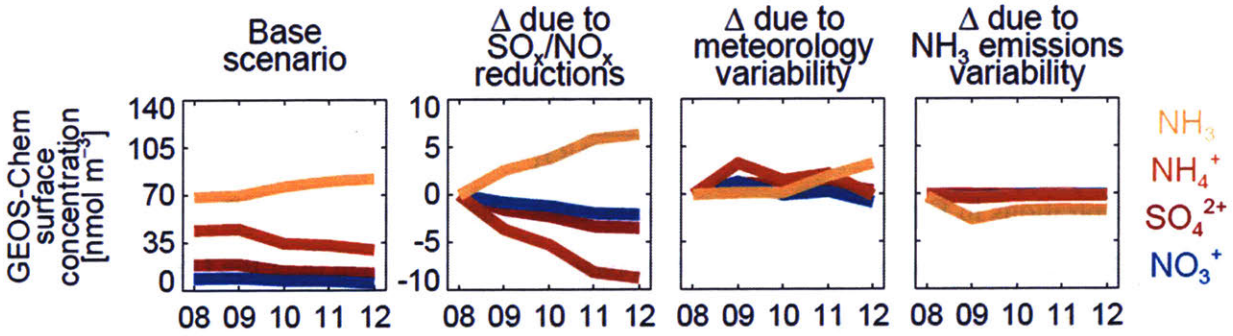

Figure 3.14. Mean summer (JJA) surface concentrations over the US for relevant gas and particle species (ammonia gas (light orange), ammonium particle (dark orange), sulfate particle (red), and nitrate particle (blue)) for 2008 to 2012 for several scenarios: (left to right) base scenario, changes from the base scenario due to anthropogenic SO_x and NO_x emissions reductions, assimilated meteorology variability, and added agricultural ammonia emissions variability.

Although changes in ammonia emissions are much smaller in the winter, both the meteorological and chemical conditions promote a higher potential for $PM_{2.5}$ formation in certain regions. Figure 3.13 shows that winter is chemically unique such that there is potential for ammonium nitrate to form throughout the eastern US should ammonia emissions increase. Averaged over the entire US, 78% of the change in the NH_x concentration from changing ammonia emissions remains in the gas phase during the winter in our final simulation, which includes ammonia emissions variability. This value remains fairly high since most of the change in ammonia emissions occurs in the area of GR > 1 (Plains) during the winter (Figure 3.13).

However, as SO_x and NO_x emissions decrease throughout the study period, this area where GR > 1 expands, reducing ammonium nitrate formation potential (not shown). Given the potential for ammonium nitrate formation, it may be more important to understand the variability of ammonia emissions during the winter (coldest temperatures, lowest ammonia emissions) to accurately simulate $PM_{2.5}$. Unfortunately, this is the time period when infrared satellite data exhibit the lowest sensitivity.

The spring (MAM) and fall (SON) seasons (which are colder, but with more moderate ammonia emissions) represent transition periods when ammonium nitrate may form under certain conditions (e.g., *Chow et al.*, [1994]). Although the distribution of GR is generally consistent with summer during both seasons as a whole, Figure 3.13 shows that this potential ammonium nitrate response to changing ammonia emissions may exist just south of the Great Lakes. Examination of GR during individual months shows that the transition to GR > 1 in the eastern US occurs between March and April, and the reverse happens between October and November. This further narrows the range of time when ammonium nitrate formation may respond to ammonia emissions changes.

The reduction of NO_x emissions dominates changes in the total simulated nitrogen (N, sum of ammonia, ammonium, nitric acid and nitrate) over our study period and results in a total summertime N deposition decrease of 12% from 2008 to 2012. In the base scenario, this decrease is partially offset by meteorologically driven factors that increase NO_x emissions in 2012. The SO_x and NO_x emission reductions create no net effect on total NH_x deposition, but there is a shift away from the particle-phase flux (ammonium) toward the deposition of the gas phase (ammonia). As the simulated lifetime to total deposition of ammonia is shorter than that of ammonium (2.6 days vs. 7.5 days over the US in summer 2008), this shift in phase preference decreases the overall lifetime of NH_x. The shortening of the NH_x lifetime to deposition means that reduced N from agricultural sources will deposit closer to the source, perhaps reducing required fertilizer inputs, but also putting sensitive ecosystems located close to source regions at risk.

Meteorology greatly influences the variability in the magnitude of NH_x deposition. Simulated summertime NH_x deposition flux is dominated by gas-phase ammonia, rather than particle-phase ammonium. The summertime ammonium deposition that does occur is largely removed via wet processes, which is more sensitive to meteorology changes than to ammonia emissions changes. In the winter, ammonium deposition dominates the total NH_x deposition flux; however, changes during this season may not be representative of the entire year, as only 11% of US agricultural ammonia emissions in our base scenario occur during the winter, compared to 36% in summer. Together, these results indicate that wet ammonium deposition may not always be a good proxy for ammonia emission changes. This is especially true in dry locations or during particularly dry summers, which in turn also have higher ammonia emissions.

3.8. Conclusions

We use a combination of surface, column, and aircraft ammonia concentration measurements along with a chemical transport model to assess simulated ammonia concentrations and analyze the variability of ammonia over the US from 2008 to 2012. The model often underestimates the observed ammonia concentrations at the surface and those measured by aircraft throughout the column; however, these observations are most often located near large source regions. The model performs well in areas of lower observed concentrations, such as in the eastern US. The observed seasonality at the surface is well captured by the model, outside of the timing of springtime fertilizer application. However, concentration gradients are more difficult to represent, both horizontally and vertically, as the model is not able to simulate plumes of observed high concentrations.

The simulated concentrations are generally less variable than the observed year-to-year concentrations, but this variability is larger than previously expected given constant ammonia emissions in the model. The variability in simulated ammonia concentrations is largely driven by changes in meteorology, and including year-to-year variation in ammonia emissions from agricultural sources has minimal impact on this variability. This suggests that year-specific agricultural emissions are not critical to the simulation of summertime ammonia and $PM_{2.5}$ in regions that are not experiencing dramatic changes in agricultural activity. Summertime $PM_{2.5}$ formation is relatively insensitive to ammonia emissions changes, but the impacts of ammonia

emission changes may be more important in cool conditions such as wintertime livestock emissions and spring crop planting.

The large role that meteorology plays in controlling atmospheric ammonia concentrations (coupled to the dynamic gas-particle partitioning) suggests that it can be challenging to use a global model to test simulated ammonia concentrations, understand how these concentrations correlate spatially with emissions sources, and assess whether emissions controls have led to expected trends in ammonia concentration. Indeed, changes in observed atmospheric ammonia concentrations may often be a poor proxy for changes in ammonia emissions. These challenges support the need for better observing systems for ammonia to test regional simulations. New satellite ammonia products (e.g., from CrIS) with dense observations may better provide observational constraints, allowing for a more quantitative comparison with models. Future surface monitoring sites should be distributed across source and background regions, make higher temporal resolution measurements, and measure both gas- and particle-phase NH_x. This will reduce the variability due to meteorology and source condition, shown in our study to be large, and better constrain the entire NH_x budget.

Appendix A: Description of Ammonia Emission Scaling Methods

A1. Activity Scaling

Scaling of agricultural activity refers to the influence changing livestock population and fertilizer application has on ammonia emissions. For livestock population, we use data from the USDA NASS for cattle, goats, chickens, hogs, and sheep. The portion of beef cattle vs. dairy cattle is determined by the ratio of beef cows to dairy cows. The census population of each species per county is gridded to the nested simulation grid box resolution for 2002, 2007, and 2012 to obtain the animal density in each grid box. We weight each species density by its relative emission factor (emission per head) to calculate the emissions value per grid box [*Pinder et al.*, 2004; *Faulkner and Shaw*, 2008; *Velthof et al.*, 2012; *Paulot et al.*, 2014]. Linear interpolation of effective emission is applied between census dates, and the emission for each year is scaled against the base year of 2005, as that corresponds to the NEI-2005 used in the base scenario, to achieve an annual scale factor for livestock population. These scale factors are applied to the livestock portion of the anthropogenic ammonia emissions.

We use data for county-wide fertilizer expense (gridded to nested resolution grid boxes) and the national fertilizer price index from the USDA NASS to develop annual scaling factors for fertilizer application. Fertilizer expense census data are available for 2002, 2007, and 2012. Each of these years is matched with the fertilizer price index (price per mass) for that year to calculate the total fertilizer mass purchased in each grid box. We assume all fertilizer purchased is applied to a field or that a similar fraction of fertilizer purchases is left unused in each year. Fertilizer mass for each of these years is interpolated linearly and then scaled in comparison to 2005 values as with livestock population above. These scale factors are then applied to the fertilizer portion of the anthropogenic ammonia inventory.

One weakness in scaling the base NEI-2005 is that the emissions for that inventory are specified for August, when fertilizer application is low, and thus there is limited fertilizer magnitude to scale in the Midwest. Fertilizer emissions from NEI-2005 in the Midwest make up about 5% of total anthropogenic emissions in that region at all times. In NEI-2011, however, fertilizer emissions make up about 10% of total anthropogenic emissions in August, and this increases to about 30% for summer and about 60% for spring. Any fertilizer activity scale factor

applied to NEI-2005 in the spring and summer will have a much smaller effect on the magnitude of the fertilizer ammonia emissions than if applied to NEI-2011, and thus our scaling on fertilizer emissions is likely to be underestimated. Resulting emission magnitude changes are shown in Figure 3.11.

A2. Volatilization Scaling

Scaling of due to volatilization refers to the effects temperature and wind speed have on ammonia emissions from both livestock and fertilizer sources. We develop monthly scale factors (individually for all 5 years) to approximate these effects. This procedure generally follows the methods used by *Paulot et al.* [2014] for MASAGE_NH3. Emissions magnitudes are not needed, since we scale all variability to the 2005 base year. Therefore, we weight each emission source by the relative importance of temperature and wind speed. Fertilizer ammonia emission (E) is similarly dependent on temperature and wind speed everywhere, and is represented by Equation (A1) [*Søgaard et al.*, 2002]:

$$E = 1.02^{T} \times 1.04^{w}, \quad \text{(A1)}$$

where the 2 m temperature (T) and 10 m wind speed (w) values used in the calculation are from the GEOS-5 meteorology used in the simulation. Livestock manure emissions vary differently depending on the location of the manure: application, housing, or storage. The application portion varies as fertilizer above in Equation (A1). The housing and storage portions vary by a different relationship, Equation (A2) [*Gyldenkærne et al.*, 2005]:

$$E = T_e^{0.89} \times V^{0.26}, \quad \text{(A2)}$$

where ammonia emissions (E) incorporate effective temperature (T_e) and ventilation rate (V). Storage temperature (T_e) and ventilation rate (V = w) are not species-dependent, but housing T_e and V do vary by species and their housing types. The relative weight of each manure emissions component (application, housing, and storage) is also species dependent [*Velthof et al.*, 2012]. Each month is scaled from the base year (2005) emissions in that month, and so the emissions changes depend on the meteorology of 2005. For example, the T in the Midwest in both summers 2005 and 2012 are similarly above the 10- and 35-year mean T from MERRA. This decreases the effect of volatilization on ammonia emissions in the Midwest in summer 2012 while using this method. These scale factors are then applied separately to the livestock and fertilizer

portions of the anthropogenic ammonia inventory as appropriate. Resulting emission magnitude changes are shown in Figure 3.11.

Supplement

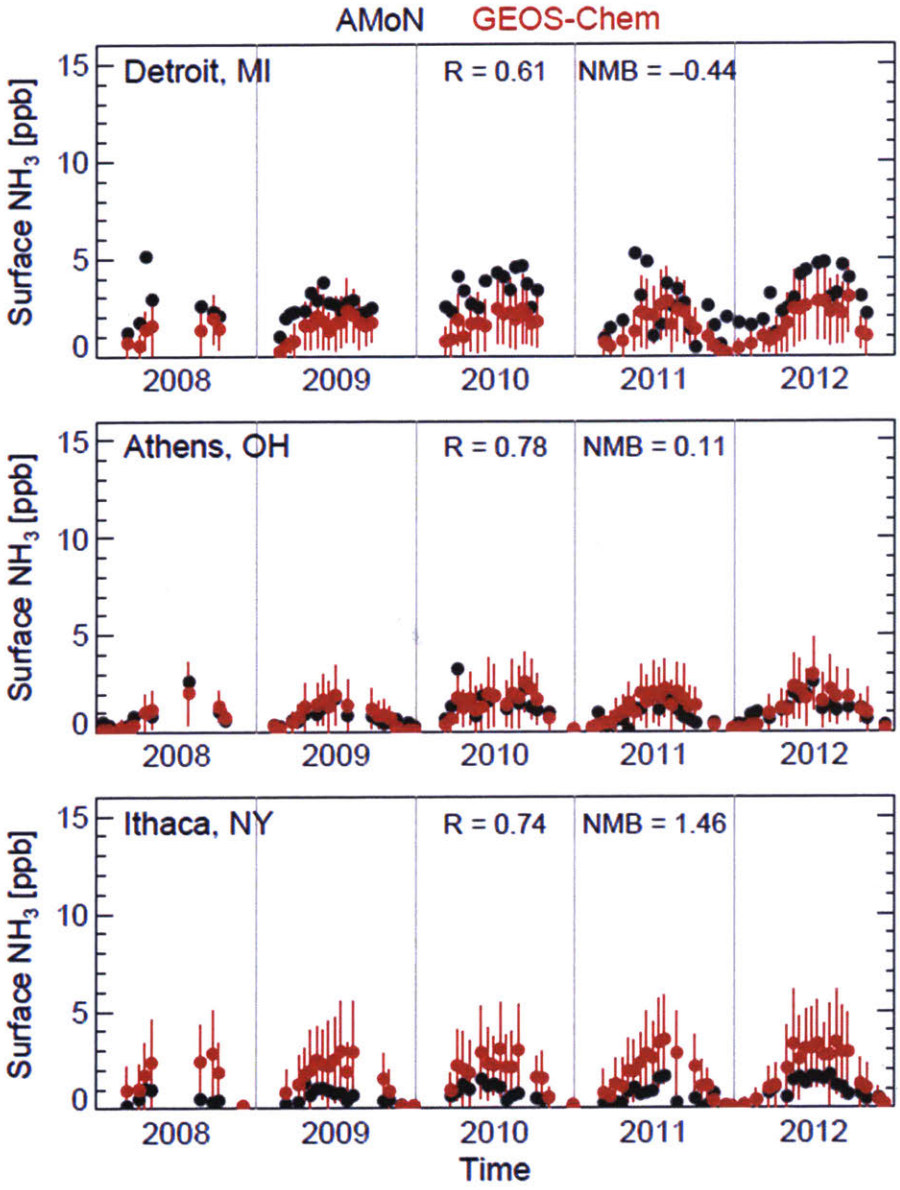

Figure S1. Same as Figure 3.8, but for: (top, urban) Detroit, Michigan (MI), (middle, mixed forest / agricultural) Athens, Ohio (OH), and (bottom, mixed forest / agricultural) Ithaca, New York (NY).

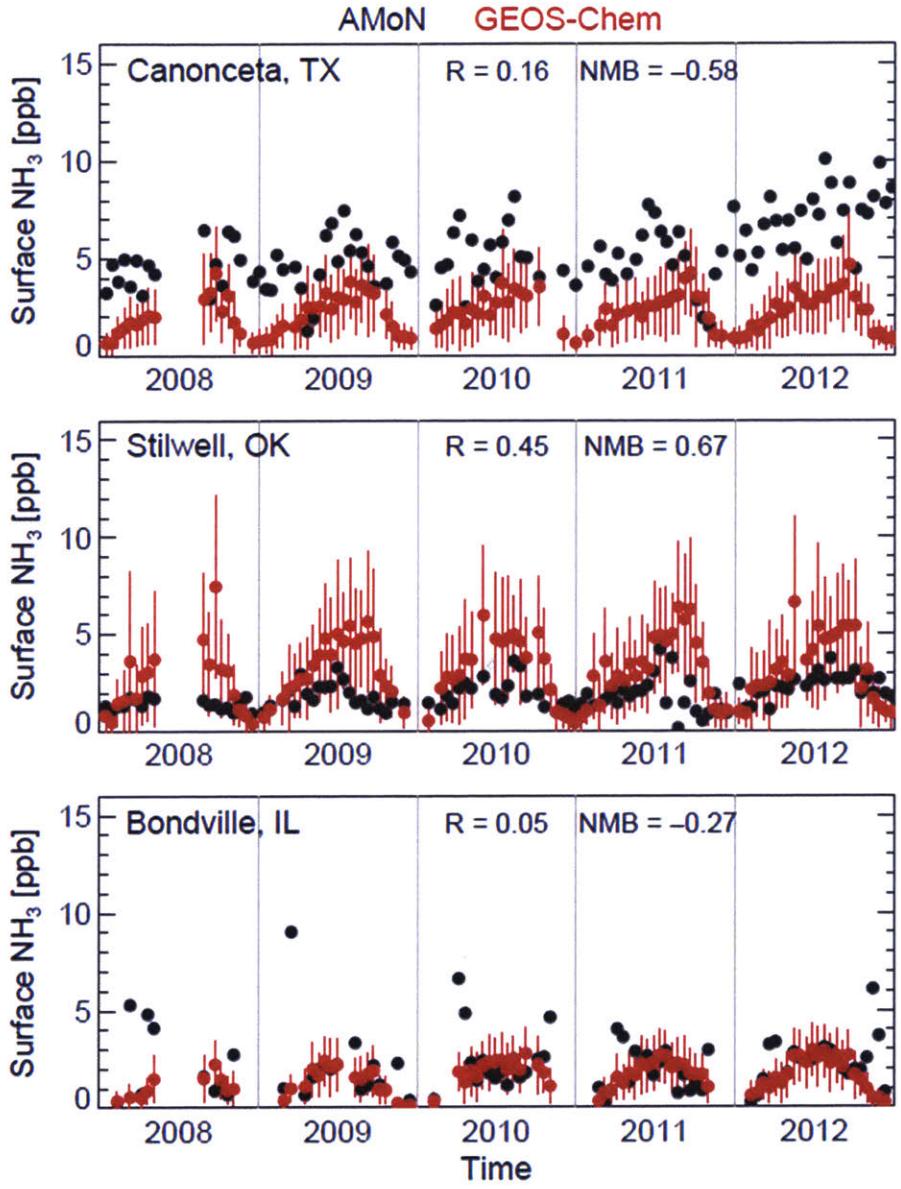

Figure S2. Same as Figure 3.8, but for: (top, agricultural) Canonceta, Texas (TX), (middle, agricultural) Stilwell, Oklahoma (OK), and (bottom, agricultural) Bondville, Illinois (IL).

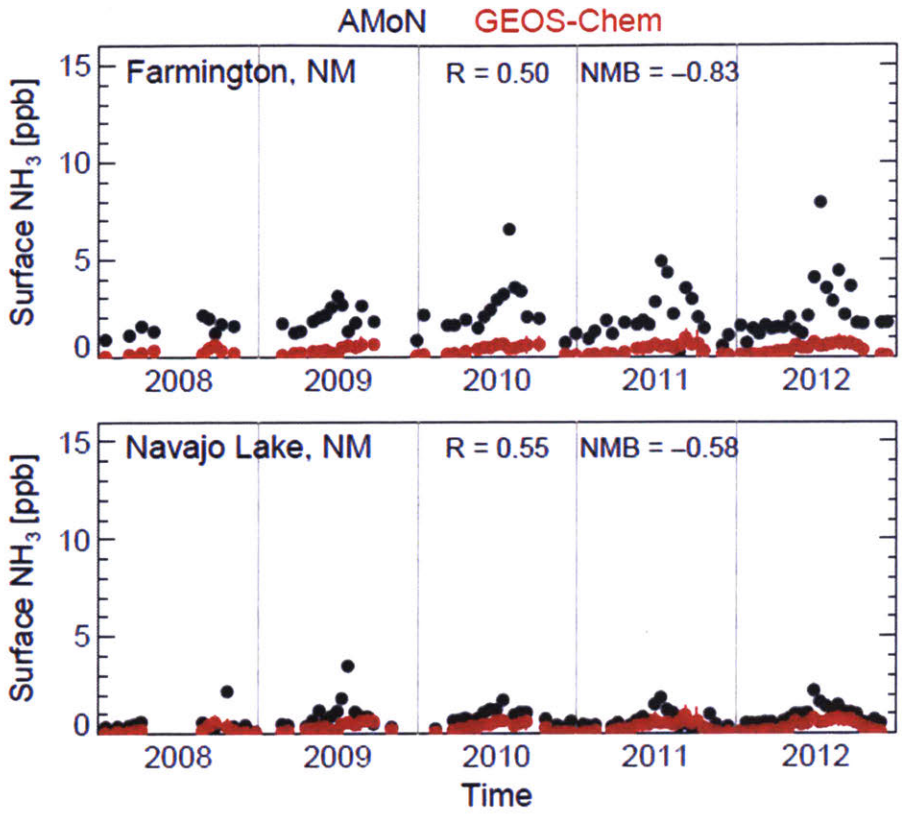

Figure S3. Same as Figure 3.8, but for: (top, varying topography / high horizontal gradient) Farmington, New Mexico (NM) and (bottom, varying topography / high horizontal gradient) Navajo Lake, NM.

Chapter 4. The Impact of Ozone and Particulate Matter Air Pollution on Global Crop Production

4.1. Introduction

Exposure to air pollution leads to over 4 million premature deaths per year [*Cohen et al.*, 2017]. At the same time, pressure on food production continues to rise with increasing global population. The close proximity of human population to crop production areas means that anthropogenic influences on air quality (defined here as ozone and particulate matter (PM)) have had and will continue to have an impact on our ability to adequately feed this growing human population. As of 2014, the United States (US), Canada, Europe, India, and China make up 52% of the global population and together are responsible for 72%, 76% and 51% of global maize, wheat and rice production, respectively [*FAOSTAT*, 2017; *United Nations*, 2017]. In China, which accounts for 19% of global population, rapid industrialization contributes to frequent air quality problems [*Guo et al.*, 2014]. These air quality concerns occur alongside intense food production schemes, illustrated by crop production often exceeding the county's population proportion (21%, 17% and 28%). In less developed countries, such as India where population is expected to increase by more than 25% by 2050, food-related stress may accompany the push to industrialize. Given the importance of these intense food production areas, it is vital to quantify the relevant air quality impacts on crop growth in order ensure proper guidance for future air quality and agricultural policy.

Surface-level ozone (O_3), usually associated with urban air pollution, is formed from the oxidation of carbon monoxide (CO), methane (CH_4) and non-methane volatile organic compounds (NMVOCs) in the presence of nitrogen oxides ($NO_X = NO + NO_2$). Ozone has a negative impact on crop production by reducing gas-exchange and inflicting phytotoxic damage on plant tissues [*Sitch et al.*, 2007; *Wilkinson et al.*, 2011; *Lombardozzi et al.*, 2012]. The crop-specific relationships between surface ozone concentration and crop yield loss have been established using several exposure metrics. These metrics either account for mean exposure (e.g., M12, M7) or cumulative exposure over a threshold concentration (e.g., AOT40). Observations relate the individual metric for ozone exposure to relative yield (RY) for a specific crop [*Adams et al.*, 1989; *Lesser et al.*, 1990; *Mills et al.*, 2007]. For example, wheat is found to be more

sensitive to ozone damage than maize and rice. These relationships have been used by other studies to perform global crop-damage assessments. *Van Dingenen et al.* [2009] find present day (2000) RY losses due to ozone to be 3–5% for maize, 7–12% for wheat and 3–4% for rice, with ranges due to variation in exposure metric. *Shindell et al.* [2011] show that future (2000 to 2030) changes in vehicle emissions will reduce RY losses due to ozone for all crops in North America and Western Europe, while the opposite is expected in India and China. Similar methodology is applied by *Tai et al.* [2014] to examine the confounding effects of ozone pollution control and climate change on crop production.

Much less studied is the effect of PM on crop production. PM can be directly emitted (e.g., mineral dust, sea salt, and black carbon particles) or formed through chemical processes (e.g., sulfate, nitrate and ammonium inorganic and organic carbon particles). The make-up of PM in a particular location is dependent on its source and chemical environment. PM scatters light, reducing the total shortwave (SW) light which reaches the surface, but also increases the diffuse fraction (DF) of this light (SW = direct + diffuse, $DF = \frac{\text{diffuse}}{\text{SW}}$). Whereas direct light only reaches the top leaves of the plant, an increase in diffuse light allows the radiation to penetrate farther down to lower levels [*Kanniah et al.*, 2012]. The overall change (both sign and magnitude) in crop productivity from these competing effects (SW vs. DF) depends on local light conditions and crop type. For example, crops with a C_3 photosynthetic pathway (e.g., wheat) are much more likely to become light saturated than C_4 crops (e.g., maize) [*Chapin et al.*, 2002]. Depending on the saturation levels of both the sunlit and shaded leaves of a plant, a reduction in SW from full sunlight would affect C_4 plants more, but an increase in DF to shaded leaves would more quickly cause an increase in C_3 plant productivity than for C_4 plants.

Greenwald et al. [2006] modify an existing process-based crop model to incorporate effects from scattered and diffuse light. This study uses offline meteorology and specified aerosol optical depth (AOD) at specific sites to quantify the effect of PM on yields of maize, wheat and rice. They find relationships between yield and AOD for each crop at each location by relating the DF to the radiation use efficiency (RUE). RUE refers to how well the plant uses its available light, accounting for physiological and environmental differences such as those mentioned above. They modify the RUE in their simulation as a function of DF according to

various possible levels (e.g., max ΔRUE = 0%, 50% or 100%), following from *Sinclair et al.* [1992]. Under the most realistic scenario at various sites, the effect of PM on yield was found to be –10 to 0% for maize, –5 to +5 % for wheat and –10% to +10% for rice. This assumes that the RUE of maize (C_4) is less sensitive to DF (max ΔRUE = 0–50%) than the RUE of wheat and rice (C_3) (max ΔRUE = 50–100%). The relationship between DF and RUE is highly uncertain, both in magnitude (max ΔRUE) and in shape. For example, *Rochette et al.* [1996] observe a linear relationship over a maize field, rather than the hyperbolic relationship used in *Greenwald et al.* [2006]. These various DF-to-ΔRUE relationships are shown in Figure 4.1. The enhancing effect of aerosol diffuse light on plant productivity, related by AOD, has also been observed by *Cirino et al.* [2014] and *Strada et al.* [2015]. However, these relationships are not easily translatable to DF and RUE values, and it is difficult to remove the impacts of clouds from such observations.

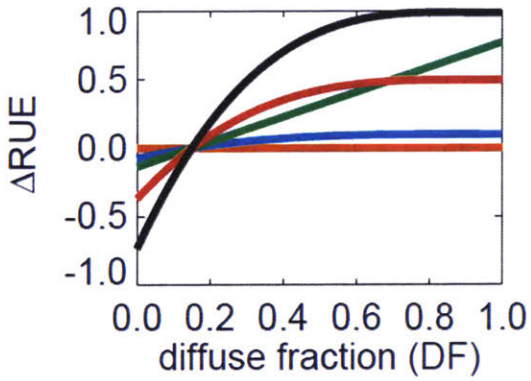

Figure 4.1. Relationship between DF and ΔRUE for various assumptions: max ΔRUE=0% (orange), 10% (blue), 50% (red), and 100% (black) from *Greenwald et al.* [2006], and linear (green) from *Rochette et al.* [1996].

Previous global modeling studies have focused on the effects of diffuse light on total carbon or net primary productivity. For example, *Mercado et al.* [2009] quantify the spatially-varying effects of aerosols on carbon flux and productivity as a whole using a land-surface scheme along with AOD from a separate chemistry simulation, but they do not focus on crop production. They find that the changing global diffuse fraction increased the land carbon sink by 25% between 1960 and 1999. *Matsui et al.* [2008] study the effect of aerosol light scattering on photosynthesis on a regional level with high spatial resolution using a land surface model. They find the effect to be largest (and positive) at noontime under cloudless conditions, but less over croplands than over forests due to a lower leaf area index (LAI) in these regions. Previous studies have also looked at how ozone and/or PM impact natural vegetation and the carbon cycle,

often by incorporating more advanced canopy or leaf-scale process modeling [*Yue and Unger*, 2014; *Strada and Unger*, 2016; *Yue et al.*, 2017]. Our study is the first to contrast the large-scale impact of ozone and PM on global managed vegetation (crops).

This study uses the GEOS-Chem chemical transport model to simulate ozone and PM along with the Rapid Radiative Transfer Model for GCMs (RRTMG) to simulate PM's impact on radiation. We then use existing relationships from previous studies described above to quantify the effects of both ozone and PM on crop production globally under both current and future emissions scenarios. We contrast only the light scattering effects of PM with the negative impacts of ozone and do not consider all other secondary effects (indirect on clouds, hydrology, temperature, etc.).

4.2. Tools

4.2.1. GAEZ Crop Production

The base crop production used in this study comes from the Global Agro-Ecological Zones (GAEZ) assessment for 2000 (www.fao.org/nr/gaez), developed by the Food and Agriculture Organization (FAO) of the United Nations along with the International Institute for Applied Systems Analysis (IIASA).We scale the 2000 base production to 2010 values determined by the country-level trend between 2000 and 2010 from the FAO (http://www.fao.org/faostat). GAEZ crop production information is available at $5' \times 5'$ horizontal resolution and we maintain this high spatial resolution when adjusting production by the relative air quality effects calculated on the GEOS-Chem grid.

The global baseline crop production is 871 Tg for maize, 667 Tg for wheat, and 705 Tg for rice according to GAEZ values scaled to 2010. Maize production is largest in the US+Canada region, accounting for 37% of global production. China+Southeast (SE) Asia follows with 23% of global maize production. Wheat production is greatest in Europe and makes up 31% of global production, while China+SE Asia and India hold about a 15% share of wheat production each. China+SE Asia and India dominate rice production, with 44% and 33% of the global total, respectively. While we present global numbers, the domain of our figures focuses mainly on the industrialized, developed regions of the northern hemisphere and the staple crops found there:

maize, wheat, and rice. Over three-quarters of these crops are grown in this domain. On average, the southern hemisphere air quality is cleaner. Food crops in those regions are more varied (e.g., pulses in Africa), and their response to environmental stress is not as well understood. We neglect soybean production, because a metric relating potential carbon production to SW and DF consistent with the other crops (see Section 4.3.2) is not available.

4.2.2. GEOS-Chem Simulation

4.2.2.1. General Description

We simulate emissions, chemistry, and wet and dry deposition processes relevant to ozone and PM concentrations in the troposphere in three dimensions using the GEOS-Chem chemical transport model (www.geos-chem.org). The model is driven by GEOS-5 meteorology from the NASA Global Modeling and Assimilation Office (GMAO) and is run globally at 2° × 2.5° horizontal resolution with 47 vertical hybrid sigma layers for 2009 and 2010. Model time steps are set to 15 min for transport and convection and 30 min for emissions and chemistry. The model description generally follows standard GEOS-Chem v10-01 as we have only implemented minor bug fixes. GEOS-Chem contains sulfate-nitrate-ammonium thermodynamics coupled to an ozone–VOC–NO_x–oxidant chemical mechanism [*Park et al.*, 2004; *Pye et al.*, 2009]. ISORROPIA II partitions ammonium nitrate between the gas and particle phase [*Fountoukis and Nenes*, 2007]. The wet deposition scheme in the model is described by *Liu et al.* [2001] for aerosols and by *Amos et al.* [2012] for gases, and the dry deposition processes are described by *Wang et al.* [1998] and *Zhang et al.* [2001].

Global anthropogenic emissions of NO_x, carbon monoxide, and sulfur dioxide (SO_2) come from the Emission Database for Global Atmospheric Research (EDGAR) v4.2 [*EC-JRC/PBL*, 2011]. The global Reanalysis of the TROpospheric chemical composition (RETRO) inventory is used for anthropogenic NMVOC emissions [*Hu et al.*, 2015a], with global anthropogenic and natural ammonia emissions from the Global Emission Inventory Activity (GEIA) inventory. Biofuel emissions follow *Yevich and Logan* [2003]. For anthropogenic (and in some cases biofuel) emissions, regional inventories overlay these global inventories in the US (National Emissions Inventory for 2011 (NEI-2011) v1 implemented by *Travis et al.* [2016]), Canada (Criteria Air Contaminants (CAC) inventory), Mexico (Big Bend Regional Aerosol and

Visibility Observational (BRAVO) Study Emissions Inventory [*Kuhns et al.*, 2005], Europe (European Monitoring and Evaluation Programme (EMEP) (www.ceip.at)), and East Asia (MIX Asian emissions inventory [*Li et al.*, 2014]). We modify NEI-2011 by reducing non-electric generating unit (non-EGU) NO_x emissions by 60% as suggested by *Travis et al.* [2016]. Black carbon (BC) and organic carbon (OC) from anthropogenic sources are emitted globally, described by *Bond et al.* [2007] and implemented by *Leibensperger et al.* [2012]. Global biomass burning emissions come from the Global Fire Emissions Database v4.1 (GFED4) [*van der Werf et al.*, 2017]. Dust emissions are described by *Fairlie et al.* [2007], and sea salt emissions are described by *Jaeglé et al.* [2011]. Lightning NO_x emissions are from *Murray et al.* [2012], soil NO_x emissions are from *Hudman et al.* [2012], and biogenic VOC emissions are from the Model of Emissions of Gases and Aerosols from Nature (MEGAN) v2.1 from *Guenther et al.* [2012] and implemented by *Hu et al.* [2015b]. 10% of monoterpene emissions by carbon are added to OC emissions as done by *Park et al.* [2003].

We output the hourly surface ozone concentration for use in quantifying the ozone impact on crop production. The ozone concentration in the surface grid box, nominally 120 m deep, is scaled to a 1 m canopy height using the simulated aerodynamic resistance and dry deposition velocity for cropland. This method for accounting for the near-surface concentration gradient is described by *Zhang et al.* [2012] and has been previously implemented for ozone by *Lapina et al.* [2016] and *Travis et al.* [2017]. Hourly PM concentrations at all vertical levels are read into RRTMG for calculation of their radiative impacts. In our simulation, PM refers to the sum of all simulated aerosol species: sulfate (SO_4^{2-}), nitrate (NO_3^-), ammonium (NH_4^+), BC, OC, sea salt and dust.

4.2.2.2. RRTMG

RRTMG [*Iacono et al.*, 2008] uses the correlated-k method to quickly calculate the atmospheric radiation flux throughout the vertical column and was implemented online into GEOS-Chem by *Heald et al.* [2014], together referred to as GC-RT. RRTMG simulates extinction from water vapor, ozone, greenhouse gases, aerosols, clouds and Rayleigh scattering over 16 longwave and 14 SW bands. In GC-RT, ozone and aerosol concentrations are simulated in GEOS-Chem, greenhouse gas concentrations are prescribed from climatology, and water

vapor concentration and cloud properties are taken from the GEOS-5 assimilated meteorology. A log-normal size distributed bulk scheme is used for all aerosols (2 bins for sea salt, 4 for dust), and consistent optical properties have been set in GC-RT. Using GC-RT, we output hourly downward SW radiation at the surface with and without PM under simulated real-time cloudiness (all-sky) conditions. We modify the GC-RT code to output the direct and diffuse components of SW under the same conditions in order to calculate the DF. In our analysis, we consider the radiative impacts of PM as a whole, rather than individual aerosol composition properties such as those exhibited by scattering vs. absorbing particles.

4.2.2.3. Evaluation with Observations

We compare the mean daytime GEOS-Chem surface ozone concentrations (scaled to 4 m height) with observations from the Air Quality System (AQS) network (www.epa.gov/aqs) in the US during summer (JJA) 2010. We find that the model is biased high by about 8 ppb. This high bias is consistent with previous studies (e.g., *Travis et al.* [2016]). When comparing observations from the EMEP network (www.emep.int) in Europe to GEOS-Chem during the same time period, the model is biased high by about 9 ppb. This comparison is shown in Figure 4.2. The addition of halogen chemistry by *Sherwen et al.* [2016] suggests that future versions of the model will have lower ozone concentrations. Similar network surface ozone measurements are not available for India and China during this time period.

We also compare ozone and PM surface observations from a site at the Indian Institute of Science Education and Research (IISER) Mohali in Chandigarh, India provided by *Sinha et al.* [2015] and *Pawar et al.* [2015], respectively, with simulated concentrations from GEOS-Chem (Figure 4.3). While an exact comparison between our 2010 simulation and the 2011-2014 observations is not possible, we find the model is biased slightly high, but does a good job reproducing the seasonal cycle of ozone concentration, with elevated concentrations during the dry phase (October–June) and lower concentrations during the wet phase of the monsoon. However, the model is unable to reproduce the magnitude of decline in ozone concentration at the peak of the wet season (July–September). For PM, the model generally reproduces the magnitude of the observed concentrations. The model fails, however, to capture the observed

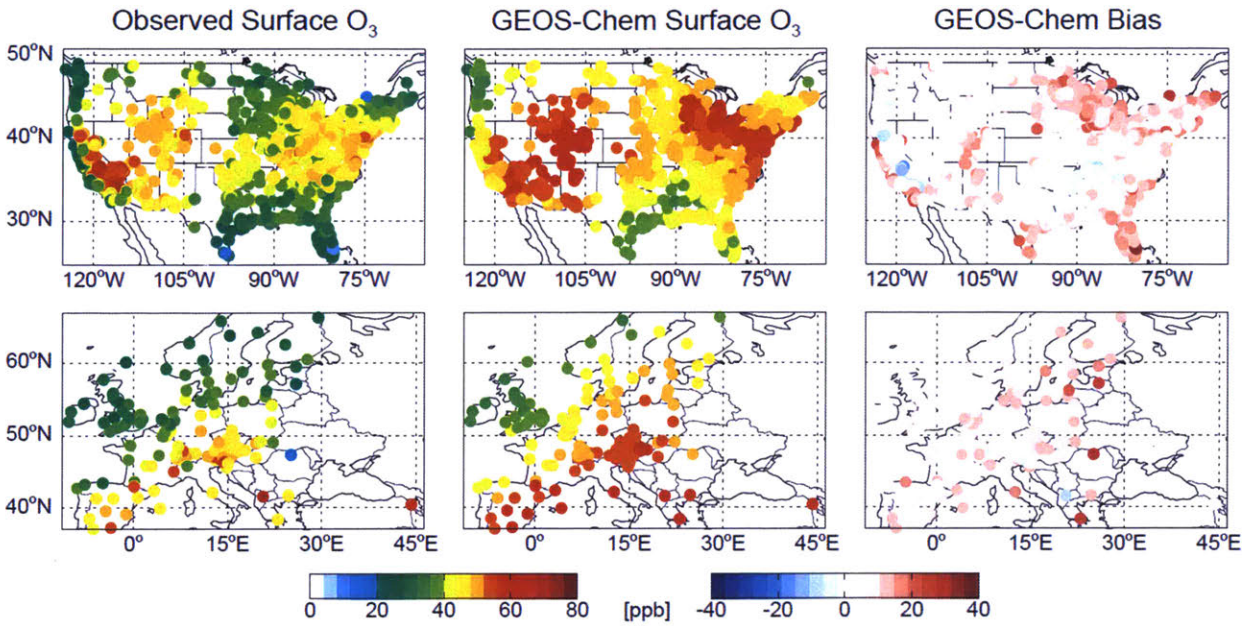

Figure 4.2. For both (top row) AQS network sites over the US and (bottom row) EMEP network sites over Europe: comparison of mean daytime (8:00–20:00 local time) (left column) observed and (middle column) GEOS-Chem simulated surface ozone concentrations for summer (JJA) 2010. Bias (simulated-observed) shown in right column.

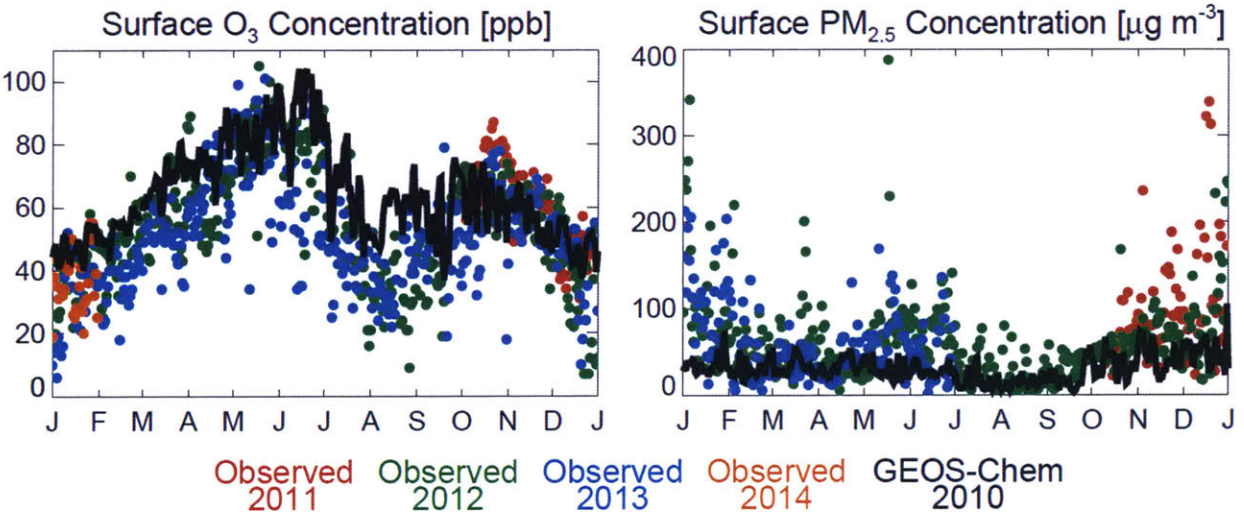

Figure 4.3. Daily surface (left) mean daytime (9:00–16:00 local time) ozone concentration and (right) mean daytime (12:00–16:00 local time) $PM_{2.5}$ concentration at Chandigarh, India. Observations in colored dots: 2011 (red), 2012 (green), 2013 (blue), and 2014 (orange). GEOS-Chem simulated values in black lines.

higher concentrations during the dry phase of the seasonal cycle, especially over the winter (November–February).

Finally, we compare the observed SW and DF at an AmeriFlux site over a maize field in Mead, Nebraska with those simulated parameters from GC-RT during JJA 2010. Overall, the

magnitudes of the observed parameters compare well with the model. By including PM and clouds in the calculation of the SW and DF in GC-RT, we improve the comparison in terms of variability simulated throughout the time period compared to a simulation without clouds and PM. For example, including clouds and PM results in the simulation of a range of lower SW values (slope reduces from 1.17 to 1.11) and higher DF values (slope increases from 0.44 to 0.93), more consistent with those observed.

4.3. Methodology

4.3.1 Ozone

Using the hourly surface ozone concentrations from GEOS-Chem, we calculate ozone exposure metrics over the final 92 days (roughly 3 months) of a growing season ending in 2010 as by *Tai et al.* [2014]. This growing season is determined by the University of Wisconsin Center for Sustainability and the Global Environment (UW SAGE) global crop calendar containing the planting and harvest dates by crop species and variety (maize, spring wheat, winter wheat, and rice) [*Sacks et al.*, 2010]. The spring (28% by mass, globally) and winter (72%) wheat distribution at each location is taken from the crop planting dates used in the pSIMS/DSSAT crop model [*Elliott et al.*, 2014]. Although double-cropping does occur significantly in some regions, such as the sub-tropics, our study assumes mutual exclusivity at a given location. We calculate AOT40 (Equation 4.1) for maize, wheat and rice, M12 (Equation 4.2) for maize, and M7 (Equation 4.3) for wheat and rice:

$$\mathrm{AOT40} = \sum_{t=08:00}^{t=19:59} 10^{-3}([O_3]_t - 40) \tag{4.1}$$

$$\mathrm{M12} = \frac{1}{n}\sum_{t=08:00}^{t=19:59} [O_3]_t \tag{4.2}$$

$$\mathrm{M7} = \frac{1}{n}\sum_{t=09:00}^{t=15:59} [O_3]_t, \tag{4.3}$$

where $[O_3]_t$ is the hourly surface ozone concentration in ppb, t the time each day in the summation and listed in local time, and n is the total number of hours in the growing season.

The global distribution of surface ozone using the M12 exposure metric is shown in Figure 4.4 for each crop. This figure has been filtered for grid boxes with a baseline crop production (see Section 4.2.1) of greater than 0.01 Mg km^{-2}. M12 is generally higher over areas with large anthropogenic influence, including the US, Europe, India and China. This is especially true for summertime crops, such as maize and rice, whose growing seasons correspond with higher ozone concentrations. Lower ozone concentrations occur during the winter wheat growing season period, and this seasonal contrast is particularly noticeable in China, but also in the US. Each exposure metric is then related to RY using empirical relationships as listed in Table 4.1. Following *Van Dingenen et al.* [2009] and *Shindell et al.* [2011], we use the mean of these metrics for each species to calculate the total production change due to ozone.

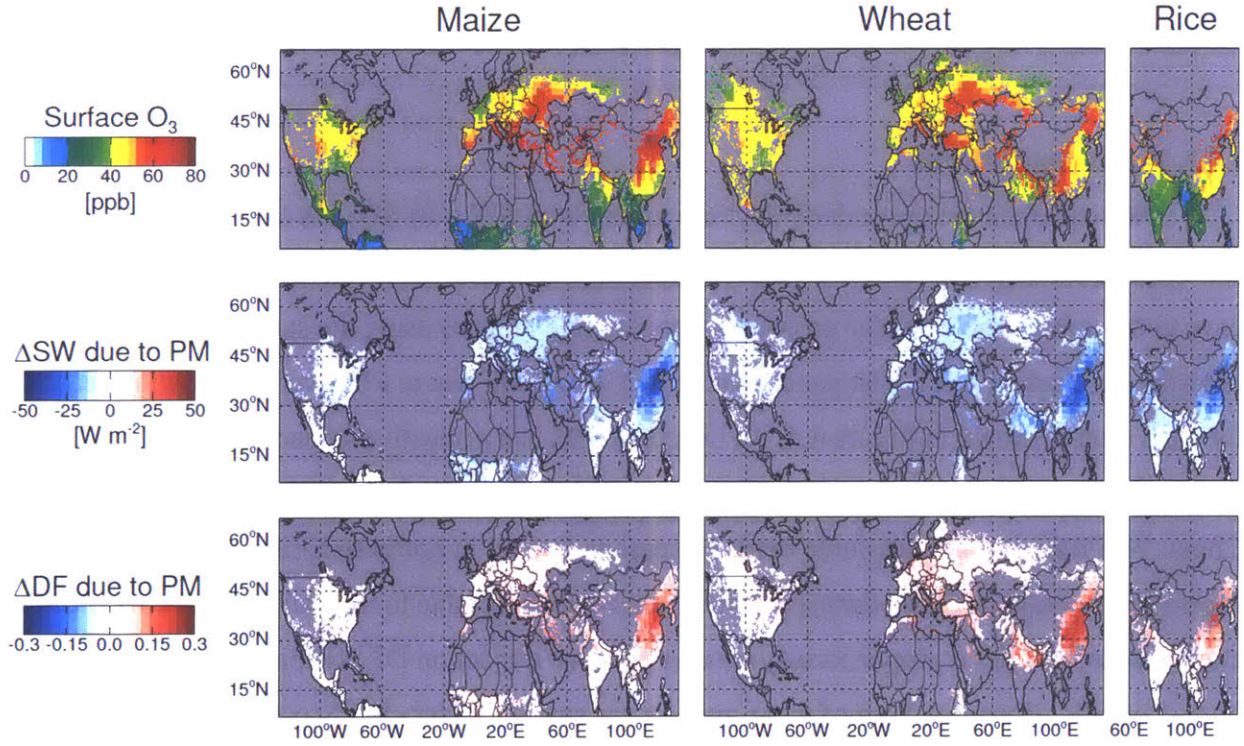

Figure 4.4. (top row) Mean daytime (8:00–20:00 local time) GEOS-Chem simulated ozone concentrations. Mean change in daytime (SW > 0) (middle row) downward SW radiation and (bottom row) DF of the SW radiation at the surface due to PM from GC-RT. Sampled to growing season ending in 2010 for (left column) maize, (middle column) wheat, and (right column) rice. Filtered for base crop production greater than 0.01 Mg km-2.

Table 4.1. Relationships between ozone exposure metric and relative yield (RY) due to ozone.

Crop	AOT40	M12/M7
Maize	$RY = 1 - (0.00356 \times AOT40)$ [*Mills et al.*, 2007]	$RY = \exp[-(M12/124)^{2.83}]/\exp[-(20/124)^{2.83}]$ [*Lesser et al.*, 1990]
Spring Wheat	$RY = 1 - (0.0163 \times AOT40)$ [*Mills et al.*, 2007]	$RY = \exp[-(M7/186)^{3.2}]/\exp[-(25/186)^{3.2}]$ [*Adams et al.*, 1989]
Winter Wheat	Same as spring wheat	$RY = \exp[-(M7/137)^{2.34}]/\exp[-(25/137)^{2.34}]$ [*Lesser et al.*, 1990]
Winter Wheat, China	$RY = 1 - (0.0228 \times AOT40)$ [*Wang et al.*, 2012]	
Rice	$RY = 1 - (0.00415 \times AOT40)$ [*Mills et al.*, 2007]	$RY = \exp[-(M7/202)^{2.47}]/\exp[-(25/202)^{2.47}]$ [*Adams et al.*, 1989]
Rice, China	$RY = 1 - (0.00949 \times AOT40)$ [*Wang et al.*, 2012]	

4.3.2. Particulate Matter

We calculate the mean daily daytime (hours with SW > 0) SW and DF from the hourly GC-RT output, both with and without PM under all-sky (cloudy) conditions. We sample these days to the entire crop calendar growing season ending in 2010 using the same calendar described in Section 4.3.1. The mean change in SW and DF due to PM over the growing season for each crop is shown in Figure 4.4. As expected, PM has a negative impact on SW at the surface and a positive impact on DF. The largest PM impacts (both for SW and DF) are over China. While similar in magnitude between seasons (crops) in northern China, the effect of PM is smaller in southern China during summer (maize and rice) due to increased cloud cover. Under cloudy skies, PM has a proportionally smaller positive impact on DF compared to the negative impact on SW. However, both of these impacts are smaller under cloudy conditions compared to when the sky is clear. Similarly, there is also a large seasonal variation in India caused by the monsoonal pattern. Cloudy conditions present during the wet season, the growing season for maize and rice, mask much of the impact of PM on radiation. The opposite is true during the dry season (winter wheat) when cloud-free skies allow for an enhancement in the effect of PM on SW and DF. The PM impacts on radiation are comparatively small in magnitude in other regions, although areas are still significant in terms of total productivity.

The potential carbon production for a crop is calculated on a daily basis with and without PM using the above daily SW and DF values and then summed over the growing season for the total potential carbon. Potential carbon is calculated following the DSSAT model for maize and wheat (Equation 4.4) and rice (Equation 4.5):

$$P_{carb} \propto 0.5 \times SW \times RUE_{s,DF} \quad (4.4)$$

$$P_{carb} \propto (0.5 \times SW)^{0.65} \times RUE_{s,DF}, \quad (4.5)$$

where P_{carb} is the potential carbon production, SW is the daily mean shortwave radiation from GC-RT and RUE_s is crop-specific radiation use efficiency. In the equations above, RUE_s is modified according to various DF-to-ΔRUE relationships. We calculate the effect of PM on crop production across 3 levels of impact: max ΔRUE = 0% (changes in SW only, direct effect), max ΔRUE = 50% (maximum 1.5 × RUE at DF=0.8), and max ΔRUE = 100% (maximum 2 × RUE at DF=0.8) [*Greenwald et al.*, 2006]. Finally, we calculate the relative carbon production with PM compared to without PM for each crop under each relationship.

4.3.3. Relative Crop Production

To calculate the crop production change due to ozone and due to PM at each ΔRUE relationship, we multiply the relative yield with ozone and the relative carbon production with PM, respectively, by global base production values for each crop from GAEZ as described in Section 4.2.1.

4.4. Results

4.4.1. Present-Day Impact of Air Pollution on Crops

The crop production changes due to air quality under current emissions (2009–2010) are shown in Figure 4.5. Crop production changes due to ozone is negative everywhere, with significant reductions globally. This negative effect ranges from wheat, which is most sensitive to ozone damage, at –11.9% to maize at –4.4% to rice at –3.4% global production change. This is consistent with the results of *Van Dingenen et al.* [2009].The high wheat sensitivity to ozone damage is reduced in terms of total production by the relatively lower winter ozone concentrations affecting winter wheat. Figure 4.6 shows regional crop production changes, and the ozone impact on wheat is consistently high in all regions. There is also a greater ozone

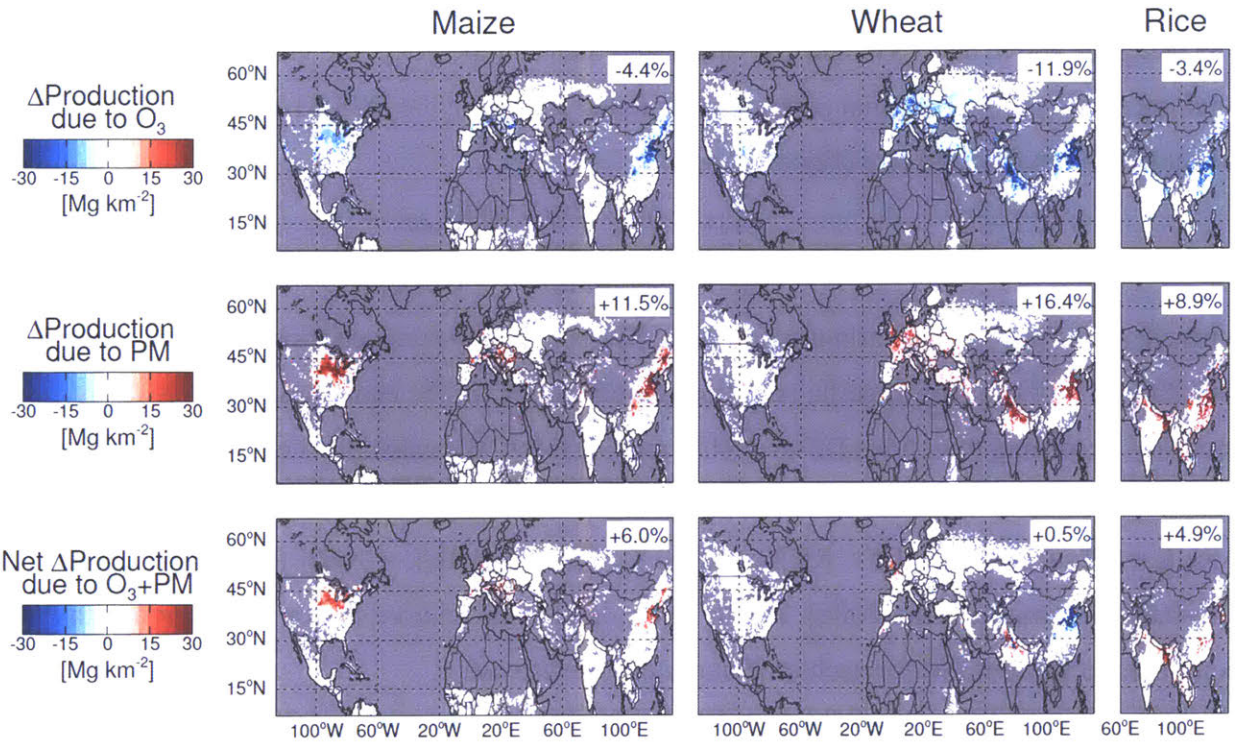

Figure 4.5. Change in crop production due to (top row) ozone, (middle row) PM with max ΔRUE=100%, and (bottom row) both ozone and PM. Sampled to growing season ending in 2010 for (left column) maize, (middle column) wheat, and (right column) rice. Filtered for base crop production greater than 0.01 Mg km $^{-2}$. Global relative production change shown in upper right.

impact on maize and rice production in China+SE Asia compared to other regions, due to high ozone concentrations in this region (Figure 4.4).

PM causes a significant enhancement in crop production throughout the globe, when the diffuse effect is calculated at max ΔRUE=100% (Figure 4.5). Given the high bias in our ozone simulation, we contrast the ozone impact with the largest possible impact of diffuse light. The impact of assuming lower sensitivity to the diffuse fraction explored in Section 4.4.2. Assuming max ΔRUE=100%, global crop production increase due to PM is +11.5% for maize, +16.4% for wheat, and +8.9% for rice. Figure 4.6 shows that the PM effect on crop production is especially large in China+SE Asia and India, regions with high PM concentrations. This is particularly dramatic for India wheat during the dry season with a gain of over 25%.

When the ozone and PM effects are combined using max ΔRUE=100% for PM to calculate the total impact of air quality on crop production (Figure 4.5), the net negative impact

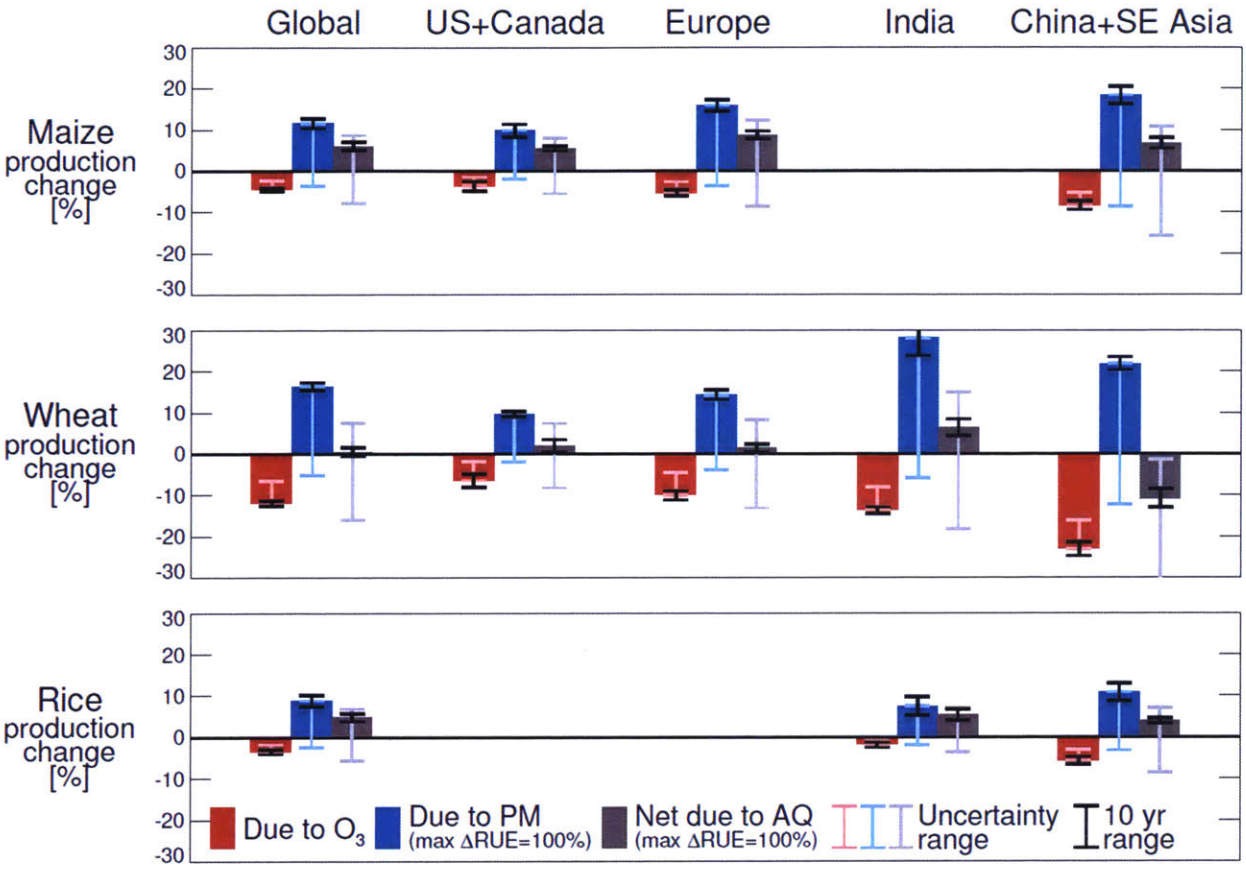

Figure 4.6. Regional relative change in crop production due to ozone (red bars), PM with max ΔRUE=100% (blue bars), and both ozone and PM (gray bars). Sampled to growing season ending in 2010 for (top row) maize, (middle row) wheat, and (bottom row) rice. Light red, light blue, and light gray lines indicate range of production from 0 to –10 ppb surface ozone concentration correction, from max ΔRUE=0% to max ΔRUE=100%, and from both effects, respectively. Black lines indicate range of production change over 10 years of variable meteorology. Regions with a base production lower than 5% of the global total are not shown.

is smaller than for ozone alone. In many regions, the net impact is positive, such as for China, northern US and Europe maize, India wheat, and India and China rice. This means that the diffuse effect from PM outweighs that of ozone damage in these locations. The net global production change due to air quality in this case is +6.0% for maize, +0.5% for wheat and +4.9% for rice. In this analysis, the ozone and PM effects are calculated separately, and we do not account for compounding effects. We also do not examine the effects of PM on cloud formation or PM deposition onto plant surfaces.

While we show detailed results from one particular growing season, it is important examine how this magnitude may change from year-to-year. Thus, we use Modern-Era Retrospective Analysis for Research and Applications v2 (MERRA2) meteorology from the GMAO to simulate the impacts of air quality on crop production for 10 growing seasons (9 for wheat) for 2001–2010. We hold anthropogenic emissions constant from year-to-year, varying only those emissions affected by meteorology. The 10 year range (min to max) of crop production change due to ozone alone, due to PM alone with max ΔRUE=100% and due to net air quality is plotted as bars in Figure 4.6 around the standard base run for a growing season ending in 2010 previously discussed. This range in production change is small compared to the ozone effect alone and to the variability in the ΔRUE relationship, which increases confidence that the results above are a robust representation of air quality impacts on crop growth beyond the 2010 growing season.

This analysis takes into account the total current ozone and PM from all sources. When isolating the impact of anthropogenic influenced air quality (since 1850) on crop production, we find that a significant portion of the PM effect (roughly half) is from natural sources (mainly dust). Nearly all of the ozone impact is anthropogenic in origin (influenced by the AOT40 threshold metric). Understanding the anthropogenic influences on crop production can have implications for air quality management strategies. For example, a policy which reduces ozone concentrations at the surface would be beneficial by enhancing food production, especially in regions like China and India. In contrast, a policy which causes a reduction in anthropogenic PM for the purpose of improving air quality would have a negative impact on crop production. As such, it is important to target air quality management such that the net gain is maximized and balanced with improvements for human exposure.

4.4.2. Uncertainty in the DF-to-ΔRUE Relationship

The relationship between DF and ΔRUE is uncertain, and we have calculated a range of possible impacts on crop production by changing the DF-to-ΔRUE relationship. This range is shown in Figure 4.6 for the PM effect only and for the net effect of air quality on crop production. For the case of max ΔRUE=0%, which can be referred to as the effect of direct radiation on PM on crop production, only the decrease in SW caused by PM is applicable. As

such, crop production decreases everywhere both when alone and when added to the impact of ozone damage. As the sensitivity to DF (max ΔRUE) increases, the impact of PM on crop production becomes more positive. For many regions and crops, this range is greater than the negative impact of ozone alone. The sensitivity of these results to the assumed response to diffuse radiation highlights the critical need for additional observational constraints on the response of crops to light. Further, the difference between C_3 and C_4 plants is not taken into account here since ΔRUE only varies by DF. A canopy model could better predict the distribution of light onto sunny and shaded leaves and the resulting RUE of the plant.

The most realistic relationship value may be closer to the max ΔRUE=50% assumption, especially for maize, which is less sensitive to an enhancement from DF, in which case at least some significant negative ozone impact is offset by the diffuse PM effect. However, we know that the model is biased high for surface ozone (see Section 4.2.2.3), so the net crop production change due to air quality when including the diffuse effect may be closer to the results we show with max ΔRUE=100%. For completeness, we include in Figure 4.6 the range of crop production change when a –10 ppb ozone concentration bias correction is applied both for ozone alone and for the net effect of air quality on crop production. While the absolute impact of air quality on crop production depends on the accurate simulation of ozone, PM, and the response of crop growth to these constituents, it is clear from these results that the PM impact on crop growth has the potential to be a major environmental factor in global food production.

4.5. Implications for Future Scenarios

In order to examine possible future scenarios for global crop production, we repeat the single growing season analysis using 2009–2010 GEOS-5 meteorology along with anthropogenic emissions for ammonia (NH_3), sulfur dioxide, sulfate, nitric oxide, BC, OC, and VOCs from the RCP 4.5 and RCP 8.5 future scenarios (tntcat.iiasa.ac.at/RcpDb). The difference between crop production change due to ozone, PM and net air quality in 2050 and 2010, which represents future change, under these scenarios is shown in Figure 4.7.

In the RCP 4.5 scenario, air quality is projected to improve (annual ozone and PM concentrations will decrease by about 10% and 50%, respectively) in all regions except India.

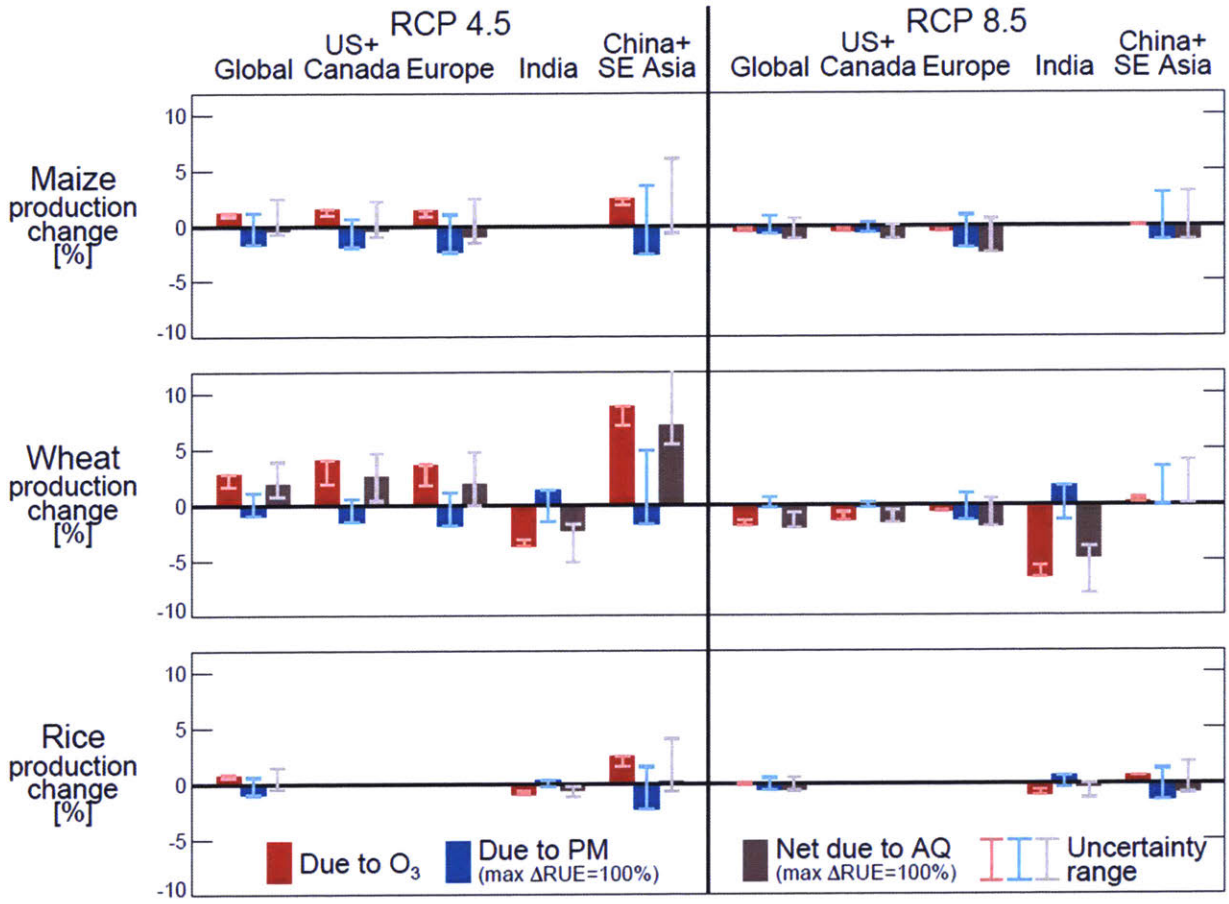

Figure 4.7. For both (left) RCP 4.5 and (right) RCP 8.5 emissions scenarios: regional relative change in crop production due to ozone (red bars), PM with max ΔRUE=100% (blue bars), and both ozone and PM (gray bars). Change from 2010 to 2050 for (top row) maize, (middle row) wheat, and (bottom row) rice. Light red, light blue, and light gray lines are as in Figure 4.6. Regions with a base production lower than 5% of the global total are not shown.

These improvements counteract each other, and there is little net impact on crop production for maize and rice, unless PM sensitivity to DF is less than estimated here (assuming max ΔRUE=100%). Production of wheat may increase by about 2% globally given its higher sensitivity to the ozone clean-up measures. In India, however, an increase in diffuse fraction given air quality degradation under RCP 4.5 dampens the crop production loss from ozone, with about 2% reduction expected.

Declines in crop production are more likely in the RCP 8.5 scenario, which is pessimistic in terms of air quality. Ozone increases in most regions, while anthropogenic PM continues to go down. Globally, this leads to a net total crop production loss for maize, wheat, and rice. As in RCP 4.5, both PM and ozone increase in India, but crop production decreases to a greater extent

as a larger increase in ozone is expected. In all cases, the impact of PM is reduced if a lower sensitivity to DF (max ΔRUE) is assumed.

4.6. Conclusions

Previous studies have quantified the reduction in crop yields and associated economic costs based on surface ozone alone, but it is imperative to understand all of the environmental impacts and limitations on crop growth given the pressure to enhance food production in the coming decades. This study broadens the study of environmental impacts on crop production by quantifying the impacts of both ozone and PM on current and future global crop production. We demonstrate that including the diffuse effect of PM on crop production can offset the negative impacts due to ozone. This offsetting nature of PM and ozone on crop production should feature in air quality management; future improvements in air quality may not be entirely beneficial to crop production, as would be assumed when considering only the impact of ozone damage. Such a scenario may even cause a net negative impact on crop production. Aerosol composition has not been examined in this study, however, we note that targeting specific aerosol types may have different effects on crop production. The range of uncertainty regarding the relationship between diffuse radiation (DF) and the response of the crop (ΔRUE) is large and warrants further experimental study. More work is also needed to understand the timing of these effects during the growing season. Finally, it may be important to consider how resource restrictions (e.g., limited water and nutrients) can impact these results.

Chapter 5. Resource and Physiological Constraints on Global Crop Production Enhancement from Particulate Matter and Nitrogen Deposition

5.1. Introduction

Stress on global food production continues to grow due to population growth. Simultaneously, anthropogenic activities are changing many aspects of the earth system. This supports the need to better understand how crop production may be limited by environmental impacts on the water, air, light, and soil required for efficient growth. For example, several studies have explored the impacts of climate and air quality on crop production, but this has generally been done without considering physiological limitations and other environmental stresses (e.g., water and nutrients) [*Greenwald et al.*, 2006; *Shindell et al.*, 2011; *Tai et al.*, 2014].

Particulate matter (PM), emitted through combustion and natural processes and formed through chemistry, is a source of air quality issues including reduced visibility and negative human health effects. PM also impacts crop production by modifying shortwave radiation at the surface. Through the scattering of light, PM decreases the total shortwave (SW) radiation at the surface, which is made up of direct and diffuse light (SW = direct + diffuse). PM also increases the diffuse fraction (DF) of this SW radiation ($DF = \frac{diffuse}{SW}$). Increased DF more evenly distributes light throughout the canopy of a plant, redirecting light away from (at times over-saturated) leaves in direct sunlight and onto shaded leaves. In this way, plants can more efficiently make use of incoming solar radiation. In the case of crops, PM can increase growth and production when the increase in efficiency outweighs the loss of SW radiation. This effect and previous work to understand it are fully introduced in Chapter 4. Briefly, *Greenwald et al.*[2006] use relationships between DF and a crop's radiative use efficiency (RUE), a measure of how effective a plant converts light into carbon, from *Sinclair et al.* [1992] along with varying meteorology and a crop model to estimate the impact of PM on crop yield. Assuming no restrictions on growth due to stresses at several sites, they find a large variation in impacts based on the DF-to-ΔRUE relationship chosen. Under the maximum relationship, maize increases by 0–10%, wheat increases by 0–5% and rice increases by 0–40% under varying cloud conditions.

Industrial agriculture, driven by the need to produce food for a growing human population, has modified the global nitrogen (N) cycle. By artificially fixing inert nitrogen gas into reactive forms, humans have increased the fluxes of nitrogen throughout the environment, including in the atmospheric, on land and in the water [*Galloway and Cowling*, 2002]. Nitrogen species in the atmosphere, both reduced and oxidized, return to the surface through deposition processes after being transported away from source regions. Anthropogenic influences on these fluxes change the nitrogen balance in land and water ecosystems. In natural systems, this can cause acidification and eutrophication, which negatively impacts the biosphere [*Erisman et al.*, 2007; *Beem et al.*, 2010]. The nitrogen can also impact crop production, by providing additional fertilization, increasing yields in areas which are nitrogen limited [*Goulding et al.*, 1998].

PM and nitrogen deposition are also connected: The release of excess nitrogen from fertilizer application and livestock production in the form of ammonia contributes to PM formation in the atmosphere under acidic conditions [*Seinfeld and Pandis*, 2006].Nitric acid (HNO_3), an oxidized form of nitrogen oxides (NO_x) emissions from mobile and industrial sources, contributes both to the nitrogen burden and these acid conditions. Nitrogen can also be incorporated in PM as organic nitrates when biogenic volatile organic compounds (BVOCs) react with NO_x [*Mao et al.*, 2013].

In Chapter 4, we quantify the impact air quality (ozone and particulate matter (PM)) has on current and future global crop production. This analysis, while consistent with the approach generally applied to estimate air quality impacts on crops, fails to account for the set of physical and biological restrictions placed on crop growth and production. In particular, crop production enhancement due to the diffuse effect of PM is considered to be unlimited. It is important, however, to consider the more realistic system, including water and nitrogen stresses and physiological caps placed on crop production. In this study, we employ a crop production model to better simulate impacts of PM on crop production with these constraints. This expands on the unstressed assumptions of *Greenwald et al.* [2006]. We then extend our examination of atmospheric impacts on crop production by applying nitrogen deposition to the simulated crop production.

5.2. GEOS-Chem Atmospheric Chemistry Model

The GEOS-Chem model (www.geos-chem.org) simulates the global concentration of gases and particles in three dimensions. Simulated PM concentrations are read into the Rapid Radiative Transfer Model for GCMs (RRTMG) to estimate the impact of PM on radiation throughout the atmosphere [*Heald et al.*, 2014]. Together these models are referred to as GC-RT. The model version and setup used here is the same as for the standard 2010 emissions scenario in *Schiferl and Heald* [in prep] and is fully described in Chapter 4. In this study, we use hourly output of surface SW radiation and the diffuse and direct portions of this SW radiation from GC-RT both with and without PM under all-sky (real time variation in cloudiness) conditions. These are used to calculate the DF of the SW radiation. As in Chapter 4, PM refers to the sum of all simulated aerosol species: sulfate (SO_4^{2-}), nitrate (NO_3^-), ammonium (NH_4^+), black carbon (BC), organic carbon (OC), sea salt and dust. We also use daily output of nitrogen deposition flux, including the wet and dry deposition simulated for all nitrogen species. Nitrogen mass deposited from five species, ammonia (NH_3), ammonium, nitric acid (HNO_3), nitrate, and nitrogen dioxide (NO_2), make up 97% of the total simulated nitrogen deposition for 2010.

5.3. pDSSAT Crop Model

5.3.1. Description

We use v4.6 of the Decision Support System for Agrotechnology Transfer (DSSAT) crop system model (www.dssat.net), along with v2.0 of the parallel System for Integrating Impact Models and Sectors (pSIMS) (www.github.com/RDCEP/psims), together called pDSSAT, to simulate the global production of maize, wheat, and rice. DSSAT provides a unified interface which combines various crop simulation models [*Jones et al.*, 2003]. Inherently a point model, DSSAT uses daily meteorological data (minimum temperature, maximum temperature, precipitation and solar radiation) along with soil and management information at a given location. The model then calculates a crop yield at harvest taking into account soil-plant-atmosphere dynamics throughout the growing season. Plant growth, in our case, is determined by the Crop-Environment Resource Synthesis (CERES) model module for each crop.

pSIMS allows for the globally gridded simulation of crop yield at $0.5° \times 0.5°$ horizontal resolution by running DSSAT in parallel at each grid box using consistent input data and settings

[*Elliott et al.*, 2014]. pDSSAT uses daily meteorological information from AgMERRA [*Ruane et al.*, 2015], a version of the NASA Modern-Era Retrospective Analysis for Research and Applications (MERRA) product developed for use in the Agricultural Model Intercomparison and Improvement Project (AgMIP) [*Rosenzweig et al.*, 2013]. Soil inputs come from the Global Soil Dataset for Earth System Modeling (GSDE) [*Shangguan et al.*, 2014]. Additional required information includes the range of planting dates [*Portmann et al.*, 2010; *Sacks et al.*, 2010], distribution of cultivars (based on local growing degree days (GDD)), and fertilizer application amounts [*You et al.*, 2000] at each grid box. Except for the soil inputs, which are modified in pSIMS v2.0, these data are consistent with those used by the global gridded crop model (GGCM) intercomparison portion of AgMIP [*Rosenzweig et al.*, 2014].

5.3.2. Integration of GEOS-Chem with pDSSAT

Using the hourly SW, diffuse and direct radiation output from GC-RT, we calculate the daily mean daytime (SW > 0) SW and DF for each GEOS-Chem gridbox (2° × 2.5° horizontal resolution) for all of 2009 and 2010. We group the nitrogen deposition fluxes of individual species into two groups, reduced nitrogen (NH_x) and oxidized nitrogen (NO_y), and calculate the daily total flux for each group for the same time period. The daily SW and DF values, along with the daily NH_x and NO_y deposition flux values, are regridded to the pDSSAT resolution and integrated into the input meteorology.

For the particulate matter simulations (see Section 4.1), the daily SW and DF are used in the pDSSAT crop-specific plant growth modules to modify the potential carbon production as in Chapter 4. Equation 5.1 is used for maize and wheat, and Equation 5.2 is used for rice.

$$P_{carb} \propto 0.5 \times SW \times RUE_{s,DF} \quad (5.1)$$

$$P_{carb} \propto (0.5 \times SW)^{0.65} \times RUE_{s,DF}, \quad (5.2)$$

where P_{carb} is the potential carbon production, SW is the daily mean shortwave radiation from GC-RT and RUE_s is crop-specific radiation use efficiency [Ritchie et al., 1998]. For simulations with PM affecting SW and DF, SW modified by PM from GC-RT is used as input for these relationships only and is not used in other functions dependent on solar radiation, such as evaporation (i.e., the GC-RT SW without PM remains applied to these processes). In this study,

we apply only the maximum DF-to-ΔRUE relationship discussed in Chapter 4, where max ΔRUE=100% at DF=0.8 [*Greenwald et al.*, 2006].

For the nitrogen deposition simulations (see Section 4.2), NH_x and NO_y nitrogen deposition fluxes are applied daily as fertilizer on the surface layer of the soil as NH_4^+ and NO_3^-, respectively. We apply these deposition fluxes beginning 30 days prior to the planting date at each location. The timing of this initiation is uncertain, as the fate of deposited nitrogen is unknown and impacts can be assessed over both short and multi-year time scales [*Goulding et al.*, 1998]. We discuss the impact of this assumption in Section 4.2.

5.3.3. Base Simulation

We configure pDSSAT to run for 2009 and 2010 with water and nitrogen stress turned off. Our modification for potential carbon production using input from GC-RT is applied to SW only (with SW values from GC-RT without PM). Maize, wheat and rice are simulated independently. We sample the results for each crop for the growing season ending in 2010. For example, crops planted in northern hemisphere spring and harvested in fall are grown entirely within 2010, while winter crops are planted in fall 2009 and harvested in spring 2010. Crop production is determined by multiplying the pDSSAT crop yield by the crop area from the Global Agro-Ecological Zones (GAEZ) assessment for 2000 (www.fao.org/nr/gaez) scaled to 2010 as in Chapter 4. The results from this simulation, our base simulation, are shown in Figure 5.1. As in Chapter 4, we focus our figures on the industrialized areas of the northern hemisphere, which rely heavily on maize, wheat and rice, while maintaining the global simulation results for reference. Since our base simulation has no restrictions on water and nitrogen use, the simulated crop production vastly surpasses that from GAEZ. For maize, this is 2066 Tg from pDSSAT compared to only 871 from GAEZ. Simulated wheat production is 2617 Tg, and simulated rice production is 1253 Tg compared to GAEZ values of 667 Tg and 705 Tg, respectively.

We rerun the crop model with water stress only, nitrogen stress only, and both stresses together to test the sensitivity of the base simulation to these resources (Figure 5.1). Water stress occurs when the amount of soil water available is below the potential transpiration rate of the

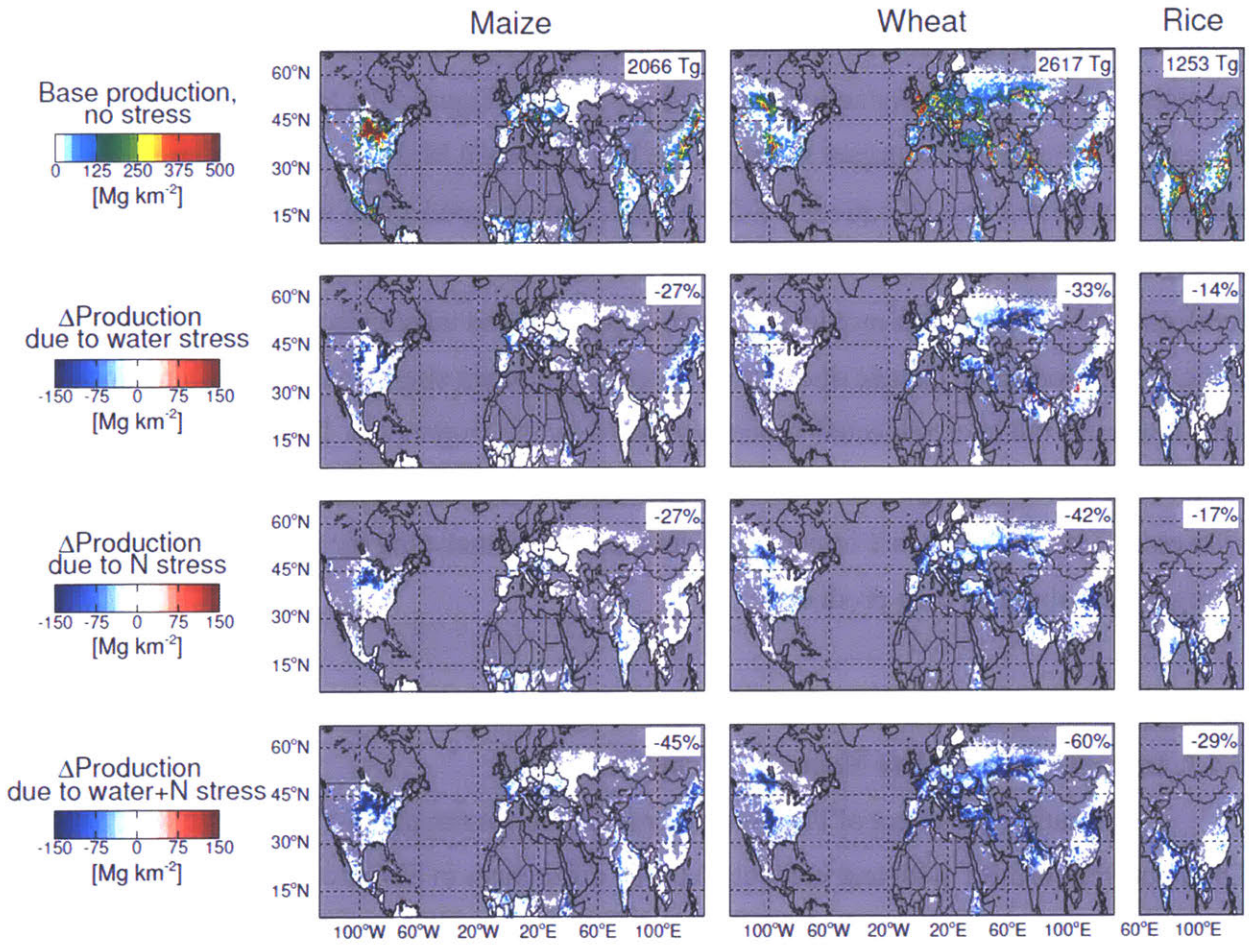

Figure 5.1. (top row) Crop production from base pDSSAT scenario (GC-RT SW only, no PM) with no stress applied for growing season ending in 2010. Difference in crop production due to (second row) water stress, (third row) nitrogen stress, and (bottom row) both water and nitrogen stresses. For each row: (left column) maize, (middle column) wheat, and (right column) rice. Filtered for GAEZ base crop production greater than 0.01 Mg km ^{2}. Global production (top) or relative production change (second row-bottom) shown in upper right.

plant. For maize, the negative effect of water stress on production is most evident in the US Plains and northern China and causes a 27% production reduction globally. The effect of water stress is larger globally on wheat, 33% reduction, and is located in the southern US Plains, northern China, and throughout western Asia. Rice production is impacted the least by water stress, with only a 14% reduction, mostly in northern India. Water stress is dependent on the precipitation prescribed from the meteorology of that growing season, so these results will vary from year to year.

Nitrogen stress occurs when the plant tissue nitrogen concentration is less than the critical nitrogen concentration determined to provide optimal growth. In our base simulation, nitrogen

stress follows different patterns compared to water stress for many regions and crops, although the global magnitudes in production reduction are similar (Figure 5.1). Maize production affected by nitrogen stress occurs mostly in the US Plains and Midwest. Nitrogen stress for wheat is distributed into all regions, while the effect on rice production is again lowest and mostly in southeast (SE) Asia. Nitrogen stress is more similar from year to year in the model as fertilizer application, which provides nitrogen to the soil, and inherent soil nitrogen content is the same. Total production change due to both water and nitrogen stress does not combine linearly. This illustrates the interconnected system simulated by the crop model. Overall, these environmental and management constraints greatly reduce global crop production from its unstressed potential. They are important to consider when analyzing the impact of PM and nitrogen deposition on crop production.

5.4. Results

5.4.1. Impact of Particulate Matter on Crop Growth

To simulate the effect of PM on crop production, we run pDSSAT as above with SW and DF input from GC-RT with and without PM. The differences in SW and DF due to PM over the pDSSAT growing season are shown in Figure 5.2. PM has a negative effect on SW everywhere and positive effect on DF. The largest influence of PM is over China for all three crops. The influence is especially noticeable for wheat, where a growing season over the winter corresponds

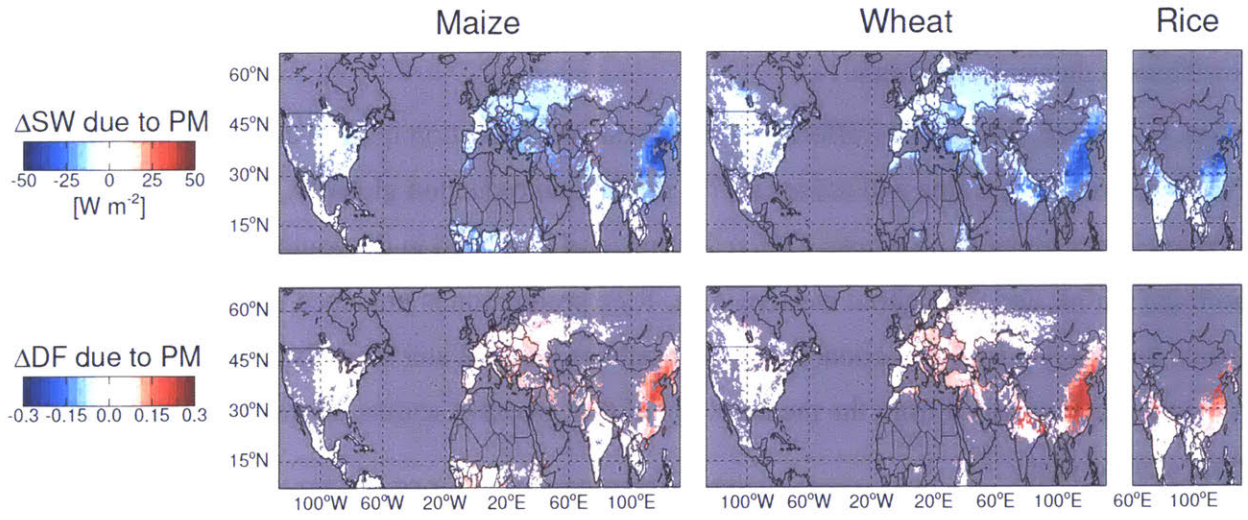

Figure 5.2. Mean change in daytime (SW > 0) (top row) downward SW radiation and (bottom row) DF of the SW radiation at the surface due to PM from GC-RT. For pDSSAT growing season ending in 2010 for (left column) maize, (middle column) wheat, and (right column) rice. Filtered for GAEZ base crop production greater than 0.01 Mg km ^{2}.

to higher PM concentrations. The difference between the simulations with and without PM (using max ΔRUE=100%) is the change in production due to PM, and this is shown in Figure 5.3. We perform this procedure first with no stress factors applied. Under no stress, global maize production increases by 1.7%, wheat increases by 17.1%, and rice increases by 6.2%. Wheat production in the India and China+SE Asia regions is most affected by PM, and the regional proportional change is show in Figure 5.4. For wheat and rice, pDSSAT reproduces well the proportional enhancement in crop production due to PM found in Chapter 4 using our offline relativistic methodology (Figure 5.4). This is true globally and within each region. The pDSSAT scenario with no stress is closely related to the offline analysis, which was unrestricted in production enhancement, so this good comparison is expected.

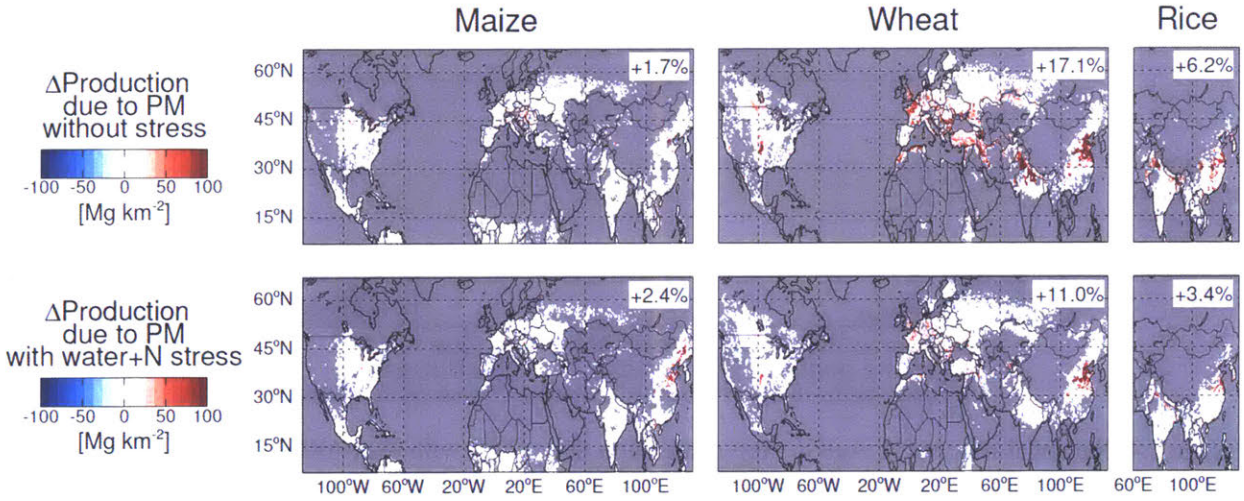

Figure 5.3. Change in pDSSAT crop production due to PM with max ΔRUE=100% with (top row) no stress and (bottom row) water and nitrogen stresses applied. For growing season ending in 2010 for (left column) maize, (middle column) wheat, and (right column) rice. Filtered for GAEZ base crop production greater than 0.01 Mg km^{-2}. Global relative production change shown in upper right.

The proportional increase in maize production due to PM simulated by the pDSSAT model is much lower than that from our offline analysis. This can be explained by a physiological restriction within the model which limits the maximum number of kernels per maize plant based on its genetic potential. Within pDSSAT, hybrid cultivars are limited to about 900 kernels per plant, while open-pollinated cultivars are limited to about 550 kernels per plant. In the scenario above with no stress, PM only causes a 1.3% increase in maize production over the US (Figure 5.5). For most locations in this domain, pDSSAT simulates the maximum maize production dictated by the kernel number both with and without PM. When we increase the limit by 500 kernels per plant, the maize production increases widely. Production without PM

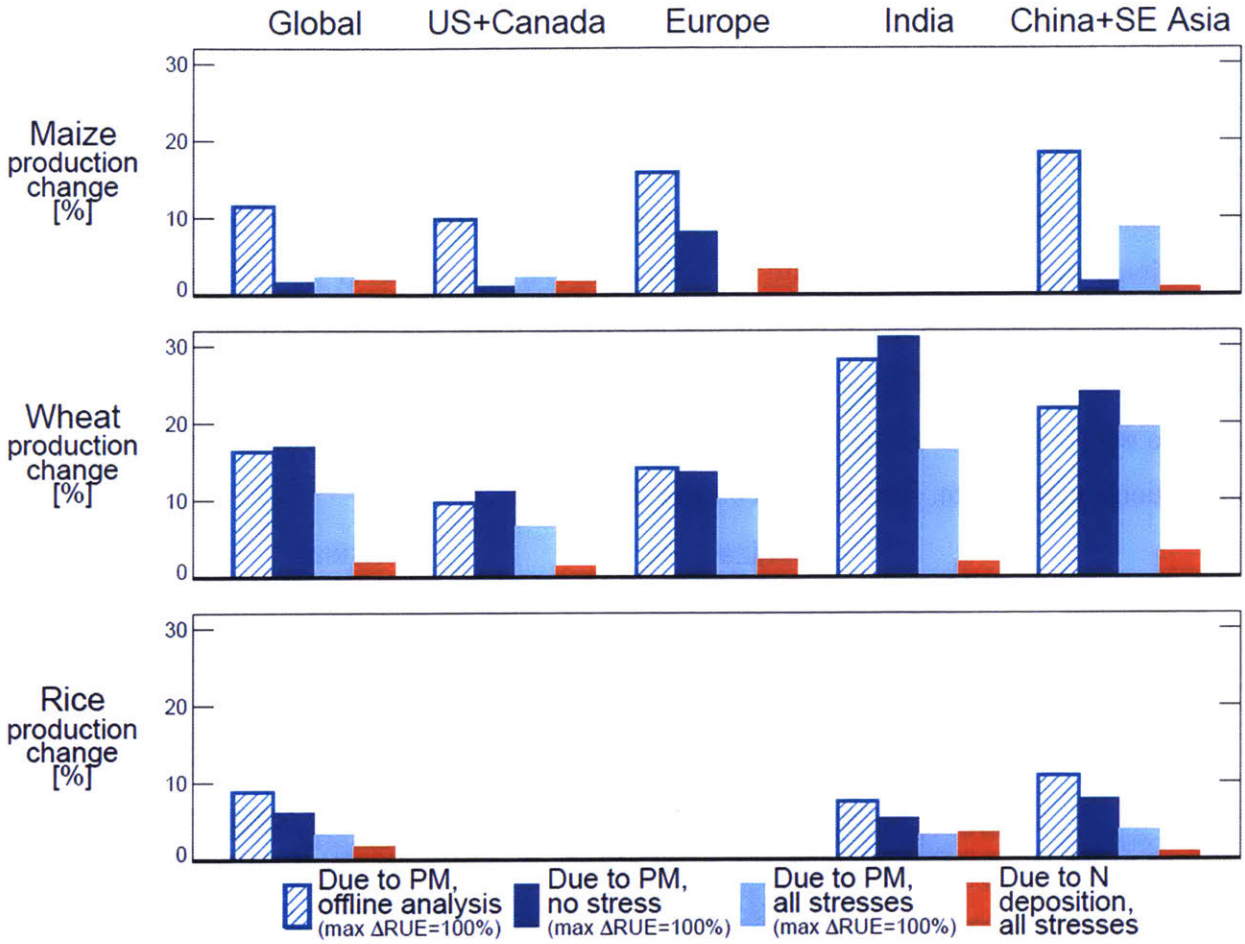

Figure 5.4. Regional relative change in crop production due to PM with max ΔRUE=100%: offline analysis from Chapter 4 (blue bars with hatching), pDSSAT simulation with no stress (dark blue bars), and pDSSAT simulation with water and nitrogen stresses (light blue bars). Change due to nitrogen deposition in orange. For growing season ending in 2010 for (top row) maize, (middle row) wheat, and (bottom row) rice. Regions with a base production lower than 5% of the global total are not shown.

increases by 25%, and production with PM increases by 34%. This results in an 8.8% increase in maize production due to PM over the US under no stress, which is similar to the approximately 10% increase found in the offline analysis. Including stress factors under the standard kernel restriction lowers the total production with and without PM, but allows for a larger proportional change due to PM in most areas (i.e., 1.3% global production increase without stress, but 2.4% with stresses) as more areas are producing below the production limit. When additional kernels are allowed with stresses turned on, production due to also PM increases, but to a lesser percentage compared to without stress (not shown).

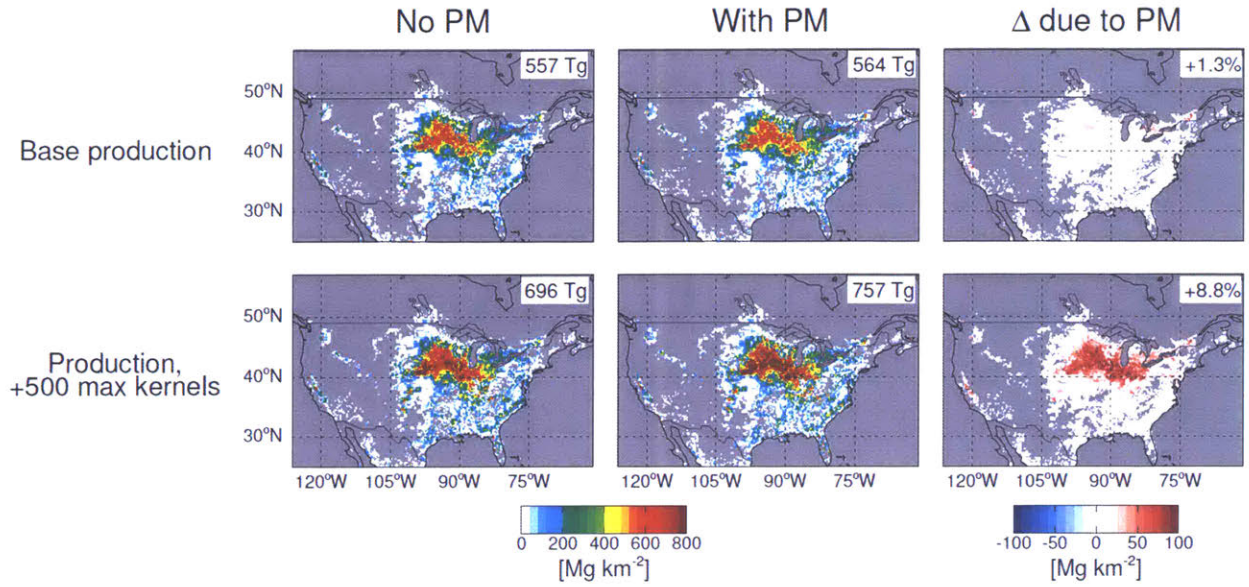

Figure 5.5. For (top row) pDSSAT base production and (bottom row) production with increased maximum kernels per plant: (left column) maize production with no PM, middle column) maize production with PM, and (right column) maize production due to PM. Filtered for GAEZ base crop production greater than 0.01 Mg km^{-2}. Global production (left and middle) or relative production change (right) shown in upper right.

To investigate the more realistic effect of PM on crop production, we impose both water and nitrogen stress on our pDSSAT simulations. The results for this scenario (Figures 5.3 and 5.4) indicate an 11% increase in global wheat production due to PM and a 3.4% increase in rice. These proportional enhancements are about one-third lower with stresses for wheat compared to without and about one-half for rice. While similar declines occur on a regional bases, these stresses have a larger impact on India for wheat, where nearly one-half of additional simulated wheat production is lost.

5.4.2. Impact of Nitrogen Deposition on Crop Growth

We run pDSSAT as above with NH_x and NO_y nitrogen deposition fluxes from GEOS-Chem and compare the results to the base simulation to quantify the impact of nitrogen deposition on crop production. No PM effects are considered. The total nitrogen deposition flux for each crop over the base scenario growing season is shown in Figure 5.6. There is high nitrogen deposition in India and China for all three crops, but especially wheat in China. The magnitude of nitrogen deposition from GEOS-Chem is generally lower than that applied as fertilizer. For example, two fertilizer applications for maize span roughly 50–100 kg ha^{-1} each over the US, Europe and China. We also plot the fraction of total nitrogen deposition made up of

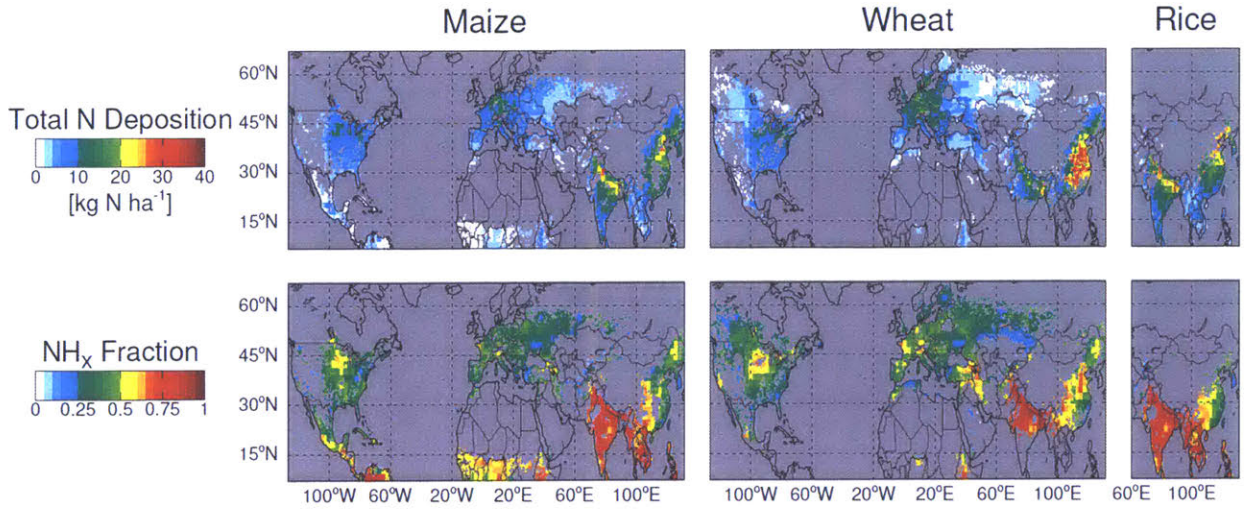

Figure 5.6. (top row) Total nitrogen deposition from GEOS-Chem and (bottom row) reduced nitrogen (NHx) fraction of this total. For pDSSAT growing season ending in 2010 for (left column) maize, (middle column) wheat, and (right column) rice. Filtered for GAEZ base crop production greater than 0.01 Mg km^{-2}.

NH_x. This fraction is slightly higher in agricultural areas of the US, Europe and China, where reduced species from agriculture mix with oxidized species from industry. In India, the NH_x fraction is very high, as there is little industrial emission to offset the large agricultural emissions.

With nitrogen stress only, crop production increases globally by 2.1% for maize, 2.6% for wheat and 1.9% for rice due to nitrogen deposition applied beginning 30 days before the planting date (Figure 5.7). The largest impact of nitrogen deposition is for wheat in China, which receives large amounts of nitrogen deposition and is highly sensitive to nitrogen stress (Figure 1). Nitrogen deposited to the surface accumulates in the soil throughout the growing season, moving quickly to lower levels of the soil profile. When fertilizer applied toward the beginning of the growing season runs out, this additional nitrogen reservoir from deposition allows for a mitigation of nitrogen stress and further plant growth. The fate of nitrogen in soil is not well constrained, and the length of time nitrogen is retained in the soil and useful to the plant is uncertain. When we apply nitrogen deposition to pDSSAT at the onset of the growing season, rather than 30 days prior to planting, we find that 18% of maize production enhancement due to nitrogen deposition is lost (20% loss for wheat and 23% loss for rice). Conversely, applying the deposition flux in the crop model earlier enhances the increase in crop production.

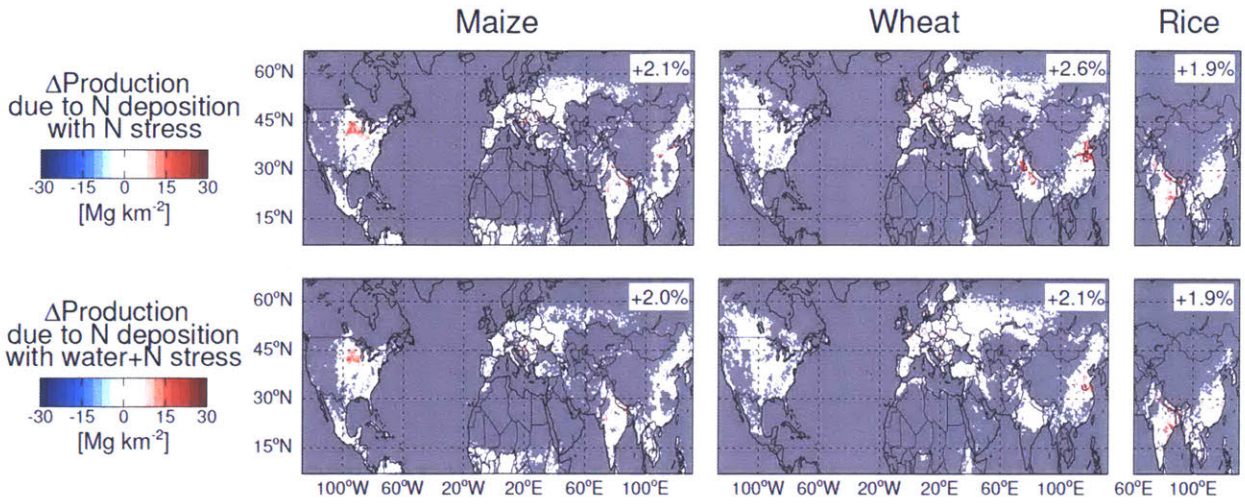

Figure 5.7. Change in pDSSAT crop production due nitrogen deposition with (top row) nitrogen stress and (bottom row) water and nitrogen stresses applied. For growing season ending in 2010 for (left column) maize, (middle column) wheat, and (right column) rice. Filtered for GAEZ base crop production greater than 0.01 Mg km^{-2}. Global relative production change shown in upper right.

The addition of water stress lowers the proportional enhancement of nitrogen deposition on crop production slightly, as shown in Figure 5.7. The largest change is for wheat, which is more water stressed than maize and rice in the model globally. The regional impacts of nitrogen deposition on crop production for the scenario with water and nitrogen stress are shown in Figure 5.4. In all cases except for rice in India, this nitrogen deposition effect is smaller proportionally than the enhancing effect of PM (disregarding the restrictive maize simulation in Europe). While we do apply reduced and oxidized nitrogen deposition (NH_x vs NO_y) separately in our simulations, this effort has little impact on the above results as soil nitrification quickly converts all soil NH_4^+ into NO_3^- in the pDSSAT model.

5.5. Conclusions

To our knowledge, this is the first effort to integrate atmospheric air quality inputs into the dynamic simulation of a crop model. Using realistic restrictions on water and nitrogen availability and physiological limitations we update estimates of the impact of PM on crop production made in Chapter 4 using the offline analysis. Maize production increases by only 2.4% due to PM (11.5% in Chapter 4) using the max ΔRUE = 100% relationship, while wheat increases by 11.0% (16.4%) and rice increases by 3.4% (8.9%). The positive effect of PM on crop production is lessened when considering realistic restrictions to crop growth, but remains

significant throughout the globe, especially in northern China, and will be important to consider for air quality policy decisions which may reduce PM and thereby reduce crop production.

The coupling with a crop model also provides an opportunity to explore the impact of atmospheric nitrogen deposition on crop production. We find that the impact of nitrogen deposition on crop production is low compared to the effect of PM. This may change in the future as ammonia emissions are expected to increase with future pressure on food production. Lower future NO_x emissions are likely due to regulatory efforts, which will reduce the nitrogen deposition flux. These reductions could also reduce PM in areas prone to ammonium nitrate formation.

The crop model responses to DF and nitrogen deposition examined in this study are uncertain. More work is needed, especially in the form of observations, to understand and evaluate these responses. It is critical to develop realistic crop models with reliable sensitivity to environmental factors to understand the pressure on future food security.

Chapter 6. Conclusions and Implications

In many areas of the globe, the current era of rising food demand and increasing industrialization is being accompanied by a deterioration in air quality and enhancement in agricultural activity. As both air quality and the food supply are vitally important to sustaining human enterprise, understanding their interactions is critical. The work in this thesis makes strides toward this goal. Here we highlight those advances, work left to be done, and additional interactions to explore.

In Chapter 2, we find that ammonia from agriculture is a major contributor to inorganic fine particulate matter ($PM_{2.5}$) under the appropriate chemical and meteorological conditions. Accurately quantifying agricultural ammonia emissions, the uncertainty of which outweighs that of other contributing factors, is critical to predicting the concentration of inorganic $PM_{2.5}$. In Chapter 3, the inclusion of variable ammonia emissions from agriculture does not improve the simulation of ammonia concentrations compared to newly available observations. These variable emissions also do not contribute much to the variability of inorganic $PM_{2.5}$ during the summer. Rather, inorganic $PM_{2.5}$ concentrations are more so driven by meteorology and acid-precursor emissions. This highlights the confounding nature of simultaneous ammonia emission and partitioning.

Motivated by the uncertainties in the above work, future work on understanding the role of ammonia in $PM_{2.5}$ formation would benefit greatly from quantitative observations of all relevant chemical species and meteorology at high spatial and high temporal resolution. Surface site density (in developed countries) is increasing, and higher quality satellite products with global coverage are being developed, but more is required. Co-located observations of multiple species over a long term period is key. An ideal study of the system would concentrate gas and particle observations in regions of either homogeneous landscape, such as large agricultural regions, or highly varying terrain, such as the transition from plain to mountainous areas. By combining these observations with a high resolution model we can better understand each individual region as well as address contrast between the regions. This method would increase confidence in the results as each region is isolated and analyzed individually, rather than combining limited data in many regions with differing environmental and chemical conditions. It

seems likely different processes are dominate in each area and teasing these out would contribute to our understanding of the ammonia and inorganic $PM_{2.5}$ system. Further, higher temporally resolved observations, both in situ and geostationary, will allow for a better understanding of the diurnal variations in this system and its role in controlling day and nighttime air quality.

Chapter 4 provides the first compete picture of the effects of air quality on global crop production, taking into account both total particulate matter (PM) and ozone. While uncertain, we find crop enhancement due to PM may contribute to a net positive air quality impact on crop production. Consequently, future air quality improvements may cause a decrease in crop production in some locations. Chapter 5 uses a crop model to constrain the PM impact on crop production to more realistic values under environmental stresses and physiological constraints, another first. We find that the effect of atmospheric nitrogen deposition on crop production is small, but highly sensitive to uncertain timing assumptions. Future work will characterize how different PM types impact the radiation reaching crops and how this might relate to air quality management strategies. We could also take a regional focus and use measurements or reported crop yields along with air quality measurements over multiple years to verify the simulated response demonstrated in our work.

Constraining plant physiological responses to particulate matter, ozone and nitrogen deposition impacts is also vital for further advancement in this area. Our work motivates future collaboration with plant and crop scientists who could investigate how air pollution impacts the biological processes affecting plant growth and crop production. This collaboration could come through modeling studies which take into account biological mechanisms at the leaf level or finer and propagate the air quality impacts through the system. Perhaps of greater impact, however, would be controlled experiments to better quantify the relationships between air quality parameters such as the diffuse fraction (DF) of shortwave radiation and plant growth, crop yield, or grain weight. In addition, studies that explore how ozone exposure and changes in radiation simultaneously impact crop production are needed. While laboratory conditions may not replicate real world conditions for resource and meteorological restrictions, they do provide better constrains on the varying impacts of PM on crops as it is not possible to control for PM in ambient conditions (only DF as a whole, which is influenced by clouds, can be measured).

Laboratory experiments with measurements of soil composition could also provide insight into the timing and transport of nitrogen deposition.

In the studies presented in this thesis, we have largely considered each direction in the agriculture and air quality system independently. In Chapters 2 and 3, agriculture impacts air quality, but this does not in turn affect agriculture, and vice versa for Chapter 4. Only in Chapter 5 do we begin to close the system loop by simulating the impact of nitrogen deposition, which is in part emitted by agricultural activities, on crop production. In reality, the interactions are more complicated, and additional exploration of these feedbacks could be insightful. As an exercise, we discuss one such situation and potential economic impacts below.

In the case of crop production, fertilizer is applied toward the beginning of the growing season based on the nitrogen content of the soil. If air quality regulations reduce nitrogen emissions and therefore the nitrogen deposition flux, the initial soil nitrogen content may be lower. The producer would then be required to purchase additional fertilizer to meet the needs of the crop. If the producer decides not to purchase additional fertilizer due to financial constraints, the crop production suffers, but emissions from volatilization during application is also reduced. This may further reduce nitrogen deposition downwind and so on. The net effect on air quality and crop production depends on the assumptions made for each individual component.

The same regulations above which restrict nitrogen emissions in order to improve air quality (and possibly increase producer fertilizer expense) may reduce crop production though a reduction in diffuse light caused by PM, as is possible in the future scenarios presented in Chapter 4. In this case, the regulators favor improving human health and visibility over the loss of food production and profitability for crop producers. This can be justified through a simple monetary comparison. The global total crop production losses for maize, wheat and rice due to total $PM_{2.5}$ reduction in RCP 4.5 is 27.7 Mt. This becomes a loss of approximately $7 billion in revenue using a mean producer price of $250 $tonne^{-1}$ [*FAOSTAT*, 2017]. Using a rough value of a statistical life set at $1 million [*Doucouliagos et al.*, 2012], this means only 7000 lives must be saved by $PM_{2.5}$ reduction to offset the loss of crop revenue. This figure is extremely small compared to the estimated 4 million premature deaths due to $PM_{2.5}$ pollution worldwide [*Cohen*

et al., 2017]. While this simple calculation could be refined by considering regional values and the costs of malnourishment, the overall cost of $PM_{2.5}$ on human health will substantially exceed the financial benefits associated with enhanced crop growth under any scenario.

Finally, we have not considered the role of climate in the interactions between agriculture and air quality. It is important to keep in mind that all of the mechanisms which are dependent on temperature described in this thesis, including chemical reactions and partitioning, emissions volatilization, and plant growth, take place in the context of increasing global temperatures. Higher temperatures favor increased ozone concentrations, decreased ammonium nitrate concentrations, increased ammonia emissions, and varying impacts on plants, depending on the plant type and location. Future work could bring the expected temperature changes (either generalized or from a climate model) into these systems to quantify the changes in the effects previously studied and discover any changes in the dominance of certain relationships. Changes in precipitation should also be examined as rainfall and moisture impact partitioning, deposition and plant growth in non-irrigated systems. The possibility of interesting feedbacks, which occur between greenhouse gas emissions from agriculture and the interactions between air quality and agriculture itself, should also be explored. However, there are large uncertainties associated with future climate scenarios, especially with regards to changes in precipitation. Therefore, in addition to the need for further observational constraints on how air quality and agriculture interact, we must also consider multiple scenarios to bracket how air quality, food production, and their interactions will be impacted by global change.

References

Adams, R. M., J. D. Glyer, S. L. Johnson, and B. A. McCarl (1989), A reassessment of the economic effects of ozone on U.S. agriculture, *JAPCA*, *39*(7), 960–968, doi:10.1080/08940630.1989.10466583.

Amos, H. M. et al. (2012), Gas-particle partitioning of atmospheric Hg(II) and its effect on global mercury deposition, *Atmos. Chem. Phys.*, 12(1), 591–603, doi:10.5194/acp-12-591-2012.

Ansari, A. S., and S. N. Pandis (1998), Response of inorganic PM to precursor concentrations, *Environ. Sci. Technol.*, 32(18), 2706–2714, doi:10.1021/es971130j.

Bahreini, R., et al. (2009), Organic aerosol formation in urban and industrial plumes near Houston and Dallas, Texas, *J. Geophys. Res.*, 114, D00F16, doi:10.1029/2008JD011493.

Beem, K. B., et al. (2010), Deposition of reactive nitrogen during the Rocky Mountain Airborne Nitrogen and Sulfur (RoMANS) study, *Environ. Pollut.*, 158(3), 862–872, doi:10.1016/j.envpol.2009.09.023.

Bond, T. C., E. Bhardwaj, R. Dong, R. Jogani, S. Jung, C. Roden, D. G. Streets, and N. M. Trautmann (2007), Historical emissions of black and organic carbon aerosol from energy-related combustion, 1850–2000, *Glob. Biogeochem. Cycles*, *21*(2), GB2018, doi:10.1029/2006GB002840.

Bouwman, A. F., D. S. Lee, W. A. H. Asman, F. J. Dentener, K. W. Van Der Hoek, and J. G. J. Olivier (1997), A global high-resolution emission inventory for ammonia, *Global Biogeochem. Cycles*, 11(4), 561, doi:10.1029/97GB02266.

Burnett, R. T., M. Smith-Doiron, D. Stieb, M. E. Raizenne, J. R. Brook, R. E. Dales, J. A. Leech, S. Cakmak, and D. Krewski (2001), Association between ozone and hospitalization for acute respiratory diseases in children less than 2 years of age, *Am. J. Epidemiol.*, *153*(5), 444–452, doi:10.1093/aje/153.5.444.

Canagaratna, M. R., et al. (2007), Chemical and microphysical characterization of ambient aerosols with the aerodyne aerosol mass spectrometer, *Mass Spectrom. Rev.*, 26(2), 185–222, doi:10.1002/mas.20115.

Chapin, F. S., P. A. Matson, and H. A. Mooney (2002), Principles of Terrestrial Ecosystems Ecology, Springer, New York.

Chen, D., Y. Wang, M. B. McElroy, K. He, R. M. Yantosca, and P. Le Sager (2009), Regional CO pollution and export in China simulated by the high-resolution nested-grid GEOS-Chem model, *Atmos. Chem. Phys.*, 9(11), 3825–3839, doi:10.5194/acp-9-3825-2009.

Chow, J. C., J. G. Watson, E. M. Fujita, Z. Lu, D. R. Lawson, and L. L. Ashbaugh (1994), Temporal and spatial variations of $PM_{2.5}$ and PM_{10} aerosol in the Southern California air quality study, *Atmos. Environ.*, 28(12), 2061–2080, doi:10.1016/1352-2310(94)90474-X.

Chow, J. C., J. G. Watson, Z. Lu, D. H. Lowenthal, C. A. Frazier, P. A. Solomon, R. H. Thuillier, and K.Magliano (1996), Descriptive analysis of $PM_{2.5}$ and PM_{10} at regionally representative locations during SJVAQS/AUSPEX, *Atmos. Environ.*, 30(12), 2079–2112, doi:10.1016/1352-2310(95)00402-5.

Chow, J. C., J. G. Watson, D. H. Lowenthal, R. T. Egami, P. A. Solomon, R. H. Thuillier, K. Magliano, and A. Ranzieri (1998), Spatial and temporal variations of particulate precursor gases and photochemical reaction products during SJVAQS/AUSPEX ozone episodes, *Atmos. Environ.*, 32(16), 2835–2844, doi:10.1016/S1352-2310(97)00449-4.

Cirino, G. G., R. A. F. Souza, D. K. Adams, and P. Artaxo (2014), The effect of atmospheric aerosol particles and clouds on net ecosystem exchange in the Amazon, *Atmos. Chem. Phys.*, *14*(13), 6523–6543, doi:10.5194/acp-14-6523-2014.

Clarisse, L., C. Clerbaux, F. Dentener, D. Hurtmans, and P.-F. Coheur (2009), Global ammonia distribution derived from infrared satellite observations, *Nat. Geosci.*, 2(7), 479–483, doi:10.1038/ngeo551.

Clarisse, L., M. W. Shephard, F. Dentener, D. Hurtmans, K. Cady-Pereira, F. Karagulian, M. Van Damme, C. Clerbaux, and P.-F. Coheur (2010), Satellite monitoring of ammonia: A case study of the San Joaquin Valley, *J. Geophys. Res.*, 115, D13302, doi:10.1029/2009JD013291.

Cohen, A. J. et al. (2017), Estimates and 25-year trends of the global burden of disease attributable to ambient air pollution: an analysis of data from the Global Burden of Diseases Study 2015, *The Lancet*, *389*(10082), 1907–1918, doi:10.1016/S0140-6736(17)30505-6.

Cooper, O. R., R.-S. Gao, D. Tarasick, T. Leblanc, and C. Sweeney (2012), Long-term ozone trends at rural ozone monitoring sites across the United States, 1990–2010, *J. Geophys. Res. Atmos.*, *117*(D22), D22307, doi:10.1029/2012JD018261.

Cox, P., A. Delao, A. Komorniczak, and R. Weller (2009), Air basin trends and forecasts—Criteria pollutants, Air Resources Board Almanac.

Day, D. E., X. Chen, K. A. Gebhart, C. M. Carrico, F. M. Schwandner, K. B. Benedict, B. A. Schichtel, and J. L. Collett Jr. (2012), Spatial and temporal variability of ammonia and other inorganic aerosol species, *Atmos. Environ.*, 61, 490–498, doi:10.1016/j.atmosenv.2012.06.045.

Dentener, F. J., and P. J. Crutzen (1994), A three-dimensional model of the global ammonia cycle, *J. Atmos. Chem.*, 19(4), 331–369, doi:10.1007/BF00694492.

Doucouliagos, C., T. D. Stanley, and M. Giles (2012), Are estimates of the value of a statistical life exaggerated?, *J. Health Econ.*, *31*(1), 197–206, doi:10.1016/j.jhealeco.2011.10.001.

Elliott, J., D. Kelly, J. Chryssanthacopoulos, M. Glotter, K. Jhunjhnuwala, N. Best, M. Wilde, and I. Foster (2014), The parallel system for integrating impact models and sectors (pSIMS), *Environ. Model. Softw.*, *62*, 509–516, doi:10.1016/j.envsoft.2014.04.008.

Ellis, R. A., D. J. Jacob, M. P. Sulprizio, L. Zhang, C. D. Holmes, B. A. Schichtel, T. Blett, E. Porter, L. H. Pardo, and J. A. Lynch (2013), Present and future nitrogen deposition to national parks in the United States: critical load exceedances, *Atmos. Chem. Phys.*, 13(17), 9083–9095, doi:10.5194/acp-13-9083-2013.

Erisman, J. W., A. Bleeker, J. Galloway, and M. S. Sutton (2007), Reduced nitrogen in ecology and the environment, *Environ. Pollut.*, 150(1), 140–149, doi:10.1016/j.envpol.2007.06.033.

Erisman, J. W., M. A. Sutton, J. Galloway, Z. Klimont, and W. Winiwarter (2008), How a century of ammonia synthesis changed the world, *Nat. Geosci.*, 1(10), 636–639, doi:10.1038/ngeo325.

Fairlie, T. D., D. J. Jacob, J. E. Dibb, B. Alexander, M. A. Avery, A. van Donkelaar, and L. Zhang (2010), Impact of mineral dust on nitrate, sulfate, and ozone in transpacific Asian pollution plumes, *Atmos. Chem. Phys.*, 10(8), 3999–4012, doi:10.5194/acp-10-3999-2010.

Fang, Y., A. M. Fiore, L. W. Horowitz, A. Gnanadesikan, I. Held, G. Chen, G. Vecchi, and H. Levy (2011), The impacts of changing transport and precipitation on pollutant distributions in a future climate, *J. Geophys. Res. Atmos.*, *116*(D18), D18303, doi:10.1029/2011JD015642.

FAOSTAT (2017), FAOSTAT,

Faulkner, W. B., and B. W. Shaw (2008), Review of ammonia emission factors for United States animal agriculture, *Atmos. Environ.*, 42(27), 6567–6574, doi:10.1016/j.atmosenv.2008.04.021.

Fountoukis, C., and A. Nenes (2007), ISORROPIA II: A computationally efficient thermodynamic equilibrium model for K^+–Ca^{2+}–Mg^{2+}–NH_4^+–Na^+–SO_4^{2-}–NO_3^-–Cl^-–H_2O aerosols, *Atmos. Chem. Phys.*, 7(17), 4639–4659, doi:10.5194/acp-7-4639-2007.

Galloway, J. N., and E. B. Cowling (2002), Reactive nitrogen and the world: 200 years of change, *AMBIO J. Hum. Environ.*, 31(2), 64–71, doi:10.1579/0044-7447-31.2.64.

Goebes, M. D., R. Strader, and C. Davidson (2003), An ammonia emission inventory for fertilizer application in the United States, *Atmos. Environ.*, 37(18), 2539–2550, doi:10.1016/S1352-2310(03)00129-8.

Goulding, K. W. T., N. J. Bailey, N. J. Bradbury, P. Hargreaves, M. Howe, D. V. Murphy, P. R. Poulton, and T. W. Willison (1998), Nitrogen deposition and its contribution to nitrogen cycling and associated soil processes, *New Phytol.*, *139*(1), 49–58.

Greenwald, R., M. H. Bergin, J. Xu, D. Cohan, G. Hoogenboom, and W. L. Chameides (2006), The influence of aerosols on crop production: A study using the CERES crop model, *Agric. Syst.*, *89*(2–3), 390–413, doi:10.1016/j.agsy.2005.10.004.

Guenther, A. B., X. Jiang, C. L. Heald, T. Sakulyanontvittaya, T. Duhl, L. K. Emmons, and X. Wang (2012), The Model of Emissions of Gases and Aerosols from Nature version 2.1 (MEGAN2.1): an extended and updated framework for modeling biogenic emissions, *Geosci Model Dev Discuss*, *5*(2), 1503–1560, doi:10.5194/gmdd-5-1503-2012.

Guo, S. et al. (2014), Elucidating severe urban haze formation in China, *Proc. Natl. Acad. Sci.*, *111*(49), 17373–17378, doi:10.1073/pnas.1419604111.

Gyldenkærne, S., C. Ambelas Skjøth, O. Hertel, and T. Ellermann (2005), A dynamical ammonia emission parameterization for use in air pollution models, *J. Geophys. Res. Atmos.*, 110(D7), D07108, doi:10.1029/2004JD005459.

Hall, J. V., V. Brajer, and F. W. Lurmann (2008), Measuring the gains from improved air quality in the San Joaquin Valley, *J. Environ. Manage.*, 88(4), 1003–1015, doi:10.1016/j.jenvman.2007.05.002.

Hand, J. L., B. A. Schichtel, M. Pitchford, W. C. Malm, and N. H. Frank (2012), Seasonal composition of remote and urban fine particulate matter in the United States, *J. Geophys. Res.*, 117, D05209, doi:10.1029/2011JD017122.

Heald, C. L., et al. (2012), Atmospheric ammonia and particulate inorganic nitrogen over the United States, *Atmos. Chem. Phys.*, 12(21), 10,295–10,312, doi:10.5194/acp-12-10295-2012.

Heald, C. L., D. A. Ridley, J. H. Kroll, S. R. H. Barrett, K. E. Cady-Pereira, M. J. Alvarado, and C. D. Holmes (2014), Contrasting the direct radiative effect and direct radiative forcing of aerosols, *Atmos. Chem. Phys.*, *14*(11), 5513–5527, doi:10.5194/acp-14-5513-2014.

Holland, E. A., F. J. Dentener, B. H. Braswell, and J. M. Sulzman (1999), Contemporary and pre-industrial global reactive nitrogen budgets, *Biogeochemistry*, 46(1), 7–43, doi:10.1007/BF01007572.

Holt, J., N. E. Selin, and S. Solomon (2015), Changes in inorganic fine particulate matter sensitivities to precursors due to large-scale US emissions reductions, *Environ. Sci. Technol.*, 49(8), 4834–4841, doi:10.1021/acs.est.5b00008.

Horton, D. E., C. B. Skinner, D. Singh, and N. S. Diffenbaugh (2014), Occurrence and persistence of future atmospheric stagnation events, *Nat. Clim. Change*, *4*(8), 698–703, doi:10.1038/nclimate2272.

Hristov, A. N., M. Hanigan, A. Cole, R. Todd, T. A. McAllister, P. M. Ndegwa, and A. Rotz (2011), Review: Ammonia emissions from dairy farms and beef feedlots, *Can. J. Anim. Sci.*, 91(1), 1–35, doi:10.4141/CJAS10034.

Hu, L. et al. (2015a), Emissions of C6–C8 aromatic compounds in the United States: Constraints from tall tower and aircraft measurements, *J. Geophys. Res. Atmos.*, *120*(2), 2014JD022627, doi:10.1002/2014JD022627.

Hu, L., D. B. Millet, M. Baasandorj, T. J. Griffis, P. Turner, D. Helmig, A. J. Curtis, and J. Hueber (2015b), Isoprene emissions and impacts over an ecological transition region in the U.S. Upper Midwest inferred from tall tower measurements, *J. Geophys. Res. Atmos.*, *120*(8), 2014JD022732, doi:10.1002/2014JD022732.

Hudman, R. C., N. E. Moore, A. K. Mebust, R. V. Martin, A. R. Russell, L. C. Valin, and R. C. Cohen (2012), Steps towards a mechanistic model of global soil nitric oxide emissions: implementation and space based-constraints, *Atmos. Chem. Phys.*, 12(16), 7779–7795, doi:10.5194/acp-12-7779-2012.

Iacono, M. J., J. S. Delamere, E. J. Mlawer, M. W. Shephard, S. A. Clough, and W. D. Collins (2008), Radiative forcing by long-lived greenhouse gases: Calculations with the AER radiative transfer models, *J. Geophys. Res. Atmos.*, *113*(D13), D13103, doi:10.1029/2008JD009944.

IPCC (2007), Climate change 2007: The physical science basis, in Contribution of Working Group I to the Fourth Assessment Report of the Intergovernmental Panel on Climate Change, edited by S. Solomon et al., 996 pp., Cambridge Univ. Press, Cambridge, U. K., and New York.

IPCC (2013), Climate change 2013: The physical science basis. Working Group I contribution to the Fifth Assessment Report of the Intergovernmental Panel on Climate Change, edited by T. F. Stocker et al., 1535 pp., Cambridge Univ. Press, Cambridge, U. K., and New York.

Jacob, D. J., J. W. Munger, J. M. Waldman, and M. R. Hoffmann (1986), The H_2SO_4–HNO_3–NH_3 system at high humidities and in fogs 1. Spatial and temporal patterns in the San Joaquin Valley of California, *J. Geophys. Res.*, 91(D1), 1073–1088, doi:10.1029/JD091iD01p01073.

Jaeglé, L., P. K. Quinn, T. S. Bates, B. Alexander, and J.-T. Lin (2011), Global distribution of sea salt aerosols: new constraints from in situ and remote sensing observations, *Atmos. Chem. Phys.*, *11*(7), 3137–3157, doi:10.5194/acp-11-3137-2011.

Jayne, J. T., D. C. Leard, X. Zhang, P. Davidovits, K. A. Smith, C. E. Kolb, and D. R. Worsnop (2000), Development of an aerosol mass spectrometer for size and composition analysis

of submicron particles, *Aerosol Sci. Technol.*, 33(1–2), 49–70, doi:10.1080/027868200410840.

Jimenez, J. L., et al. (2003), Ambient aerosol sampling using the Aerodyne Aerosol Mass Spectrometer, *J. Geophys. Res.*, 108(D7), 8425, doi:10.1029/2001JD001213.

Jones, J. W., G. Hoogenboom, C. H. Porter, K. J. Boote, W. D. Batchelor, L. A. Hunt, P. W. Wilkens, U. Singh, A. J. Gijsman, and J. T. Ritchie (2003), The DSSAT cropping system model, *Eur. J. Agron.*, *18*(3–4), 235–265, doi:10.1016/S1161-0301(02)00107-7.

Kaneyasu, N., H. Yoshikado, T. Mizuno, K. Sakamoto, and M. Soufuku (1999), Chemical forms and sources of extremely high nitrate and chloride in winter aerosol pollution in the Kanto Plain of Japan, *Atmos. Environ.*, 33(11), 1745–1756, doi:10.1016/S1352-2310(98)00396-3.

Kanniah, K. D., J. Beringer, P. North, and L. Hutley (2012), Control of atmospheric particles on diffuse radiation and terrestrial plant productivity A review, *Prog. Phys. Geogr.*, *36*(2), 209–237, doi:10.1177/0309133311434244.

Kim, S.-W., et al. (2011), Evaluations of NO_x and highly reactive VOC emission inventories in Texas and their implications for ozone plume simulations during the Texas Air Quality Study 2006, *Atmos. Chem. Phys.*, 11(22), 11,361–11,386, doi:10.5194/acp-11-11361-2011.

Kuhns, H., E. M. Knipping, and J. M. Vukovich (2005), Development of a United States-Mexico emissions inventory for the Big Bend Regional Aerosol and Visibility Observational (BRAVO) study, *J. Air Waste Manag. Assoc. 1995*, *55*(5), 677–692.

Lapina, K., D. K. Henze, J. B. Milford, and K. Travis (2016), Impacts of foreign, domestic, and state-level emissions on ozone-induced vegetation loss in the United States, *Environ. Sci. Technol.*, *50*(2), 806–813, doi:10.1021/acs.est.5b04887.

Leibensperger, E. M., L. J. Mickley, D. J. Jacob, W.-T. Chen, J. H. Seinfeld, A. Nenes, P. J. Adams, D. G. Streets, N. Kumar, and D. Rind (2012), Climatic effects of 1950–2050 changes in US anthropogenic aerosols – Part 1: Aerosol trends and radiative forcing, *Atmos. Chem. Phys.*, *12*(7), 3333–3348, doi:10.5194/acp-12-3333-2012.

Lelieveld, J., J. S. Evans, M. Fnais, D. Giannadaki, and A. Pozzer (2015), The contribution of outdoor air pollution sources to premature mortality on a global scale, *Nature*, 525(7569), 367–371, doi:10.1038/nature15371.

Lemieux, P. M., C. C. Lutes, and D. A. Santoianni (2004), Emissions of organic air toxics from open burning: a comprehensive review, *Prog. Energy Combust. Sci.*, *30*(1), 1–32, doi:10.1016/j.pecs.2003.08.001.

Lesser, V. M., J. O. Rawlings, S. E. Spruill, and M. C. Somerville (1990), Ozone effects on agricultural crops: statistical methodologies and estimated dose-response relationships, *Crop Sci.*, *30*(1), 148–155, doi:10.2135/cropsci1990.0011183X003000010033x.

Levy, H., L. W. Horowitz, M. D. Schwarzkopf, Y. Ming, J.-C. Golaz, V. Naik, and V. Ramaswamy (2013), The roles of aerosol direct and indirect effects in past and future climate change, *J. Geophys. Res. Atmos.*, *118*(10), 4521–4532, doi:10.1002/jgrd.50192.

Li, M. et al. (2014), Mapping Asian anthropogenic emissions of non-methane volatile organic compounds to multiple chemical mechanisms, *Atmos. Chem. Phys.*, *14*(11), 5617–5638, doi:10.5194/acp-14-5617-2014.

Liu, H., D. J. Jacob, I. Bey, and R. M. Yantosca (2001), Constraints from ^{210}Pb and ^{7}Be on wet deposition and transport in a global three-dimensional chemical tracer model driven by assimilated meteorological fields, *J. Geophys. Res.*, 106(D11), 12,109–12,128, doi:10.1029/2000JD900839.

Liu, P. S. K., R. Deng, K. A. Smith, L. R. Williams, J. T. Jayne, M. R. Canagaratna, K. Moore, T. B. Onasch, D. R. Worsnop, and T. Deshler (2007), Transmission efficiency of an aerodynamic focusing lens system: Comparison of model calculations and laboratory measurements for the aerodyne aerosol mass spectrometer, *Aerosol Sci. Technol.*, 41(8), 721–733, doi:10.1080/02786820701422278.

Lloret, J., and I. Valiela (2016), Unprecedented decrease in deposition of nitrogen oxides over North America: the relative effects of emission controls and prevailing air-mass trajectories, *Biogeochemistry*, 129(1–2), 165–180, doi:10.1007/s10533-016-0225-5.

Lombardozzi, D., J. P. Sparks, G. Bonan, and S. Levis (2012), Ozone exposure causes a decoupling of conductance and photosynthesis: implications for the Ball-Berry stomatal conductance model, *Oecologia*, *169*(3), 651–659, doi:10.1007/s00442-011-2242-3.

Mao, J., F. Paulot, D. J. Jacob, R. C. Cohen, J. D. Crounse, P. O. Wennberg, C. A. Keller, R. C. Hudman, M. P. Barkley, and L. W. Horowitz (2013), Ozone and organic nitrates over the eastern United States: sensitivity to isoprene chemistry, *J. Geophys. Res. Atmos.*, *118*(19), 2013JD020231, doi:10.1002/jgrd.50817.

Mari, C., D. J. Jacob, and P. Bechtold (2000), Transport and scavenging of soluble gases in a deep convective cloud, *J. Geophys. Res.*, 105(D17), 22,255–22,267, doi:10.1029/2000JD900211.

Massad, R.-S., E. Nemitz, and M. A. Sutton (2010), Review and parameterisation of bi-directional ammonia exchange between vegetation and the atmosphere, *Atmos. Chem. Phys.*, 10(21), 10359–10386, doi:10.5194/acp-10-10359-2010.

Matsui, T., A. Beltrán-Przekurat, D. Niyogi, R. A. Pielke, and M. Coughenour (2008), Aerosol light scattering effect on terrestrial plant productivity and energy fluxes over the eastern United States, *J. Geophys. Res. Atmos.*, *113*(D14), D14S14, doi:10.1029/2007JD009658.

Mercado, L. M., N. Bellouin, S. Sitch, O. Boucher, C. Huntingford, M. Wild, and P. M. Cox (2009), Impact of changes in diffuse radiation on the global land carbon sink, *Nature*, *458*(7241), 1014–1017, doi:10.1038/nature07949.

Mills, G., A. Buse, B. Gimeno, V. Bermejo, M. Holland, L. Emberson, and H. Pleijel (2007), A synthesis of AOT40-based response functions and critical levels of ozone for agricultural and horticultural crops, *Atmos. Environ.*, *41*(12), 2630–2643, doi:10.1016/j.atmosenv.2006.11.016.

Mozurkewich, M. (1993), The dissociation constant of ammonium nitrate and its dependence on temperature, relative humidity and particle size, *Atmos. Environ. A-Gen.*, 27(2), 261–270, doi:10.1016/0960-1686(93)90356-4.

Murray, L. T., D. J. Jacob, J. A. Logan, R. C. Hudman, and W. J. Koshak (2012), Optimized regional and interannual variability of lightning in a global chemical transport model constrained by LIS/OTD satellite data, *J. Geophys. Res.*, 117, D20307, doi:10.1029/2012JD017934.

Myriokefalitakis, S., K. Tsigaridis, N. Mihalopoulos, J. Sciare, A. Nenes, K. Kawamura, A. Segers, and M. Kanakidou (2011), In-cloud oxalate formation in the global troposphere:

A 3-D modeling study, *Atmos. Chem. Phys.*, 11(12), 5761–5782, doi:10.5194/acp-11-5761-2011.

Neuman, J. A., et al. (2002), Fast-response airborne in situ measurements of HNO_3 during the Texas 2000 Air Quality Study, *J. Geophys. Res.*, 107(D20), 4436, doi:10.1029/2001JD001437.

Neuman, J. A., et al. (2003), Variability in ammonium nitrate formation and nitric acid depletion with altitude and location over California, *J. Geophys. Res.*, 108(D17), 4557, doi:10.1029/2003JD003616.

Nowak, J.B., J.A. Neuman, K.Kozai, L.G.Huey, D. J. Tanner, J. S.Holloway, T.B.Ryerson,G. J. Frost, S.A.McKeen, and F.C. Fehsenfeld (2007), A chemical ionization mass spectrometry technique for airborne measurements of ammonia, *J. Geophys. Res.*, 112, D10S02, doi:10.1029/2006JD007589.

Nowak, J. B., J. A. Neuman, R. Bahreini, C. A. Brock, A. M. Middlebrook, A. G. Wollny, J. S. Holloway, J. Peischl, T. B. Ryerson, and F. C. Fehsenfeld (2010), Airborne observations of ammonia and ammonium nitrate formation over Houston, Texas, *J. Geophys. Res.*, 115(D22), doi:10.1029/2010JD014195.

Nowak, J. B., J. A. Neuman, R. Bahreini, A. M. Middlebrook, J. S. Holloway, S. A. McKeen, D. D. Parrish, T. B. Ryerson, and M. Trainer (2012), Ammonia sources in the California South Coast Air Basin and their impact on ammonium nitrate formation, *Geophys. Res. Lett.*, 39, L07804, doi:10.1029/2012GL051197.

OECD (2012), *OECD Environmental Outlook to 2050*, Organisation for Economic Co-operation and Development, Paris.

Park, R. J., D. J. Jacob, M. Chin, and R. V. Martin (2003), Sources of carbonaceous aerosols over the United States and implications for natural visibility, *J. Geophys. Res. Atmos.*, *108*(D12), 4355, doi:10.1029/2002JD003190.

Park, R. J., D. J. Jacob, B. D. Field, R. M. Yantosca, and M. Chin (2004), Natural and transboundary pollution influences on sulfate-nitrate-ammonium aerosols in the United States: Implications for policy, *J. Geophys. Res.*, 109, D15204, doi:10.1029/2003JD004473.

Paulot, F., and D. J. Jacob (2014), Hidden cost of U.S. agricultural exports: particulate matter from ammonia emissions, *Environ. Sci. Technol.*, 48(2), 903–908, doi:10.1021/es4034793.

Paulot, F., D. J. Jacob, R. W. Pinder, J. O. Bash, K. Travis, and D. K. Henze (2014), Ammonia emissions in the United States, European Union, and China derived by high-resolution inversion of ammonium wet deposition data: Interpretation with a new agricultural emissions inventory (MASAGE_NH3), *J. Geophys. Res. Atmos.*, 119(7), 4343–4364, doi:10.1002/2013JD021130.

Paulot, F., P. Ginoux, W. F. Cooke, L. J. Donner, S. Fan, M.-Y. Lin, J. Mao, V. Naik, and L. W. Horowitz (2016), Sensitivity of nitrate aerosols to ammonia emissions and to nitrate chemistry: implications for present and future nitrate optical depth, *Atmos. Chem. Phys.*, 16(3), 1459–1477, doi:10.5194/acp-16-1459-2016.

Pawar, H., S. Garg, V. Kumar, H. Sachan, R. Arya, C. Sarkar, B. P. Chandra, and B. Sinha (2015), Quantifying the contribution of long-range transport to particulate matter (PM)

mass loadings at a suburban site in the north-western Indo-Gangetic Plain (NW-IGP), *Atmos. Chem. Phys.*, *15*(16), 9501–9520, doi:10.5194/acp-15-9501-2015.

Peel, D. (2012), Current Economic Climate of the Beef Cattle Industry, Cornbelt Cow-Calf Conf.

Pinder, R. W., R. Strader, C. I. Davidson, and P. J. Adams (2004), A temporally and spatially resolved ammonia emission inventory for dairy cows in the United States, *Atmos. Environ.*, 38(23), 3747–3756, doi:10.1016/j.atmosenv.2004.04.008.

Pinder, R. W., P. J. Adams, S. N. Pandis, and A. B. Gilliland (2006a), Temporally resolved ammonia emission inventories: Current estimates, evaluation tools, and measurement needs, *J. Geophys. Res.*, 111, D16310, doi:10.1029/2005JD006603.

Pinder, R. W., P. J. Adams, and S. N. Pandis (2006b), Ammonia emission controls as a cost-effective strategy for reducing atmospheric particulate matter in the Eastern United States, *Env. Sci. Technol.*, 41(2), 380–386, doi:10.1021/es060379a.

Pinder, R. W., K. W. Appel, and R. L. Dennis (2011), Trends in atmospheric reactive nitrogen for the Eastern United States, *Environ. Pollut.*, 159(10), 3138–3141, doi:10.1016/j.envpol.2011.04.042.

Pleim, J. E., J. O. Bash, J. T. Walker, and E. J. Cooter (2013), Development and evaluation of an ammonia bidirectional flux parameterization for air quality models, *J. Geophys. Res. Atmos.*, 118(9), 3794–3806, doi:10.1002/jgrd.50262.

Pollack, I. B., B. M. Lerner, and T. B. Ryerson (2010), Evaluation of ultraviolet light-emitting diodes for detection of atmospheric NO_2 by photolysis-chemiluminescence, *J. Atmos. Chem.*, 65(2–3), 111–125, doi:10.1007/s10874-011-9184-3.

Pope, C. A., M. Ezzati, and D. W. Dockery (2009), Fine-particulate air pollution and life expectancy in the United States, *New Engl. J. Med.*, 360(4), 376–386, doi:10.1056/NEJMsa0805646.

Portmann, F. T., S. Siebert, and P. Döll (2010), MIRCA2000—Global monthly irrigated and rainfed crop areas around the year 2000: a new high-resolution data set for agricultural and hydrological modeling, *Glob. Biogeochem. Cycles*, *24*(1), GB1011, doi:10.1029/2008GB003435.

Puchalski, M. A., M. E. Sather, J. T. Walker, C. M. B. Lehmann, D. A. Gay, J. Mathew, and W. P. Robarge (2011), Passive ammonia monitoring in the United States: Comparing three different sampling devices, *J. Environ. Monit.*, 13(11), 3156–3167, doi:10.1039/C1EM10553A.

Pye, H. O. T., H. Liao, S. Wu, L. J. Mickley, D. J. Jacob, D. K. Henze, and J. H. Seinfeld (2009), Effect of changes in climate and emissions on future sulfate-nitrate-ammonium aerosol levels in the United States, *J. Geophys. Res.*, 114, D01205, doi:10.1029/2008JD010701.

Qi, M., K. Lin, X. Li, T. W. Sammis, D. R. Miller, and J. Wang (2015), Particulate matter contributions from agricultural tilling operations in an irrigated desert region, *PLOS ONE*, *10*(9), e0138577, doi:10.1371/journal.pone.0138577.

Rastigejev, Y., R. Park, M. P. Brenner, and D. J. Jacob (2010), Resolving intercontinental pollution plumes in global models of atmospheric transport, *J. Geophys. Res.*, 115, D02302, doi:10.1029/2009JD012568.

Rienecker, M. M. et al. (2011), MERRA: NASA's Modern-Era Retrospective Analysis for Research and Applications, *J. Clim.*, 24(14), 3624–3648, doi:10.1175/JCLI-D-11-00015.1.

Ritchie, J.T., U. Singh, D.C. Godwin, and W.T. Bowen (1998), Cereal growth, development and yield. In: Tsuji, G.Y., Hoogenboom, G., Thornton, P.K. (Eds.), Understanding Options for Agricultural Production. Kluwer Academic Publishers, Dordrecht, Netherlands.

Rochette, P., R. L. Desjardins, E. Pattey, and R. Lessard (1996), Instantaneous measurement of radiation and water use efficiencies of a maize crop, *Agron. J.*, *88*(4), 627, doi:10.2134/agronj1996.00021962008800040022x.

Rosenzweig, C. et al. (2013), The Agricultural Model Intercomparison and Improvement Project (AgMIP): protocols and pilot studies, *Agric. For. Meteorol.*, *170*, 166–182, doi:10.1016/j.agrformet.2012.09.011.

Rosenzweig, C. et al. (2014), Assessing agricultural risks of climate change in the 21st century in a global gridded crop model intercomparison, *Proc. Natl. Acad. Sci.*, *111*(9), 3268–3273, doi:10.1073/pnas.1222463110.

Ruane, A. C., R. Goldberg, and J. Chryssanthacopoulos (2015), Climate forcing datasets for agricultural modeling: merged products for gap-filling and historical climate series estimation, *Agric. For. Meteorol.*, *200*, 233–248, doi:10.1016/j.agrformet.2014.09.016.

Russell, A. G., G. J. McRae, and G. R. Cass (1983), Mathematical modeling of the formation and transport of ammonium nitrate aerosol, *Atmos. Environ.*, 17(5), 949–964, doi:10.1016/0004-6981(83)90247-0.

Russell, A. G., and G. R. Cass (1986), Verification of a mathematical model for aerosol nitrate and nitric acid formation and its use for control measure evaluation, *Atmos. Environ.*, 20(10), 2011–2025, doi:10.1016/0004-6981(86)90342-2.

Russell, A. R., L. C. Valin, and R. C. Cohen (2012), Trends in OMI NO_2 observations over the United States: effects of emission control technology and the economic recession, *Atmos. Chem. Phys.*, 12(24), 12,197–12,209, doi:10.5194/acp-12-12197-2012.

Ryerson, T. B., et al. (1998), Emissions lifetimes and ozone formation in power plant plumes, *J. Geophys. Res.*, 103(D17), 22,569–22,583, doi:10.1029/98JD01620.

Ryerson, T. B., E. J. Williams, and F. C. Fehsenfeld (2000), An efficient photolysis system for fast-response NO_2 measurements, *J. Geophys. Res.*, 105(D21), 26,447–26,461, doi:10.1029/2000JD900389.

Ryerson, T. B., et al. (2013), The 2010 California Research at the Nexus of Air Quality and Climate Change (CalNex) field study, *J. Geophys. Res. Atmos.*, 118, 5830–5866, doi:10.1002/jgrd.50331.

Sacks, W. J., D. Deryng, J. A. Foley, and N. Ramankutty (2010), Crop planting dates: an analysis of global patterns, *Glob. Ecol. Biogeogr.*, *19*(5), 607–620, doi:10.1111/j.1466-8238.2010.00551.x.

Schiferl, L. D. and C. L. Heald, The impact of ozone and particulate matter air pollution on global crop production, in prep.

Schiferl, L. D., C. L. Heald, J. B. Nowak, J. S. Holloway, J. A. Neuman, R. Bahreini, I. B. Pollack, T. B. Ryerson, C. Wiedinmyer, and J. G. Murphy (2014), An investigation of ammonia and inorganic particulate matter in California during the CalNex campaign, *J. Geophys. Res. Atmos.*, 119(4), 2013JD020765, doi:10.1002/2013JD020765.

Schiferl, L. D. et al. (2016), Interannual variability of ammonia concentrations over the United States: sources and implications, *Atmos. Chem. Phys.*, 16(18), 12305–12328, doi:10.5194/acp-16-12305-2016.

Seinfeld, J. H., and S. N. Pandis (2006), Atmospheric Chemistry and Physics - From Air Pollution to Climate Change, 2nd ed., John Wiley, Hoboken, N. J.

Shangguan, W., Y. Dai, Q. Duan, B. Liu, and H. Yuan (2014), A global soil data set for earth system modeling, *J. Adv. Model. Earth Syst.*, *6*(1), 249–263, doi:10.1002/2013MS000293.

Shephard, M. W., and K. E. Cady-Pereira (2015), Cross-track Infrared Sounder (CrIS) satellite observations of tropospheric ammonia, *Atmos. Meas. Tech.*, 8(3), 1323–1336, doi:10.5194/amt-8-1323-2015.

Shephard, M. W. et al. (2011), TES ammonia retrieval strategy and global observations of the spatial and seasonal variability of ammonia, *Atmos. Chem. Phys.*, 11(20), 10743–10763, doi:10.5194/acp-11-10743-2011.

Sherwen, T. et al. (2016), Global impacts of tropospheric halogens (Cl, Br, I) on oxidants and composition in GEOS-Chem, *Atmos. Chem. Phys.*, *16*(18), 12239–12271, doi:10.5194/acp-16-12239-2016.

Shindell, D., G. Faluvegi, M. Walsh, S. C. Anenberg, R. Van Dingenen, N. Z. Muller, J. Austin, D. Koch, and G. Milly (2011), Climate, health, agricultural and economic impacts of tighter vehicle-emission standards, *Nat. Clim. Change*, *1*(1), 59–66, doi:10.1038/nclimate1066.

Sinclair, T. R., T. Shiraiwa, and G. L. Hammer (1992), Variation in crop radiation use efficiency with increased diffuse radiation, *Crop Sci.*, *32*(5), 1281, doi:10.2135/cropsci1992.0011183X003200050043x.

Sinha, B., K. Singh Sangwan, Y. Maurya, V. Kumar, C. Sarkar, B. P. Chandra, and V. Sinha (2015), Assessment of crop yield losses in Punjab and Haryana using 2 years of continuous in situ ozone measurements, *Atmos. Chem. Phys.*, *15*(16), 9555–9576, doi:10.5194/acp-15-9555-2015.

Sitch, S., P. M. Cox, W. J. Collins, and C. Huntingford (2007), Indirect radiative forcing of climate change through ozone effects on the land-carbon sink, *Nature*, *448*(7155), 791–794, doi:10.1038/nature06059.

Søgaard, H. T., S. G. Sommer, N. J. Hutchings, J. F. M. Huijsmans, D. W. Bussink, and F. Nicholson (2002), Ammonia volatilization from field-applied animal slurry—the ALFAM model, *Atmos. Environ.*, 36(20), 3309–3319, doi:10.1016/S1352-2310(02)00300-X.

State of California (2012), Interim population projections for California and its counties 2010–2050, Department of Finance.

Steiner, A. L., S. Tonse, R. C. Cohen, A. H. Goldstein, and R. A. Harley (2006), Influence of future climate and emissions on regional air quality in California, *J. Geophys. Res.*, 111, D18303, doi:10.1029/2005JD006935.

Strada, S., and N. Unger (2016), Potential sensitivity of photosynthesis and isoprene emission to direct radiative effects of atmospheric aerosol pollution, *Atmos. Chem. Phys.*, *16*(7), 4213–4234, doi:10.5194/acp-16-4213-2016.

Strada, S., N. Unger, and X. Yue (2015), Observed aerosol-induced radiative effect on plant productivity in the eastern United States, *Atmos. Environ.*, *122*, 463–476, doi:10.1016/j.atmosenv.2015.09.051.

Sutton, M. A., J. W. Erisman, F. Dentener, and D. Möller (2008), Ammonia in the environment: From ancient times to the present, *Environ. Pollut.*, 156(3), 583–604, doi:10.1016/j.envpol.2008.03.013.

Tai, A. P. K., M. V. Martin, and C. L. Heald (2014), Threat to future global food security from climate change and ozone air pollution, *Nat. Clim. Change*, *4*(9), 817–821, doi:10.1038/nclimate2317.

Tan, Z., and Y. Zhang (2004), A review of effects and control methods of particulate matter in animal indoor environments, *J. Air Waste Manag. Assoc.*, *54*(7), 845–854, doi:10.1080/10473289.2004.10470950.

Travis, K. R. et al. (2016), Why do models overestimate surface ozone in the Southeast United States?, *Atmos. Chem. Phys.*, 16(21), 13561–13577, doi:10.5194/acp-16-13561-2016.

Travis, K. R., D. J. Jacob, C. A. Keller, S. Kuang, J. Lin, M. J. Newchurch, and A. M. Thompson (2017), Resolving ozone vertical gradients in air quality models, *Atmos. Chem. Phys. Discuss*, *2017*, 1–18, doi:10.5194/acp-2017-596.

United Nations, Department of Economic and Social Affairs, Population Division (2017), World population prospects: the 2017 revision.

US Environmental Protection Agency (2015), 2011 National Emissions Inventory data, Version 2. Retrieved from http://www3.epa.gov/ttnchie1/net/2011inventory.html.

Van Damme, M., L. Clarisse, C. L. Heald, D. Hurtmans, Y. Ngadi, C. Clerbaux, A. J. Dolman, J. W. Erisman, and P. F. Coheur (2014a), Global distributions, time series and error characterization of atmospheric ammonia (NH_3) from IASI satellite observations, *Atmos. Chem. Phys.*, 14(6), 2905–2922, doi:10.5194/acp-14-2905-2014.

Van Damme, M., R. J. Wichink Kruit, M. Schaap, L. Clarisse, C. Clerbaux, P.-F. Coheur, E. Dammers, A. J. Dolman, and J. W. Erisman (2014b), Evaluating 4 years of atmospheric ammonia (NH_3) over Europe using IASI satellite observations and LOTOS-EUROS model results, *J. Geophys. Res. Atmos.*, 119(15), 9549–9566, doi:10.1002/2014JD021911.

Van Damme, M. et al. (2015a), Towards validation of ammonia (NH_3) measurements from the IASI satellite, *Atmos. Meas. Tech.*, 8(3), 1575–1591, doi:10.5194/amt-8-1575-2015.

Van Damme, M., J. W. Erisman, L. Clarisse, E. Dammers, S. Whitburn, C. Clerbaux, A. J. Dolman, and P.-F. Coheur (2015b), Worldwide spatiotemporal atmospheric ammonia (NH_3) columns variability revealed by satellite, *Geophys. Res. Lett.*, 42(20), 2015GL065496, doi:10.1002/2015GL065496.

Van Dingenen, R., F. J. Dentener, F. Raes, M. C. Krol, L. Emberson, and J. Cofala (2009), The global impact of ozone on agricultural crop yields under current and future air quality legislation, *Atmos. Environ.*, *43*(3), 604–618, doi:10.1016/j.atmosenv.2008.10.033.

Van Donkelaar, A., et al. (2008), Analysis of aircraft and satellite measurements from the Intercontinental Chemical Transport Experiment (INTEX-B) to quantify long-range transport of East Asian sulfur to Canada, *Atmos. Chem. Phys.*, 8(11), 2999–3014, doi:10.5194/acp-8-2999-2008.

Velthof, G. L., C. van Bruggen, C. M. Groenestein, B. J. de Haan, M. W. Hoogeveen, and J. F. M. Huijsmans (2012), A model for inventory of ammonia emissions from agriculture in the Netherlands, *Atmos. Environ.*, 46, 248–255, doi:10.1016/j.atmosenv.2011.09.075.

Vingarzan, R. (2004), A review of surface ozone background levels and trends, *Atmos. Environ.*, *38*(21), 3431–3442, doi:10.1016/j.atmosenv.2004.03.030.

Von Bobrutzki, K., et al. (2010), Field inter-comparison of eleven atmospheric ammonia measurement techniques, *Atmos. Meas. Tech.*, 3(1), 91–112, doi:10.5194/amt-3-91-2010.

Walker, J. M., S. Philip, R. V. Martin, and J. H. Seinfeld (2012), Simulation of nitrate, sulfate, and ammonium aerosols over the United States, *Atmos. Chem. Phys.*, 12(22), 11,213–11,227, doi:10.5194/acp-12-11213-2012.

Wang, X. et al. (2012), Effects of elevated O_3 concentration on winter wheat and rice yields in the Yangtze River Delta, China, *Environ. Pollut.*, *171*, 118–125, doi:10.1016/j.envpol.2012.07.028.

Wang, Y., D. J. Jacob, and J. A. Logan (1998), Global simulation of tropospheric O_3-NO_x - hydrocarbon chemistry: 3. Origin of tropospheric ozone and effects of nonmethane hydrocarbons, *J. Geophys. Res. Atmos.*, *103*(D9), 10757–10767, doi:10.1029/98JD00156.

Wang, Y. X., M. B. McElroy, D. J. Jacob, and R. M. Yantosca (2004), A nested grid formulation for chemical transport over Asia: Applications to CO, *J. Geophys. Res.*, 109, D22307, doi:10.1029/2004JD005237.

Warner, J. X., Z. Wei, L. L. Strow, R. R. Dickerson, and J. B. Nowak (2016), The global tropospheric ammonia distribution as seen in the 13 year AIRS measurement record, *Atmos. Chem. Phys.*, 16(8), 5467–5479, doi:10.5194/acp-16-5467-2016.

van der Werf, G. R. et al. (2017), Global fire emissions estimates during 1997–2015, *Earth Syst. Sci. Data Discuss.*, 1–43, doi:https://doi.org/10.5194/essd-2016-62.

Wesely, M. L. (1989), Parameterization of surface resistances to gaseous dry deposition in regional-scale numerical models, *Atmos. Environ.*, 23(6), 1293–1304, doi:10.1016/0004-6981(89)90153-4.

Whitburn, S., M. Van Damme, J. W. Kaiser, G. R. van der Werf, S. Turquety, D. Hurtmans, L. Clarisse, C. Clerbaux, and P.-F. Coheur (2015), Ammonia emissions in tropical biomass burning regions: Comparison between satellite-derived emissions and bottom-up fire inventories, *Atmos Environ.*, 121, 42–54, doi:10.1016/j.atmosenv.2015.03.015.

Wiedinmyer, C., and J. C. Neff (2007), Estimates of CO_2 from fires in the United States: Implications for carbon management, *Carbon Balance Manage.*, 2(1), 10, doi:10.1186/1750-0680-2-10.

Wiedinmyer,C., S. K.Akagi, R. J. Yokelson, L. K. Emmons, J.A.Al-Saadi, J. J. Orlando, andA. J. Soja (2011), The Fire INventory fromNCAR (FINN):A high resolution global model to estimate the emissions from open burning, *Geosci. Model Dev.*, 4(3), 625–641, doi:10.5194/gmd-4-625-2011.

Wilczak, J. M., and J. W. Glendening (1988), Observations and Mixed-Layer Modeling of a Terrain-Induced Mesoscale Gyre: The Denver Cyclone, *Mon. Weather Rev.*, 116(12), 2688–2711, doi:10.1175/1520-0493(1988)116<2688:OAMLMO>2.0.CO;2.

Wilkinson, S., G. Mills, R. Illidge, and W. J. Davies (2011), How is ozone pollution reducing our food supply?, *J. Exp. Bot.*, err317, doi:10.1093/jxb/err317.

Wu, S., L. J. Mickley, J. O. Kaplan, and D. J. Jacob (2012), Impacts of changes in land use and land cover on atmospheric chemistry and air quality over the 21st century, *Atmos. Chem. Phys.*, *12*(3), 1597–1609, doi:10.5194/acp-12-1597-2012.

Yevich, R., and J. A. Logan (2003), An assessment of biofuel use and burning of agricultural waste in the developing world, *Glob. Biogeochem. Cycles*, *17*, 40 PP., doi:200310.1029/2002GB001952.

You, L., et al. (2000) Spatial Production Allocation Model (SPAM) 2000 Version 3 Release 1. http://MapSPAM.info. (Accessed Feb, 2012).

Yue, X., and N. Unger (2014), Ozone vegetation damage effects on gross primary productivity in the United States, *Atmos. Chem. Phys.*, *14*(17), 9137–9153, doi:10.5194/acp-14-9137-2014.

Yue, X., N. Unger, K. Harper, X. Xia, H. Liao, T. Zhu, J. Xiao, Z. Feng, and J. Li (2017), Ozone and haze pollution weakens net primary productivity in China, *Atmos. Chem. Phys.*, *17*(9), 6073–6089, doi:10.5194/acp-17-6073-2017.

Zhang, L., L. P. Wright, and W. A. H. Asman (2010), Bi-directional air-surface exchange of atmospheric ammonia: A review of measurements and a development of a big-leaf model for applications in regional-scale air-quality models, *J. Geophys. Res.*, 115(D20), doi:10.1029/2009JD013589.

Zhang, L., D. J. Jacob, E. M. Knipping, N. Kumar, J. W. Munger, C. C. Carouge,A. vanDonkelaar, Y. X.Wang, andD. Chen (2012), Nitrogen deposition to the United States: Distribution, sources, and processes, *Atmos. Chem. Phys.*, 12(10), 4539–4554, doi:10.5194/acp-12-4539-2012.

Zhu, L., D. K. Henze, K. E. Cady-Pereira, M. W. Shephard, M. Luo, R. W. Pinder, J. O. Bash, and G.-R. Jeong (2013), Constraining U.S. ammonia emissions using TES remote sensing observations and the GEOS-Chem adjoint model, *J. Geophys. Res. Atmos.*, 118(8), 3355–3368, doi:10.1002/jgrd.50166.

Zhu, L., D. Henze, J. Bash, G.-R. Jeong, K. Cady-Pereira, M. Shephard, M. Luo, F. Paulot, and S. Capps (2015), Global evaluation of ammonia bidirectional exchange and livestock diurnal variation schemes, *Atmos. Chem. Phys.*, 15(22), 12823–12843, doi:10.5194/acp-15-12823-2015.